Impurities of glacier ice: accumulation, transport and albedo

Urenheter i breis: akkumulasjon, transport og albedo
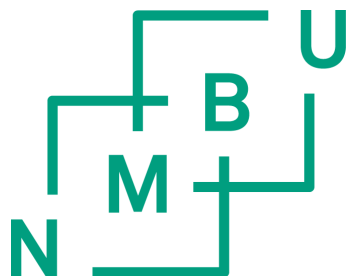
Philosophiae Doctor (PhD) Thesis

Thomas Gölles

Department of Mathematical Sciences and Technology
Faculty of Environmental Science and Technology
Norwegian University of Life Sciences

Department of Arctic Geophysics
The University Centre in Svalbard

Ås and Longyearbyen (2016)

Acknowledgements

A lot has happened in the last 5 years of my life. Right from the start when I first heard of Svalbard I was fascinated. I got a free sample of a newspaper in my post-box which included an article with the title: "Mit den Skiern zur Uni fahren" – skiing to university. After a short semester at UNIS it was clear to me, that I wanted to focus on polar research in my masters. I applied for a master's thesis at AWI in Germany. Originally I applied for an oceanography topic, which turned out to be taken by somebody else. So I was left with a thesis on ice sheets which sounded just as interesting. I am grateful to Klaus Grosfeld and Gerrit Lohmann at AWI for assigning the topic to me which ultimately led to this PhD thesis.

Just at the right timing, the perfect PhD position at UNIS was announced. I couldn't believe I would live on this strange island far north for at least four years. I would like to thank all my colleges and friends at UNIS and in Longyearbyen. "Takk for turen" to everyone who I shared a small or big adventure with.

Thanks to Cecilie, Karin and Mona for translating the summary to Norwegian. I want to thank NCoE SVALI for organising and financing the summer school in Finland. I want to thanks ResClim for their financial support for some of my travels, especially my longer stay in Sapporo, Japan. There I want to thank, one of my supervisors, Ralf Greve for all his support over the years. In Japan I also want to thank Tatsuro Sato and Hakime Seddik for making my time in Japan very enjoyable.

I am grateful to Carl Egede Bøggild for introducing me to this interesting topic and for allowing me as much freedom as I needed. I am also thankful to Cecilie Rolstad Denby for acting as my "mainland" supervisor and for the administrative work at NMBU.

Acknowledgements

I became a father of two wonderful sons in the last 3 years: Björn and Oskar. I am very happy that you came into my life. I am especially grateful to Karin, Inga-Lill and my parents for babysitting, which gave me more time to work on the thesis. I also have to express my gratitude to the Norwegian system which allowed my to take some months off and to work part-time for some additional months allowing me more time with my family. Its sad that being fully paid and having all social benefits as a PhD candidate is an exception.

I also want to thank my friends in Austria for keeping me in touch despite the distance. Further, I want to express my gratitude to my parents and brother for their constant interest and support. Finally, I want to thank Karin – I am looking forward to our next adventures!

Månsta, May 2016

Contents

List of Tables

List of Articles

Article I: *Goelles, T. and Bøggild, C. E.*: Albedo reduction of ice caused by dust and black carbon accumulation from melt-out and atmospheric deposition, under review for the Journal of Glaciology, 2016

Article II: *Goelles, T., Bøggild, C. E. and Greve, R.*: Ice sheet mass loss caused by dust and black carbon accumulation, The Cryosphere, 9(5), 1845–1856, doi:10.5194/tc–9–1845–2015, 2015.

Article III: *Goelles, T., Grosfeld, K. and Lohmann, G.*: Semi-Lagrangian transport of oxygen isotopes in polythermal ice sheets: implementation and first results, Geoscientific Model Development, 7(4), 1395–1408, doi:10.5194/gmd–7–1395–2014, 2014.

Summary

The Greenland ice sheet is the largest ice mass in the Northern Hemisphere and has experienced accelerating mass loss in recent decades. An increase in surface melt is the major cause for the loss of mass. Albedo is a major control of surface melt and has decreased over the entire Greenland ice sheet, especially at lower elevations near the margin where glacier ice is exposed for part of each year. The albedos of ice and snow are lowered by dark impurities such as mineral dust and black carbon, a by-product of combustion. These impurities are a heterogeneous group of highly absorbent particles which reach the ice sheet via atmospheric transport from distant and local sources. Parts of these impurities are buried in the accumulation zone and become part of the moving ice. After a significant transport time, up to tens of thousands of years, these englacial impurities re-emerge in the ablation zone near the margin. These re-emerging impurities, together with those directly deposited, accumulate on the ice surface. Once located on the ice surface, these impurities darken the ice surface for several years and lower the albedo, causing more melt.

Current sea-level projections rarely include albedo as a dynamic model component. In models which consider albedo, snow albedo is often treated with sophisticated methods, while ice albedo is still treated as a constant. Albedo lowering is a major cause of the current mass loss of the Greenland ice sheet, and the role of ice albedo will increase under a warmer climate. Therefore, this study presents a model with a dynamic component of ice albedo.

The model framework includes the effect of impurities on the mass balance and ice sheet geometry. The framework consists of an ice dynamics component which is linked to a module of englacial impurity transport. This component feeds into the impurity accumulation module, which deals with both snow and ice. An albedo

module which accounts for mineral dust and black carbon accumulation uses this output to derive daily albedo values. A simplified surface energy balance model is used to derive the surface melt rate and surface mass balance, which is then fed back into the ice dynamics component.

This model framework is used to investigate the role of melt-out and impurity accumulation on the melt of the Greenland ice sheet. For that purpose, simplified geometry and different temperature pathways are used to simulate the evolution of the ice sheet over 1000 years. Due to the feedback between melt-out, ice albedo and impurity accumulation, the role of impurities is disproportionally larger in warmer scenarios. In the warmest scenario (RCP8.5), a conservative estimate for the additional mass loss due to impurity accumulation in the year 3000 was 7%.

Melt-out of dust is the largest source of impurities on the ice surface. Darkening is not always dominated by dust, however, due to the high absorption of black carbon. The amount of impurities from melt-out depends on the englacial impurity concentration and surface melt. The englacial impurity concentration, in turn, relies on the computed age of the ice and a time series of impurity concentration. Therefore, the accuracy of the transport scheme, which provides the age of the ice, is crucial for overall accuracy.

A semi-Lagrangian transport scheme of second-order accuracy was implemented in the 3D ice sheet model SICOPOLIS (SImulation COde for POLythermal Ice Sheets). The model was applied to the ice sheets of Greenland and Antarctica. Artificial ice cores of δ^{18}O, a proxy for surface temperature, were compared to ice core data. The results of the second-order scheme were identical to the results of the first-order scheme in the ice sheet interior. The results deviated substantially, however, in the outer regions near the margin.

The results emphasise that the role of ice albedo and impurities for the surface mass balance will be even greater under warmer conditions. Furthermore, the presented model framework is not limited to Greenland but can also be adapted for valley glaciers and paleo-ice sheets.

Sammendrag

Iskappen på Grønland er den største ismassen på den nordlige halvkule og masse-tapet her har vært akselererende de siste tiårene. En økning i overflatesmeltingen er den viktigste årsaken til tap av masse. Albedoen, som er hovedfaktoren for overflatesmeltingen, har avtatt over hele iskappen på Grønland, og særlig i lavere høyde nær iskanten hvor breisen er eksponert for et visst tidsrom årlig. Albedoen for is og snø er redusert pga mørkere partikler og urenheter, som mineralstøv og black carbon (sot), et bi-produkt av forbrenning. Disse urenhetene er en het-erogen gruppe av svært absorberende partikler som transporteres til iskappen via atmosfæren fra lokale og fjerntliggende kilder. Deler av disse urenhetene opptas i akkumulasjonssonen og blir del av den bevegelige isen. Etter lang tids transport, opptil titusener av år, vil disse englasiale urenhetene komme frem i ablasjonssonen nær brekanten. Både englasialt transporterte urenhetene og dirkete avsatte urenheter akkumuleres på isoverflaten. Når urenhetene først er avsatt på isoverflaten vil de bidra til en mørkere isoverflate med redusert albedo, og derved bidra til økt smelting.

Nåværende havnivå prognoser inkluderer sjelden albedo som en dynamisk modellkomponent. I modeller som inkluderer albedo blir snøalbedoen ofte justert med sofistikerte metoder, mens isalbedoen blir holdt konstant. Albedo er hoved-driveren av det pågående massetapet for Grønlandsisen, og isalbedoens rolle vil forsterkes under et varmere klima. Av denne grunn presenteres det i dette studie en modell med en dynamisk komponent for isalbedo.

Dette modellrammeverket blir brukt til å undersøke hvilken rolle utsmelting og akkumulasjon av urenheter spiller på avsmeltingen av iskappen på Grønland. En forenklet geometri og forskjellige temperaturtraseer blir brukt til å simulere utviklingen av iskappen over 1000 år. På grunn av tilbakekoblingsmekanismene

mellom utsmelting, isalbedo, og akkumulasjon av urenheter er rollen av urenheter uproporsjonalt større i varmere scenarier. I det varmeste scenariet (RCP8.5) er et konservativt estimat for massetap på grunn av akkumulasjon av urenheter i året 3000 på 7 %.

Utsmelting av støv er den største kilden til urenheter på isoverflaten. Sverting av overflaten er allikevel ikke alltid dominert av støv, pga. den høye absorbsjonen av black carbon. Mengden av urenheter pga. utsmelting avhenger av den englasiale urenhetskonsentrasjonen og overflatesmelting. Den englasiale konsentrasjonen avhenger igjen av den beregnede alderen av isen og av en tidsserie av urenhet-skonsentrasjoner. Derfor er nøyaktigheten av transportskjema, som gir alderen på isen, essensiell for den generelle nøyaktigheten.

Et semi-Lagrangian transport skjema av annen ordens nøyaktighet ble imple-mentert i den tre dimensjaonale iskappemodellen SICOPOLIS (SImulation COde for POLythermal Ice Sheets). Modellen ble anvendt for iskappene på Grønland og Antarktis. Genererte iskjerne data av δ^{18}O, en proxy for overflate temperatur, ble sammenlignet med iskjerne data. Resultatet av annen ordens skjemaet var iden-tisk til resultatet til første ordens skjemaet i det indre av iskappen, men resultatene avvek vesentlig i de ytre regionene nær iskanten.

Resultatene understreker rollen isalbedo og urenheter har for overfalte masse-balansen, en rolle som også vil bli enda større ved varmere forhold. Videre er det presenterte modellrammeverket ikke begrenset til Grønland men det kan også tilpasses dalbreer og paleo-iskapper.

Abbrevations

AR5	Fifth Assessment Report
AWS	automatic weather station
BC	black carbon
BrC	brown carbon
CTS	cold–temperate surface
EBC	equivalent black carbon
EBM	energy balance model
EC	elemental carbon
ELA	equilibrium line altitude
ESM	Earth system model
GrIS	Greenland ice sheet
K-transect	Kangerlussuaq transect in western Greenland
KPCL	Kronprinz Christians Land in northeastern Greenland
LGM	last glacial maximum
OC	organic carbon
OM	organic matter
rBC	refractory black carbon
SD	standard deviation
SIA	shallow ice approximation
SLT	semi-Lagrangian transport

SMB	surface mass balance
SSA	specific surface area
TIM	temperature index model
TOA	top of atmosphere
PDD	positive degree day
ppb	parts per billion
ppm	parts per million

Chapter 1

Introduction

1.1 Overview

This thesis consists of this introduction, three research articles and a concluding chapter (5). The introduction starts with the Greenland ice sheet. Next, the basics of surface mass balance and energy balance are introduced which leads to the introduction of albedo. A section on impurities follows that introduces cryoconite, impurity accumulation and different impurities species and their effects on albedo. The introduction is concluded by providing the motivation for the three research articles, which are as follows:

Article I: *Goelles, T. and Bøggild, C. E.*: Albedo reduction of ice caused by dust and black carbon accumulation from melt-out and atmospheric deposition, under review for Journal of Glaciology, 2016

Article II: *Goelles, T., Bøggild, C. E. and Greve, R.*: Ice sheet mass loss caused by dust and black carbon accumulation, The Cryosphere, 9(5), 1845–1856, doi:10.5194/tc–9–1845–2015, 2015.

Article III: *Goelles, T., Grosfeld, K. and Lohmann, G.*: Semi-Lagrangian transport of oxygen isotopes in polythermal ice sheets: implementation and first results, Geoscientific Model Development, 7(4), 1395–1408, doi:10.5194/gmd–7–1395–2014, 2014.

The articles are in logical, rather than chronological, order. Articles II and III have been published, and Article I is currently under review for the Journal of Glaciology.

The articles have been reformatted to fit the format of the thesis but are otherwise identical to the published versions. A common list of references for the introduction and all articles is included at the end of the thesis.

1.2 The Greenland ice sheet

The Greenland ice sheet (GrIS) is currently the second-largest ice sheet in the world and the largest ice body in the Northern Hemisphere. It is approximately 2.93 million km^3, which is equivalent to 10% of the Earth's fresh water. A complete melt of the GrIS would cause an average global sea level rise of 7.36 metres (Bamber et al., 2013). The GrIS extends roughly 2200 km from south to north and about 1100 km from east to west. The ice sheet covers roughly 80% of Greenland's land surface and is about 1.7 million km^2. Its maximum thickness is 3367 metres, and average thickness is about 1600 metres (Thomas and PARCA Investigators, 2001).

Ice sheets and glaciers gain mass through snowfall and deposition and lose mass through surface melt, sublimation, basal melt due to geothermal heating, basal melt of ice shelves and calving of icebergs. Sublimation, snowdrift and subglacial melting all play a minor role for the GrIS (Box et al., 2006).

The GrIS is currently losing mass (Shepherd et al., 2012), and the rate of mass loss has increased since 1992 (Vaughan et al., 2013). The acceleration is mainly caused by an increase in surface melt. From 2000 to 2008, about half of the mass loss of the GrIS was attributed to calving and the other half to surface melt (Van den Broeke et al., 2009). The proportion of mass loss after 2009 is about two-thirds caused by surface melt and one-third by calving of icebergs (Enderlin et al., 2014). The amount of calving of the GrIS has been constant for the last 110 years (Kjeldsen et al., 2015). Therefore, the increase in mass loss of the GrIS is mainly due to a decrease in the surface mass balance (SMB).

Surface melt is largely controlled by near-surface temperature and absorbed short-wave radiation. The amount of incident radiation and the surface albedo control the proportion of absorbed short-wave radiation (Bougamont et al., 2005; Van de Wal et al., 2005; Tedesco et al., 2011; Van As, 2011; van Angelen et al., 2012; Van As et al., 2012). Therefore, the broadband albedo has been identified as a major component of the SMB of the GrIS (Bougamont et al., 2005; Tedesco et al., 2011; van Angelen et al., 2012).

Remote and in-situ measurements of the surface albedo of the GrIS have revealed a decline over the whole ice sheet (Tedesco et al., 2011; Box et al.,

2012; Stroeve et al., 2013; Tedesco et al., 2016). During the June-August period of 2000 to 2010, the average decline in the ablation zone was -0.056 ± 0.007 and -0.091 ± 0.021 in the ablation zone (Box et al., 2012). Remote sensing data from 1996 to 2012 showed an albedo decline of 0.02 per decade (Tedesco et al., 2016). The albedo decrease is pronounced in the ablation zone (Box et al., 2012; Tedesco et al., 2016), where the drop of albedo is caused by an increasingly earlier exposure of darker ice after the winter snow cover has melted away. Under a warmer climate, snow melts earlier and the equilibrium line moves to higher elevations (Brutel-Vuilmet et al., 2013; Vizcaino et al., 2014), which causes ice to be exposed for a longer time and over a wider area. Model simulation suggests that the variability of the SMB will increase in the future and be tied to incoming solar radiation and the surface albedo (Fyke et al., 2014).
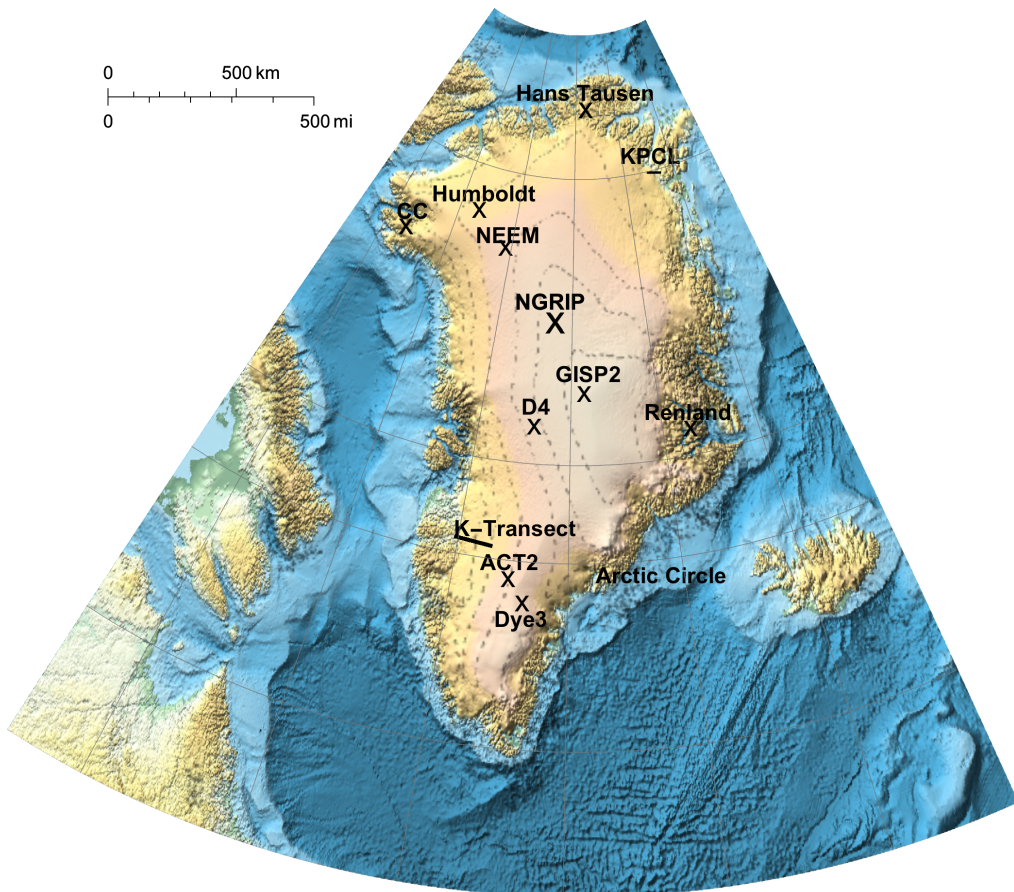

Figure 1.1: Map of Greenland and the locations referred to in the thesis.

1.3 Surface mass balance

SMB drives the internal flow of glaciers and ice sheets. Ice starts to flow as a response to a change in the surface slope that is introduced by mass loss at lower elevations and mass gain at higher elevations. The SMB is often simply called "mass balance," but it should not be confused with the total mass balance. In addition to the SMB, the total mass balance also includes mass exchanges at the bed and margin, such as calving and subglacial melt.

SMB is expressed either in units of volume or mass. In addition, SMB-related terms can either be denoted as a cumulative sum or changes over a stated span of time, usually a season or year. These rates of change are denoted by an overdot, which represents a partial derivative with respect to time.

The SMB is calculated either for an individual point with the symbol $\dot{b}_{\text{sfc}}$ or averaged over the entire surface area which is expressed by the symbol $\dot{B}_{\text{sfc}}$. SMB at a point on a glacier is the deviation between surface accumulation ($\dot{c}_{\text{sfc}}$) and surface ablation ($\dot{a}_{\text{sfc}}$).

Surface accumulation refers to all processes which add snow or ice to a glacier or ice sheet. Surface ablation includes all processes of removal (Cuffey and Paterson, 2010). Therefore, $\dot{c}_{\text{sfc}}$ is a positive contribution and $\dot{a}_{\text{sfc}}$ a negative one to $\dot{b}_{\text{sfc}}$:

$$\dot{b}_{\text{sfc}} = \dot{c}_{\text{sfc}} - \dot{a}_{\text{sfc}} \tag{1.1}$$

Integration of $\dot{b}_{\text{sfc}}$ over the whole surface area S yields the average SMB in m water equivalent (w.e.) per year:

$$\dot{B}_{\text{sfc}} = \frac{1}{S} \int_{S} \dot{b}_{\text{sfc}} \, \mathrm{d}S \tag{1.2}$$

Several processes determine the SMB at a point on a glacier or ice sheet. Depending on the location, the same process contributes to accumulation or ablation. For example, wind drift can either cause snow to accumulate or dissipate. The most important processes are snowfall and surface melt; for polar ice mass, refreezing is also important. Therefore, Equation 1.1 becomes the following:

$$\dot{b}_{\text{sfc}} = \dot{c}_{\text{sfc(sn)}} + \dot{c}_{\text{sfc(rainfall)}} - \dot{a}_{\text{sfc(evaporation/sublimation)}} - \dot{a}_{\text{sfc(runoff)}} \tag{1.3}$$

$\dot{c}_{\text{sfc(rainfall)}}$ is the accumulation by rainfall, $\dot{a}_{\text{sfc(evaporation/sublimation)}}$ is the ablation by evaporation or sublimation and $\dot{a}_{\text{sfc(runoff)}}$ is the ablation by runoff.

Liquid water from rain or surface melt refreezes inside the snowpack if the temperature is below the freezing point. Liquid water may also refreeze at the base of snow overlying glacier ice, forming "superimposed ice". If refreezing occurs below the summer surface, it represents internal accumulation which is sometimes, incorrectly, directly included in the SMB (Cogley et al., 2011). The summer surface is identified as the surface on which the first snow of the new balance year falls. Liquid water which does not refreeze leaves the ice sheet and is called runoff:

$$\dot{a}_{\text{sfc(runoff)}} = \dot{M}_{\text{s}} + \dot{\text{rainfall}} - \dot{\text{refreezing}} \tag{1.4}$$

where M_{s} is the surface melt rate.

Most glaciers and ice sheets can be divided into two zones determined by the annual SMB: the accumulation zone, where the annual SMB is positive, and the ablation zone, where it is negative. Those two zones are divided by the equilibrium line, where the annual SMB is zero. The equilibrium line of the GrIS is located at altitudes between 1000 and 1500 metres (lower in northernmost Greenland, Cuffey and Paterson (2010)).

1.4 Surface energy balance

The surface energy balance governs the net energy flux (E_{N}) into the surface and describes the processes which drive surface melt. The units of energy flux density are W m^{-2} and the flux is positive if it is in the direction towards the snow or ice surface. A positive net energy flux E_{N} drives melt, and a negative one drives refreezing if liquid water is available. At 0°C surface temperature, any surplus energy is assumed to be used for melting snow or ice. The net energy flux combines the following components (Cuffey and Paterson, 2010):

$$E_{\text{N}} = \underbrace{E_{\text{S}}^{\downarrow} + E_{\text{S}}^{\uparrow} + E_{\text{L}}^{\downarrow} + E_{\text{L}}^{\uparrow}}_{\text{radiation fluxes}} + \underbrace{E_{\text{H}} + E_{\text{E}}}_{\text{turbulent fluxes}} + E_{\text{G}} + E_{\text{P}} \tag{1.5}$$

where $E_{\text{S}}^{\downarrow}$ is the downward shortwave radiation, $E_{\text{S}}^{\uparrow}$ is the upward shortwave radiation and $E_{\text{L}}^{\downarrow}$ and $E_{\text{L}}^{\uparrow}$ are the downward and upward longwave radiations. These radiative fluxes combined yield the net radiation (E_{R}). The sensible heat flux (E_{E}) and latent heat flux (E_{H}) are the turbulent fluxes. E_{G} is the ground energy flux, and E_{P} is the heat flux from precipitation.

Surface melt rate M_s from the available energy is represented by the following:

$$M_s = \frac{E_N}{\rho_w L_f} \tag{1.6}$$

where ρ_w is the density of water, and L_f is the latent heat of fusion for ice.

The magnitude of each process in Equation 1.5 depends on the atmospheric conditions and surface properties. For a detailed discussion, see Cuffey and Paterson (2010), Oerlemans (2001) and Hock (2005). Examples of these studies of the surface energy balances of the GrIS can be found for example in Van As et al. (2012), which focuses on the ablation zone or Cullen et al. (2014), which focuses on the accumulation zone.

The energy available for melt in June, July and August decreases with elevation. In the lower ablation zone of the GrIS, the available energy averages $150\,\text{W m}^{-2}$ and is usually 0 at higher elevations in the dry snow zone (Van As et al., 2012). An exception was in 2012 when almost the entire GrIS (98.6%) experienced melt (Nghiem et al., 2012).

In the ablation zone of the GrIS, most of the available energy for melt stems from net shortwave radiation ($E_S^{\downarrow} + E_S^{\uparrow}$) which is in the order of $100\text{–}150\,\text{W m}^{-2}$ (Van As et al., 2012). The net longwave radiation was found to be negative at all elevations but never exceeded $-60\,\text{W m}^{-2}$ at higher elevations. The sensible heat flux is greatest at lower elevations around $40\,\text{W m}^{-2}$ and near zero in the accumulation zone. Latent heat, ground heat flux and rain are low at all elevations. Also, in alpine valley glaciers most of the energy used for melt is supplied by radiation, followed by the sensible heat flux and only a minor fraction from latent heat (Hock, 2005).

A complete surface energy balance is the most physical way to derive melt rates. The advantage is that each source of energy can by quantified and changes in each component can be monitored. This advantage comes at the cost of required inputs, which are not always available, especially the turbulent fluxes requiring near-surface gradients of wind speed, temperature and specific humidity. For model studies of glaciers or ice sheets, these quantities need to be provided by an atmospheric model, which is not always feasible or desired. Therefore, several other methods for melt have been developed.

The temperature index model (TIM) or positive degree-day models (PDD) link air temperature with snow or ice melt. Air temperature is usually available in models and is easy to measure. Both models link air temperature to melt via an empirical melt factor. These melt factors vary from site to site and over time. Despite their simplicity, they often match the performance of full-energy balance

models on the catchment scale (e.g. Rango and Martinec, 1995). These models perform well because many components of the surface energy balance are linked to air temperature (Hock, 2005).

The disadvantage of these simple models is that the melt factors are site dependent and might not be the same under different climatic conditions. Some temperature index models, therefore, use an extended formulation which includes different components of the surface energy balance, like net radiation, vapour pressure or wind speed.

The biggest source of radiation is net shortwave radiation, which is the difference between incoming and outgoing shortwave radiation. The incoming shortwave radiation (also called insolation or global radiation) is the sum of the direct solar beam, the diffuse radiation from all directions due to scattering in the atmosphere, and the reflection from the surrounding terrain. All the effects of direct, diffuse and reflected components can be expressed by the following equation of the downward shortwave radiation (Cuffey and Paterson, 2010):

$$E_S^{\downarrow} = S_{\text{TOA}} \cdot \cos\theta_z \cdot \tau_a \tag{1.7}$$

where S_{TOA} is the top of the atmosphere solar flux, θ_z is the zenith angle of the sun and τ_a is the effective transmissivity, which expresses how much of the total solar radiation strikes the surface. The effective transmissivity depends on cloud cover, altitude and haze.

The outgoing shortwave radiation is the reflected part of the downward radiation and can be described by the following equation:

$$E_S^{\uparrow} = \alpha_s E_S^{\downarrow} \tag{1.8}$$

where α_s is the broadband surface albedo (discussed in detail in the following section).

1.5 Albedo of snow and ice

The albedo or broadband albedo as defined in Grenfell (2011) is: "The fraction of incident solar radiative energy flux, or irradiance, reflected and scattered upward from a surface integrated over the solar spectrum from 300 to approximately 3000 nm". Different studies have used different limits; (Hock, 2005) for example, used 350–2800 nm. The limits are based on the range of the solar spectrum (see

Figure 1.3a); the actual limits have only a minor effect since the solar radiation is low near the limits.

Examples of broadband albedos are given in Table 1.1. An albedo of 0.70 means that 70% of the incident solar radiation is reflected. Snow has a high albedo, and fresh dry snow has the highest naturally occurring albedo.

Table 1.1: Examples of snow and ice albedo from (Cuffey and Paterson, 2010) and †
(Bøggild et al., 2010), ∗ (Knap and Oerlemans, 1996), ▷ (Bøggild et al., 1996),
§(Van den Broeke et al., 2008).

Surface type	min	max
fresh dry snow	0.75	0.98
old clean dry snow	0.70	0.85
old clean wet snow	0.46	0.70
old dirty dry snow	0.30	0.60
old dirty wet snow	0.30	0.50
clean glacier ice ▷ §	0.30	0.56
dirty ice †	0.21	0.44
cryoconite basin †	0.10	0.11
superimposed ice † ∗	0.63	0.68
tundra †	0.14	0.23

The spectral albedo is defined as the ratio between upwelling and incident irradiance versus the wavelength of radiation:

$$\alpha_\lambda = \frac{E_S^\uparrow(\lambda)}{E_S^\downarrow(\lambda)} \tag{1.9}$$

The total or broadband albedo, often just called albedo, is related to the spectral albedo by the following equation:

$$\alpha_s = \frac{E_S^\uparrow}{E_S^\downarrow} = \frac{\int_{SW} \alpha_\lambda E_S^\downarrow(\lambda)\,\mathrm{d}\lambda}{\int_{SW} E_S^\downarrow(\lambda)\,\mathrm{d}\lambda} = \frac{\int_{SW} \alpha_\lambda E_S^\downarrow(\lambda)\,\mathrm{d}\lambda}{E_S^\downarrow} \tag{1.10}$$

where $\int_{SW}$ denotes an integration over the shortwave band (Cuffey and Paterson, 2010). The downward radiation consists of the direct and diffuse radiation over the whole spectrum. The upward shortwave radiation ($E_S^\uparrow$) is a result of scattering and reflection by the near-surface layers.

Wiscombe and Warren (1980) developed the first physically based model of snow albedo over the solar spectrum which also accounted for direct and diffuse radiation. They computed scattering and absorption for a single snow grain with the Mie theory by approximating the grain with an optically equivalent sphere. Multiple scattering was approximated with the delta-Eddington approximation, which is a radiative transfer model suited for strongly forward-scattering optical media such as ice. One important insight from the Mie theory is that the bigger the sphere, the more is scattered in the forward direction (the direction of the incident light). The model of Wiscombe and Warren (1980) matched observations accurately in the near-infrared spectrum but over-predicted the observed albedo in the visible range. The companion study of Warren and Wiscombe (1980) also accounts for impurities, which solved the visual range problem. Even very small concentrations of highly absorbent impurities lower the albedo substantially.

A conceptual illustration of scattering and absorption in a layer of snow or ice is given in Figure 1.2. The incident radiation gets scattered by snow grains (Figure 1.2 (a)). A snowflake quickly loses its delicate shape and can be described as a sphere. The bigger the snow grain, the more is scattered in the forward direction. In addition, a bigger snow grain leads to more absorbed radiation because the radiation needs to travel through more ice in bigger grains (Grenfell, 2011).

In ice, the radiation gets scattered by air bubbles, which can also be described as spheres. Therefore, for both snow and ice, the Mie theory can be applied in a similar fashion; only the material properties differ (Mullen and Warren, 1988). In ice, the radiation needs to travel through more absorbent material. This leads to higher absorption in ice than snow, even though ice is not very absorbent. This explains why the albedo of ice is lower than snow. In addition, the scattering and absorption of impurity particles (c) also needs to be addressed.

The specific surface area (SSA) is an important physical property of ice related to air bubbles. The SSA is the ratio of air-ice interface area to ice mass (e.g. Dadic et al., 2013). The albedo is directly related to SSA: a high SSA results in a high albedo. The "weathering crust" (also called the ablation crust, radiation crust or melt crust), a shallow, porous layer of ice produced by differential melt, is also related to SSA (Müller and Keeler, 1969; Irvine-Fynn et al., 2011b). The weathering crust on the GrIS is a few centimetres thick (Chandler et al., 2015;
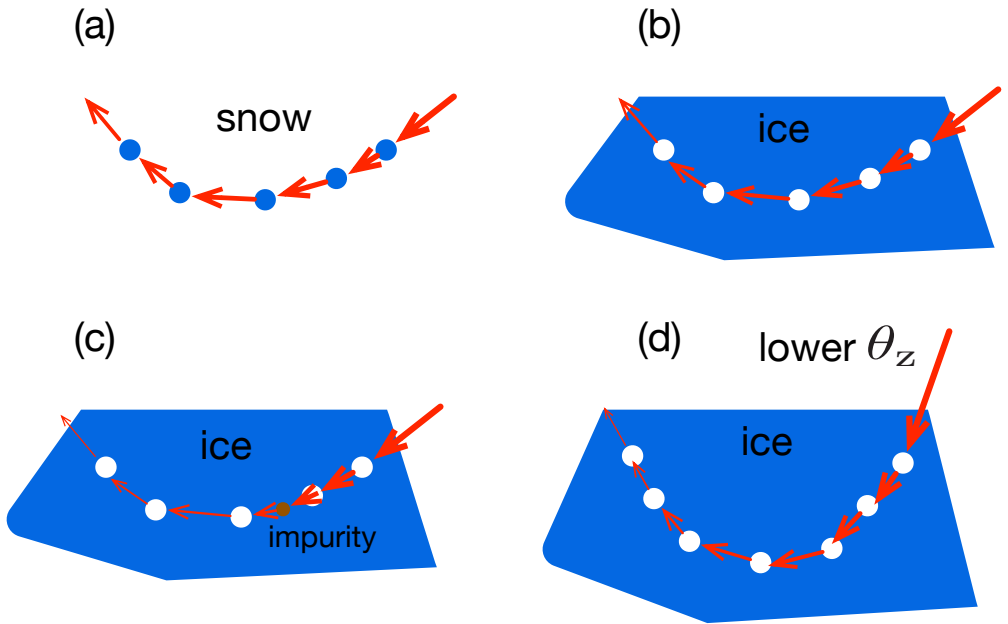
Figure 1.2: Schematic diagram showing the influence of grain size, air bubble and zenith angle of the sun on albedo (inspired by Grenfell (2011)). The width of the arrow indicates the relative intensity. **(a)** Snow with small grains, low absorption, high albedo; **(b)** Ice with small air bubbles, higher absorption, lower albedo compared to snow; **(c)** Ice with an impurity particle, higher absorption, lower albedo than in **(b)**; **(c)** Lower zenith angle of the sun, greater absorption path length, lower albedo than in case **(b)**

Konzelmann and Braithwaite, 1995). The weathering crust has a higher SSA compared to the undisturbed glacier ice; therefore, the ice surface albedo is higher when a weathering crust is present.

Figure 1.2(d) shows the case when the sun is high above the horizon, i.e. the zenith angle is low. The radiation can penetrate deeper into the ice or snow layer because of the forward scattering. This deeper penetration gives the radiation more opportunities to scatter and be absorbed, causing a lower albedo. The longer travel path increases the probability that the radiation will interact with an impurity. Therefore, the effect of impurities is higher at lower zenith angles.

Albedo is not an intrinsic material property. As shown in Figure 1.2, albedo also depends on the zenith angle of the sun and the fraction of diffuse radiation. Pure diffuse radiation causes the same albedo as direct radiation at the solar zenith angle of 50° (Wiscombe and Warren, 1980). In addition, clouds cause a shift in the solar spectrum, resulting in a higher albedo (Greuell and Konzelmann, 1994).

Figure 1.2 is simplified as it shows only the main direction of radiation and ignores scattering at the crystal boundaries and ice/air interface. Nevertheless, the figure effectively illustrates the influence of the zenith angle and impurities.

Figure 1.3(a) shows the amount of solar radiation at the top of the atmosphere (TOA) in red and at sea level in orange. As the radiation passes through the atmosphere, some parts are modified by scattering, absorption and reflection, which causes the dents in the spectrum at sea level. The example is taken from North America and represents clear sky conditions. For Greenland, the radiation is much lower due to the higher zenith angles and is further reduced by clouds. Nevertheless, the spectrogram has a similar shape but lower magnitudes (Grenfell, 2011). The spectrogram peaks in the visible range (380–750), where solar irradiance is highest.

The complex index of refraction m of ice is strongly dependent on the wavelength λ:

$$m_\lambda = n_\lambda + ik_\lambda \tag{1.11}$$

where k is the extinction coefficient.

Panel (b) shows the real part of the index of refraction for ice, black carbon (BC) and dust of two different origins. Panel (c) shows the imaginary part of the index of refraction of BC, saharan dust and ice on a logarithmic scale. The absorption of ice is weak below 170 nm and extremely weak in the visible range. At the same range where the incoming radiation is highest (Figure 1.3(a)). Both, BC and dust are highly absorbent in the visible range. Therefore, even low concentrations of
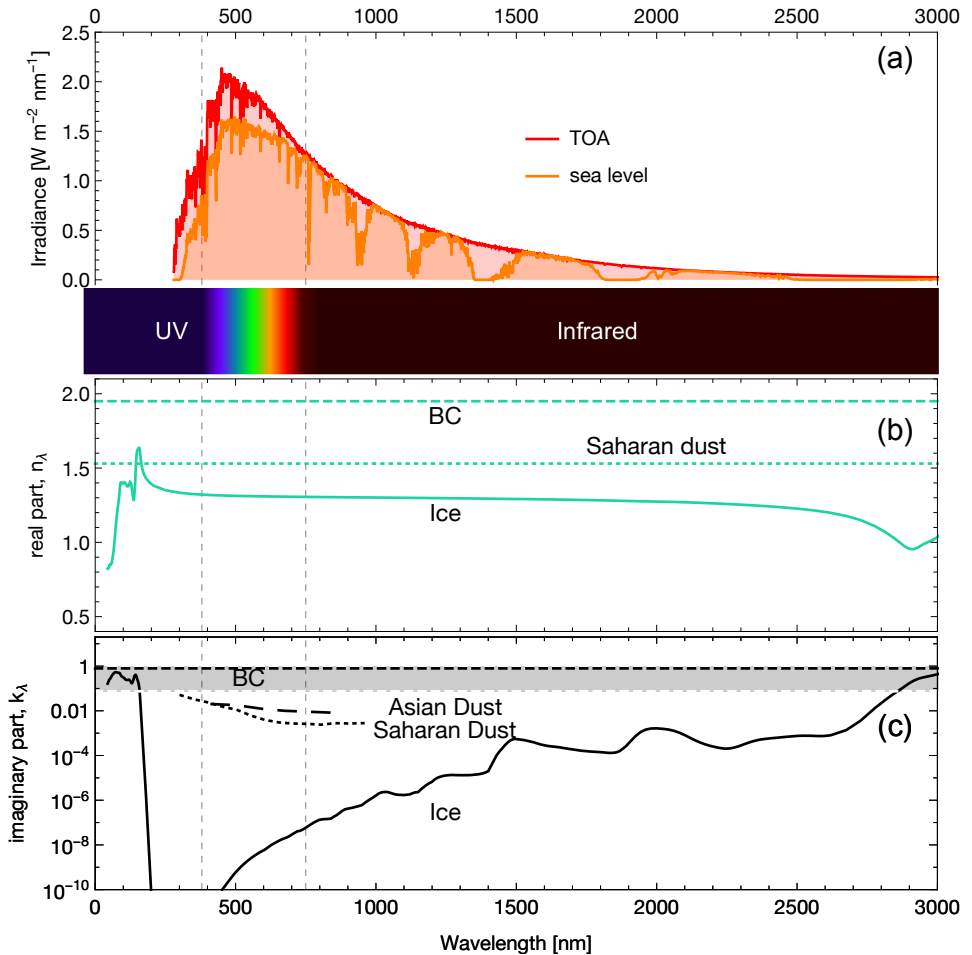
Figure 1.3: (a) spectral irradiance at the top of atmosphere (TOA) and sea level (ASTM International, 2012). **(b)** real part and **(c)** imaginary part of the complex refraction index. The extinction coefficient (k_λ) of ice is strongly dependent on wavelength, and is very low in the visible spectrum (Warren and Brandt, 2008). The extinction coefficient of black carbon (BC) does not depend on wavelength, and the recommended value is 0.79 (Bond and Bergstrom, 2006). The exact value of BC depends on the source and range of the values is indicated in grey. Dust has a lower k than BC, shown here in examples from the Sahara (Burkina Faso, Wagner et al. (2012)) and Asia (Zhangye: 39.082°N, 100.276°E, Ge et al. (2010)).

dust or BC have a big influence on albedo. Between 1000 and 3000 nm ice is moderately absorbent and impurities play a lesser role. Therefore, the biggest change in spectral albedo due to impurities is in the visible range (Warren and Wiscombe, 1980).

Due to ice's low absorption, scattering is the dominant process for snow extinction (sum of scattering and absorption); scattering is responsible for 99.99% of extinction in the visible range. The low absorption even plays a role in ice without bubbles of impurities because radiation can travel for long distances within the ice.

The absorption length of pure ice ranges from 700–6000 m (Warren et al., 2006) at 390 nm. In contrast, measurements from apparently clean, deep Antarctic ice had an absorption length of 240 m, and ice grown in laboratories had an absorption length of 10 m. The large spread is caused by different measurement techniques as well as microscopic bubbles and impurities.

1.6 Impurities

1.6.1 Cryoconite

Cryoconite is a granular sediment found on glacier ice surfaces and consists of biological material, mineral material, black carbon and other particles. The term cryoconite was first used by the Arctic explorer Nils Adolf Erik Nordenskiöld after his travels to Greenland in 1870 (Nordenskiöld, 1875). The word is a combination of the Greek words "kryos", meaning cold, and "konis", meaning dust. The effect of impurities on albedo and melt was documented as far back as 1875 by Nordenskiöld (1875) and in 1906 by another famous polar explorer Nansen (1906) (as cited in Cook et al. (2015)).

Impurities which have been transported by wind are often referred to as aerosols, even after they have been deposited on ice or snow. Therefore, aerosols in the glaciological context should be understood to be "past aerosols".

Cryoconite can be located inside cryoconite holes, in streams, dispersed as granules over the ice surface (Hodson et al., 2007, e.g.) or inside wide cryoconite holes called cryoconite basins (Bøggild et al., 2010). A cryoconite hole is a water-filled depression which forms on the surface as dark cryoconite melts into ice. These holes are deeper in polar glaciers (20–50 cm) compared to middle- and low-latitude glaciers (3–20 cm) (Takeuchi, 2011). The lifespan of a cryoconite hole is shorter on glaciers with high melt rates, while in polar regions a lifespan of 100–200 years may be possible (Takeuchi, 2011).

1.6.2 Impurity accumulation on the ice surface

Figure 1.4 shows a sketch of the processes of impurity accumulation at a location in the ablation zone of an ice sheet or glacier. In this example, the winter snow cover starts to form on the first of October. The albedo increases as a layer of snow forms (c). Snow grain size increases after the time of deposition, causing the albedo to decrease.

Impurities are deposited by dry or wet deposition with snowflakes. The albedo of snow is quickly lowered as the impurity is swiftly covered by fresh snow. Snow starts to melt around the first of May as it gets warmer, causing the snow grains to grow rapidly, which lowers the albedo. The layers with impurities re-emerge as snow melts, causing the impurities to accumulate on the surface (Doherty et al., 2013). These impurities stay close to the snow surface and further lower the albedo. This process of melt-out and accumulation on the snow surface is likely the reason for the darkening of the GrIS in the accumulation zone (Tedesco et al., 2016), as the source of the impurities has not increased significantly.

The released meltwater refreezes at the base of the snowpack, forming superimposed ice. The superimposed ice layer melts away as the temperatures increase further, and ice is exposed. A layer with a higher impurity concentration melts out and releases the impurities onto the ice surface. A fraction of these impurities, as well as those released by the snowpack, are moved by meltwater into cryoconite holes. These impurities in the cryoconite holes are shielded from the low-standing sun and therefore do not influence the albedo directly (Bøggild et al., 2010). If the cryoconite hole melts out, all its enclosed impurities are released onto the ice surface, causing a decrease in the albedo.

A summer snowfall event causes a short increase in the albedo until the snow has melted away. Clouds cause an increase in the albedo by shifting the solar spectrum. In autumn, the cycle starts again, and impurities located on the ice surface and inside cryoconite holes are conserved under the seasonal snow cover. Cryoconite holes can last for several years or possibly decades (Takeuchi, 2011).

Meltwater also has an indirect influence on the albedo. The optical properties of pure ice and water are very similar in the shortwave spectrum; therefore, the direct influence is minimal (Dozier, 1989; Green et al., 2002). Liquid water has an indirect effect, however, by enhancing grain growth and filling voids between snow grains.

Due to the heterogeneous distribution of cryoconite the albedo varies hugely over short distances (Moustafa et al., 2015; Chandler et al., 2015, e.g.), causing differential melt. This melt can increase the aerodynamic roughness, which is

important for the turbulent heat transfer and hence the surface energy balance and melt (Nield et al., 2012; Brock et al., 2006, e.g.).
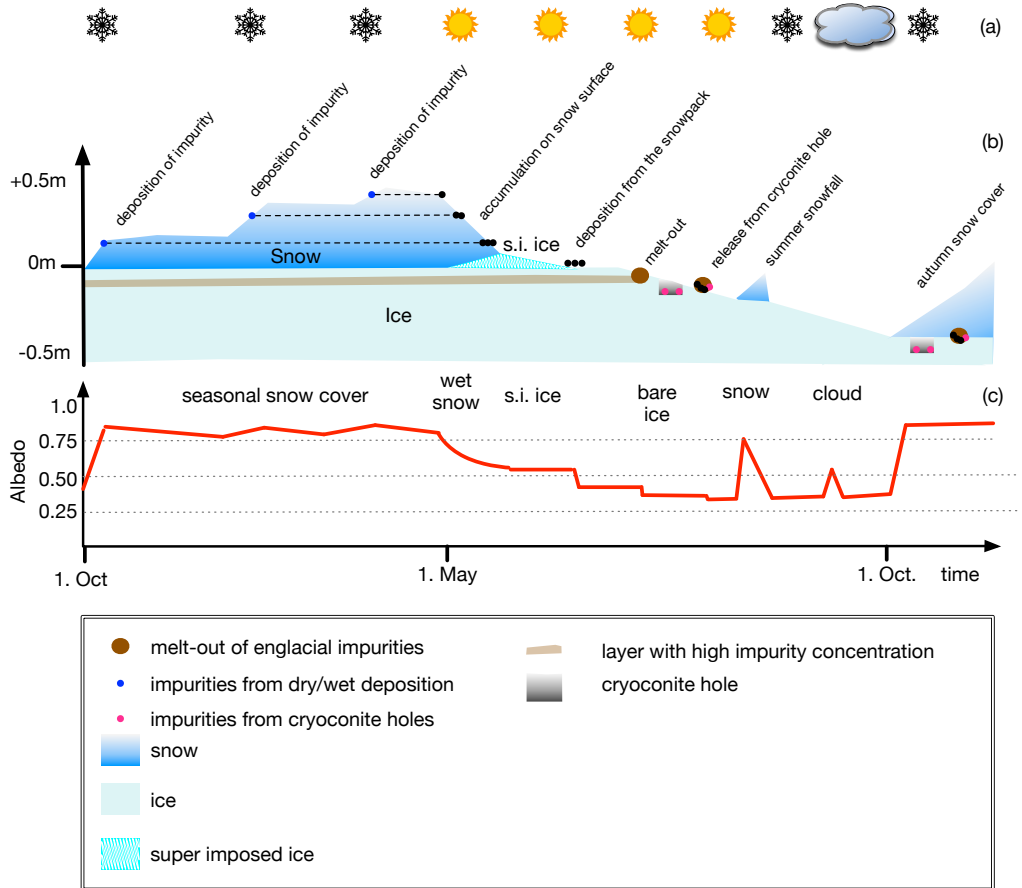
Figure 1.4: Schematic of melt-out and accumulation of impurities at a location in the ablation zone. The upper most row **(a)** indicates the atmospheric condition, e.g. snowfall, sunshine and clouds. **(b)** indicates the evolution of the snow and ice surface over one year (first of October to first of October). **(c)** indicates the albedo evolution corresponding to the surface conditions.

1.6.3 Black carbon (BC)

Black carbon (BC) is emitted during the incomplete combustion of fossil fuels, biofuels and biomass. BC is therefore natural as well as anthropogenic and is

transported by the atmosphere to polar regions or regions with glaciers. BC is a set of materials with different optical and physical properties (examples listed in Table 1 of Petzold et al. (2013)). Black carbon has a unique combination of physical properties (Bond et al., 2013): it is insoluble in water, stable up to high temperatures, strongly absorbs visible light, and exists as an aggregate of small carbon spherules.

Commonly the terms "black carbon", "soot", "elemental carbon", "light absorbing carbon", "equivalent black carbon" and "refractory black carbon" all refer to the strong light-absorbing components of carbonaceous particles originating from combustion (Petzold et al., 2013). These definitions are associated mostly with different measurement techniques or the source of the particles. Depending on the measurement method, the results for mass can differ by a factor of up to 7 (Reisinger et al., 2008; Petzold et al., 2013). Converting between different measurement methods is difficult and prone to errors (Petzold et al., 2013) because the measurement methods are linked to specific particle properties which may also depend on chemical as well as physical properties.

To avoid confusion, it is important to use the appropriate nomenclature and report details of the measurement techniques. Petzold et al. (2013) gives recommendations for nomenclature in the context of atmospheric aerosol research. The cryosphere community should use the same nomenclature in order to make measurements comparable.

By definition, soot originates from incomplete combustion. Similar to atmospheric research in the context of glaciology, soot deals with mixed and aged particles which can no longer be associated with any combustion source process. In that context, Petzold et al. (2013) recommends avoiding the terms soot or BC altogether and instead reporting fractions of BC depending on the measurement technique: refractory black carbon (rBC) for incandescence methods, elemental carbon (EC) for methods that are specific to the carbon content or equivalent black carbon (EBC) for methods linked to optical absorption.

Following the recommendation of Petzold et al. (2013), BC is still a useful qualitative description when referring to light-absorbing carbonaceous atmospheric aerosols, but for quantitative applications the term needs clarification of the measurement method used. This thesis uses the qualitative term BC. Nevertheless, using the nomenclature of Petzold et al. (2013) when reporting measurements is recommended.

BC's average atmospheric residence time ranges from 5 to 15 days according to model inter-comparison (Lee et al., 2013); therefore, BC particles can travel from hundreds to thousands of km before being deposited on the GrIS. Important

sources of BC for the GrIS are Southeast Asia and North America (McConnell et al., 2007).

Ice core BC data exists for several GrIS cores: D4, Humboldt, Summit, ACT2, Dye3, GISP2, Camp Century and NEEM (McConnell et al., 2007; Zennaro et al., 2014; Chýlek et al., 1992, 1995). Although the cores were mostly analysed for BC concentrations only from the last two centuries, Dye3 (Chýlek et al., 1992) has been analysed back 3380 years, Camp Century back 6000 years (Chýlek et al., 1987) and the NEEM core, which showed a higher resolution than the other cores, back roughly 2000 years (Zennaro et al., 2014) .

Values of BC in the GrIS snowpack have been reported in the following: Clarke and Noone (1985); Chýlek et al. (1987, 1995); Slater et al. (2002); Hegg et al. (2010); Doherty et al. (2010); Carmagnola et al. (2013); Dumont et al. (2014); Polashenski et al. (2015)

The existence of any BC measurements of ice surface samples is unknown.

1.6.4 Dust

In the context of this thesis, dust refers to windblown insoluble mineral material from continental areas. Dust is characterised by its chemical and physical properties, such as size and reflective index. Common size classes are clay ($d < 2.5\,\mu m$), silt ($2.5\,\mu m < d < 60\,\mu m$) and sand ($60\,\mu m < d < 2\,mm$).

A certain fraction of mineral dust is soluble in water. The largest soluble fraction is $CaCO_3$, which is used as a proxy for dust. Only the insoluble part of dust is relevant to the albedo.

Mineral dust originates predominantly from large deserts or semiarid areas which are subject to wind erosion. The provenance of dust particles can be derived by their mineralogy and isotopic composition. Local dust was found to be the dominant source at the Hans Tausen and Renland ice caps of Greenland, which are separate from the ice sheet (Bory et al., 2003). For the ice sheet itself, the East Asian deserts of Gobi and Taklimakan are likely the main dust source regions (Biscaye et al., 1997; Bory et al., 2003). A recent study by (Újvári et al., 2015) argues that the isotopic ratios and mineralogy of dust found in the GISP2 and GRIP ice cores could also be of central European origin.

Chemical and physical weathering produces loose fine-grain material. If the wind speed is high enough, these particles are lifted from the ground and transported in the atmosphere. The lightest particles, clay, can be transported several thousands of kilometres. During transport, particles are lost by dry and wet deposition. A clay particle with a diameter of approximately $0.7\,\mu m$ has an average atmospheric

residence time of 13 days, while silt (d=38 μm) stays in the air for only an hour (Tegen and Fung, 1994).

Another important source of dust on the ice surface is release from englacial storage (e.g Oerlemans, 1991; Bøggild et al., 1996; Wientjes et al., 2011) and outcropping of basal till (Stibal et al., 2012). The relative contribution of melt-out to the dust is one topic of Article I (see also Figure 2.15).

In the ice sheet interior (Dye 3, GRIP, NGRIP), the dust composition is essentially the same (Bory et al., 2003). Also, the variation in the dust proxy (Ca2+) of GRIP, GISP2, NGRIP is highly similar (Rasmussen et al., 2008). These cores also show a strong correlation of dust with $\delta 18O$, which is a proxy for temperature.

Dust concentration in ice cores is in antiphase with temperature. Under a warmer climate, the dust concentration is lower. Changes in source strength and atmospheric transport contribute to changes in the ice cores of the GrIS (Fischer et al., 2007). The ratio of the particulate dust concentration in the NGRIP core between the last glacial maximum and the Holocene is approximately 80 to 100 (Steffensen, 1997; Fischer et al., 2007).

Dust has been measured direct or via a proxy in the following ice cores of the GrIS: NGRIP (Ruth, 2007), GRIP (De Angelis et al., 1997; Fuhrer et al., 1999), GISP2 (which includes the only Holocene data, Mayewski et al. (1997); Taylor et al. (1997)), Camp Century (Fisher, 1979), Dye3 (Hammer et al., 1985) and Renland (Hansson, 1994). The NEEM ice core has not yet been fully analysed but should also provide Holocene data (Bigler, 2012; NEEM community members, 2009).

1.6.5 Microbes

Microbes influence the albedo of ice in two ways: by producing dark materials and aggregating particles, causing the size of the cryoconite granules to be altered. Cyanobacteria are especially responsible for the size of the cryoconite granules (Takeuchi et al., 2010). Larger and more stable grains exist where cyanobacteria are abundant (Takeuchi et al., 2010). Larger granules probably have a longer residence time and therefore, also influence the albedo indirectly (Bøggild et al., 2010; Hodson et al., 2010; Irvine-Fynn et al., 2011a). Organic matter and granule size correlate strongly, suggesting that they play a key role in determining the size and shape of the granules (Langford et al., 2010; Stibal et al., 2010). The precise biotic and abiotic processes which control cryoconite granule growth are still poorly understood (Cook et al., 2015).

Microbial activity also alters the albedo of the cryoconite granules by producing dark materials (Kohshima et al., 1993; Quesada et al., 1999; Takeuchi, 2002; Takeuchi et al., 2010; Remias et al., 2012; Tedesco et al., 2013; Takeuchi et al., 2014). The darkening effect of microbes is not yet quantified (Stibal et al., 2012; Yallop et al., 2012).

The origin of the microbes in cryoconite is currently unclear (Cook et al., 2015). A strong hypothesis is that microbes are provided by the atmosphere via both wet and dry deposition from local and distant sources (Swan, 1992; Pearce et al., 2009) similar to dust and BC. One might, therefore, argue that microbes are aerosols. Unlike dust and BC, however, microbes can reproduce, and their mass changes without the additional influx of "newcomers" from the atmosphere. Microbes can produce dark material *in situ* on the ice or snow surface and, therefore, deserve their own category.

Measurements of organic matter on the GrIS reach from 2 to 18% of the cryoconite mass (Table 1 in Cook et al. (2015)). Nevertheless, even if the mass concentrations are low, the darkening effect could still be significant. Microbes have a lower density than mineral dust; together with a high absorbance, this could lead to a substantial influence on the albedo.

Microbial cell concentration was measured in the GISP2 ice core (e.g. Miteva et al., 2004; Price, 2007; Price et al., 2009) estimated that microbial cells contributed about 1% as much mass as dust. The DYE3 (Castello et al., 1999) and recently the NEEM (Miteva et al., 2015) ice cores were also analysed for microbial cell concentrations.

Similar to BC and dust, some microbes get trapped in ice in the accumulation zone and are transported to the ablation zone over thousands of years. As much as 10% of bacteria might be able to reanimate after this long transport (Yung et al., 2007).

In conclusion, microbes are an active player in the cryoconite system on the ice surface and influence the albedo in different ways. Their dynamics and albedo-lowering capacity are currently not well understood; therefore, microbial activity is not explicitly included in this thesis.

1.6.6 Brown carbon (BrC) and organic carbon (OC)

Brown carbon (BrC) is light-absorbing organic matter of various organic substances which appears brown rather than black (Andreae and Gelencsér, 2006). The brown colour is associated with non-uniform absorption over the visible spectrum.

Brown carbon has various origins: soil humic substances, humic-like substances (HULIS) and tarry materials from combustion (Petzold et al., 2013).

According to this definition, the light-absorbing materials produced by microbes are BrC, although they are not explicitly called brown carbon in the glaciological literature. Similar to BC, brown carbon is not one specific material but a big set of materials with specific properties.

Brown carbon is sometimes used equivalently with organic carbon (OC) (Dang et al., 2015; Doherty et al., 2010, e.g.). Organic carbon, however, includes all carbon compounds where carbon is combined with hydrogen or other elements. Therefore, brown carbon is a subset of OC.

1.6.7 Tephra

Tephra is a collective term for all airborne volcanic ejecta (Thorarinsson, 1974). In the context of this thesis, only ash (< 2 mm) is relevant. Volcanic tephra is usually identifiable and excluded from the ice core records (e.g. Narcisi et al., 2010). Greenland ice cores are mostly analysed for acid layers from the fallout of aerosols emitted by volcanic eruptions. For example, 1927 volcanic events have been detected in the sulphate record of the NGRIP core between approximately 10 ka and 110 ka before the year 2000 (Chalmas (2004), as cited in Abbott and Davies (2012)). Only 45 tephra horizons have been identified in the ice cores (Abbott and Davies, 2012), which indicates the very limited amount of volcanic ash reaching the GrIS. Recently, "cryptotephra", which are not visible to the naked eye, have been studied in Greenland's ice cores (Abbott and Davies, 2012). The reasons why the tephra concentration on the GrIS is so low are the distance to significant volcanic regions and dominant wind patterns. Even though the volcano on Jan Mayen is close, only one study found its material in a Greenland ice core (Abbott and Davies, 2012). Iceland is responsible for most of the ice core records. Of the 45 tephra layers, 37 have been attributed to Icelandic eruptions (Abbott and Davies, 2012; Grönvold et al., 1995). No tephra of the large equatorial eruptions such as Toba, Krakatoa or Pinatubo has been found in Greenland's ice cores, although peaks of sulphate linked to those eruptions have been identified (Abbott and Davies, 2012).

Nevertheless, for glaciers close to active volcanoes, tephra has a significant impact on albedo (e.g. Möller et al., 2014) and melt (e.g. Julio-Miranda et al., 2008) up to a certain ash layer thickness (Dragosics et al., 2016). An albedo reduction of 0.01 is reached at a mass fraction of 10 ng g^{-1} for ice and 1000 ng g^{-1} for snow (Dadic et al., 2013). Since the number of visible ash layers in Greenland's

ice cores is small and the mass fraction to reach a significant lowering of ice's albedo is quite high, volcanic ash is not addressed in this thesis.

1.6.8 Micrometorites

Nordenskiöld originally proposed that cryoconite was of extraterrestrial origin. In fact, the influx of micrometeorites on the GrIS is in the order of 10^{-6} g m^{-2} per year (Maurette et al., 1987), about 1000 times lower than the current atmospheric influx of BC (0.001 g m^{-2}, Lee et al. (2013)). Therefore, assuming that the influx is stable, micrometeorites can be neglected.

1.6.9 Non-absorptive aerosols: sea salt, sulphate and nitrate

The majority of natural aerosols are sea salts and natural sulphates (Satheesh and Krishna Moorthy, 2005; Stocker et al., 2013). Both are non-absorbing and therefore could only influence the albedo of snow and ice by scattering. To the author's knowledge, this effect has not been studied in snow or ice but is probably minor.

1.7 Tracer transport

Impurities are transported within the ice from the accumulation zone towards the ablation zone. These impurities do not interact with the flow while in transit and can therefore be seen as a passive tracer. Another passive tracer in ice is δ^{18}O, which is the ratio of oxygen isotopes relative to a defined standard and an important proxy of past surface temperatures (e.g. Masson-Delmotte et al., 2008).

In order to accurately predict when and where an impurity emerges, the age of the ice needs to be computed. This computation is complex because first, the geometry of the ice sheet needs to match the present day geometry and second, the age of the ice needs to be accurate in order to obtain the impurity concentration. This concentration is calculated by linking the age of the ice to a time series of impurity concentration obtained from the ice cores. Calculating the age of the ice is still a challenging task.

Clarke and Marshall (2002) and the follow-up papers (Lhomme et al., 2005a,b; Clarke et al., 2005) used a semi-Lagrangian scheme with first-order accuracy. Article III will show that the first-order method produces the same results as a second-order method of the ice sheet interior. However, in the ablation zone, which

is the area of interest for impurity melt-out, the second-order scheme produces different results.

Tracer transport is of interest not only for the melt-out of impurities but also for the global cycle of oxygen isotopes and the emergence of persistent organic pollutants. Bogdal et al. (2010) used a 2D glacier-flow model for predicting the emergence of persistent organic pollutants with a Eulerian transport scheme and a full Stokes model. The studies, based on Clarke and Marshall (2002), focused on oxygen isotopes in the ice sheet interior. Therefore, Article II is the first study that considers impurity transport, melt-out and surface accumulation.

1.8 Motivation and objectives

Shortwave radiation is the major component of the surface energy balance during melt, and broadband albedo is a major factor in the SMB (see references in section 1.2). Therefore, albedo should be a dynamic component of models aiming to predict sea level rise. A dynamic surface albedo component of a glacier or ice sheet needs to include the albedos of both snow and ice.

Currently, snow albedo is more commonly studied because of the large areas which are covered by snow at some point during the year and the effect of snow albedo on climate (Hansen and Nazarenko, 2004; Flanner et al., 2007). Snow albedo models are becoming increasingly complex, consisting of multiple layers and accounting for grain growth, meltwater percolation, refreezing and impurities (Flanner and Zender, 2006; Gent et al., 2011; Rae et al., 2012; Gabbi et al., 2015).

Ice albedo is known to be highly variable over space and time, but models still treat ice albedo as uniform and constant (e.g. Mernild et al., 2010; Rae et al., 2012) or a constant in time (e.g. Gent et al., 2011; Oaida et al., 2015). Some models use intricate snow albedo schemes but still treat ice albedo as a non-evolving constant parameter (e.g. Vizcaino et al., 2013; Franco et al., 2013).

Additional motivation to study ice albedo is its increasing importance in a warming climate. This importance is because ice will be exposed over wider areas and for longer periods. More ice is exposed as the equilibrium line moves to higher elevations and ice is exposed longer as snow melts earlier (Brutel-Vuilmet et al., 2013; Vizcaino et al., 2014). Already the darkening of the GrIS is partly attributed to the longer exposure of ice as well as impurities and snow grain growth (Tedesco et al., 2016). Another indicator for the expansion of the bare ice area was the 2012 event when melt occurred almost everywhere on the GrIS (Nghiem et al., 2012).

These facts lead to the main objective of this thesis: developing a model framework which includes the following processes: ice dynamics, surface mass balance (which depends on albedo,) impurity melt-out and accumulation, impurity transport within the ice flow and ice albedo depending on both englacial and supraglacial impurities (see Figure 1.5).
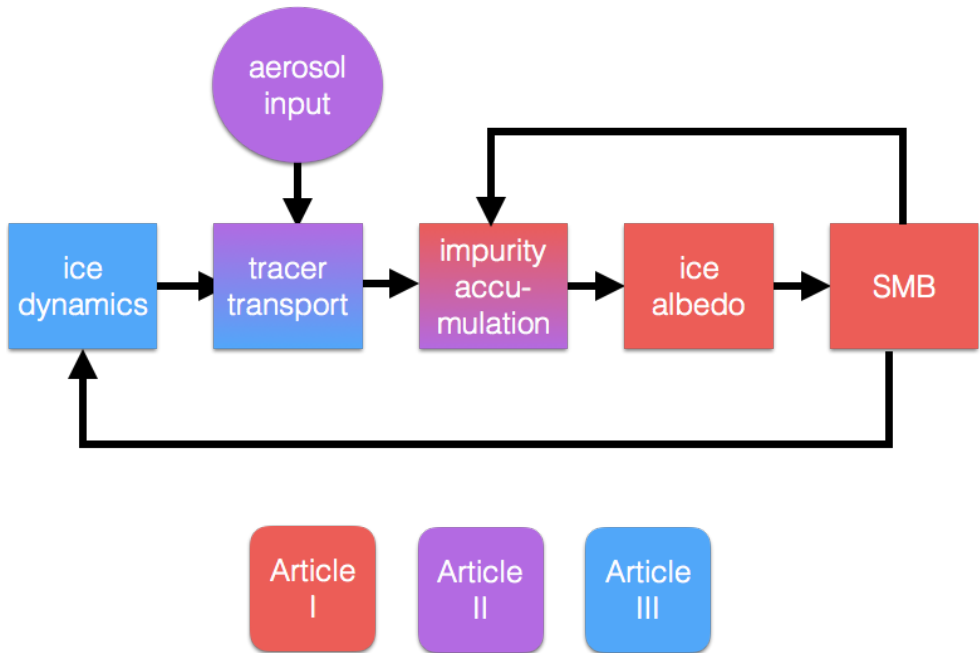
Figure 1.5: Schematic overview of the model framework and organisation of the thesis. Each article focuses on different parts of the framework, as indicated by the colour code.

Other objectives are:

- Investigating the role of melt-out against the atmospheric deposition of impurities.

- Deriving the residence time of impurities on the ice sheet surface.

- Investigating the role of impurity melt-out on ice albedo and ice sheet volume under warmer conditions.

- Implementing and testing a tracer transport scheme of second-order accuracy in a 3D ice sheet model.

The current state of research of impurity dynamics, especially BC, is summarised by Hodson (2014) who recommends developing a 3D model which includes impurity transport and melt-out. This thesis is a first step towards a complete model where impurity transport and melt-out are included in a 2D model (Article I and II) and the transport in a 3D model is developed (Article III).

Figure 1.5 shows the model framework and a colour code for each article. Each article focuses on different parts of the framework. Article I (chapter 2) covers impurity melt-out, impurity accumulation on the surface and the effect of dust and BC on ice albedo and SMB. Article II (chapter 3) introduces the whole framework and focuses on the aerosol input, impurity transport and feedback between melt-out, ice albedo and melt. Article III (chapter 4) is a technical paper dealing with ice dynamics and tracer transport[1].

---

[1] Article III is based on my master's thesis. I wrote the article during my PhD and added additional analysis.

Chapter 2

Article I

Goelles, T. and Bøggild, C. E.

Albedo reduction of ice caused by dust and black carbon accumulation from melt-out and atmospheric deposition

Abstract

Surface melt in the ablation zone is controlled by atmospheric temperature and surface albedo. Impurities accumulate on the ice surface and lower the albedo of ice. Non-biological impurities, such as mineral dust and black carbon, accumulate by dry or wet deposition and by melt-out. The darkening effect of accumulating impurities on the ice surface is currently not included in surface mass balance models and sea level projections. We present a model framework which includes impurity melt-out and accumulation, the effect of clouds and the angle of the sun on albedo and ultimately surface mass balance. The main source of dust on the ice surface is melt-out from dust deposited during glacial periods, whereas current atmospheric deposition contributes insignificantly. While for black carbon the atmospheric deposition dominates at melt rates below one meter. Runoff of impurities is in the range of one permille per day, which leads to a residence time of decades on the ice surface in which the albedo is lowered and melt is enhanced.

2.1 Introduction

The increased mass loss of the Greenland ice sheet (GrIS) since 2009 is mainly caused by an increase in surface melt and runoff (Enderlin et al., 2014). Surface melt is largely determined by the amount of absorbed shortwave radiation (Van den Broeke et al., 2008), which is governed by the surface albedo. Hence, the broadband albedo (from now on just referred to as albedo) has been identified as a major control on the surface mass balance (SMB) of the GrIS (Bougamont et al., 2005; Tedesco et al., 2011; van Angelen et al., 2012).

The albedo of ice varies highly over space and time (e.g. Bøggild et al., 2010; Chandler et al., 2015), but in most model studies ice albedo is still treated as a uniform constant (e.g. Mernild et al., 2010; Rae et al., 2012) or as constant over time (e.g. Noël et al., 2015). Snow albedo, on the other hand, is often modelled by multi-layer snowpack and radiative transfer models, considering grain growth and impurities (e.g. Gent et al., 2011; Lipscomb et al., 2013; Oaida et al., 2015). Models of ice albedo are still at their infancy.

The highest melt rates of the GrIS are observed in the ablation area, where ice is exposed at some point of the year, after the seasonal snow has disappeared. This goes in hand with a drop in surface albedo because the albedo of ice is significantly lower than that of snow (e.g. Moustafa et al., 2015). The duration and area of exposed ice will increase under a warmer climate (Brutel-Vuilmet et al., 2013; Vizcaino et al., 2014) as snow melts earlier and the equilibrium line moves to higher elevations. Therefore, ice albedo will be of more importance for the SMB of the GrIS in the future.

We present the first SMB model which takes the effect of impurity accumulation on ice albedo into account. The ice albedo is part of the surface albedo scheme which includes the seasonal change between snow and ice surface. The design goal for the model is that it can be used in stand-alone ice sheet and glacier models, as well as in conjunction with an atmospheric model. The temperature and precipitation needs to be prescribed when used in stand-alone mode, while these are otherwise provided by the atmospheric model. This study focuses on the stand-alone application and the model framework is applied and tested on the western margin of the GrIS.

First we begin with an outline of impurities on snow and ice, and the description of the model test site. In Section 2.2 we present the model equations and parameters, and the calibration procedure, followed by model results. We conclude by

discussing the result of model simulations at two locations and the role of impurity melt-out.

2.1.1 Albedo and impurities

Absorption of ice at visible wavelengths is very weak, therefore small amounts of highly absorbent impurities have a big effect on snow and ice albedo (Wiscombe and Warren, 1980; Warren and Wiscombe, 1980; Warren and Brandt, 2008). The most absorbent impurity is black carbon (BC), which is about 200 times more absorbent than mineral dust (Dang et al., 2015). BC particles are highly absorptive in the visual range, where the solar radiation is greatest. In addition to the aerosols dust and BC, microbes may influence the albedo by aggregating material (Takeuchi et al., 2001) and by production of dark materials (Takeuchi, 2002; Remias et al., 2012). Brown-black ice algae can potentially decrease the albedo of ice by up to 40% relative to clean ice (Yallop et al., 2012). Despite the potentially high influence of microbes, their dynamics and exact effect on albedo are not well understood (Stibal et al., 2012; Yallop et al., 2012).

Non-biological impurities on the ice surface accumulate by dry or wet deposition, by release of impurities in the snowpack or by melt-out of englacial impurities. The ice itself acts as a reservoir of mineral dust and BC (Reeh et al., 1991; Bøggild et al., 1996). These englacial impurities travel with the ice towards the ablation zone, where they melt-out and contribute to the impurity mass on the ice surface (e.g. Oerlemans, 1991; Bøggild et al., 1996; Klok and Oerlemans, 2002; Oerlemans et al., 2009). The accumulated impurities on the ice surface lower the albedo for several years, because they are preserved under the winter snow cover, and re-emerge in spring.

The effect of impurities on snow, on the other hand, is short. A substantial snow-fall in winter resets the snow albedo to the high values of fresh dry snow (Dumont et al., 2014). In spring, when snow melts, the impurities tend to concentrate at the snow surface which amplifies the impact of impurities on snow albedo (Doherty et al., 2010, 2013). However, the impact at the ablation zone is still rather short because the snow cover is thin and therefore the period of snow melt is short. After all snow has melted the impurities of the snowpack are released onto the ice surface.

Typical values of BC concentrations, found in snow on the GrIS, are around 3 ng g^{-1} with peaks of 20 ng g^{-1} (Dumont et al., 2014). Values of dust concentration in snow can reach up to 500 ng g^{-1} (Dumont et al., 2014), which has about the same effect on albedo as 2.5 ng g^{-1} BC. Dust concentration in ice cores are up

to 9000 ng g^{-1} Ruth et al. (2003) and of BC up to 16 ng g^{-1} (McConnell et al., 2007). While the surface concentration of impurities on ice range from 16 g m^{-2} up to 1.4 kg m^{-2} (Bøggild et al., 2010).

2.1.2 The K-transect in western Greenland

The so-called "K-transect" (also known as Søndre Strømfjord transect) is located on the western margin of the GrIS at 67°N (Fig. 2.1) and has been the target of numerous field campaigns. We chose this location as the test site for the model because of available SMB measurements as well as continuous automatic weather station observations.
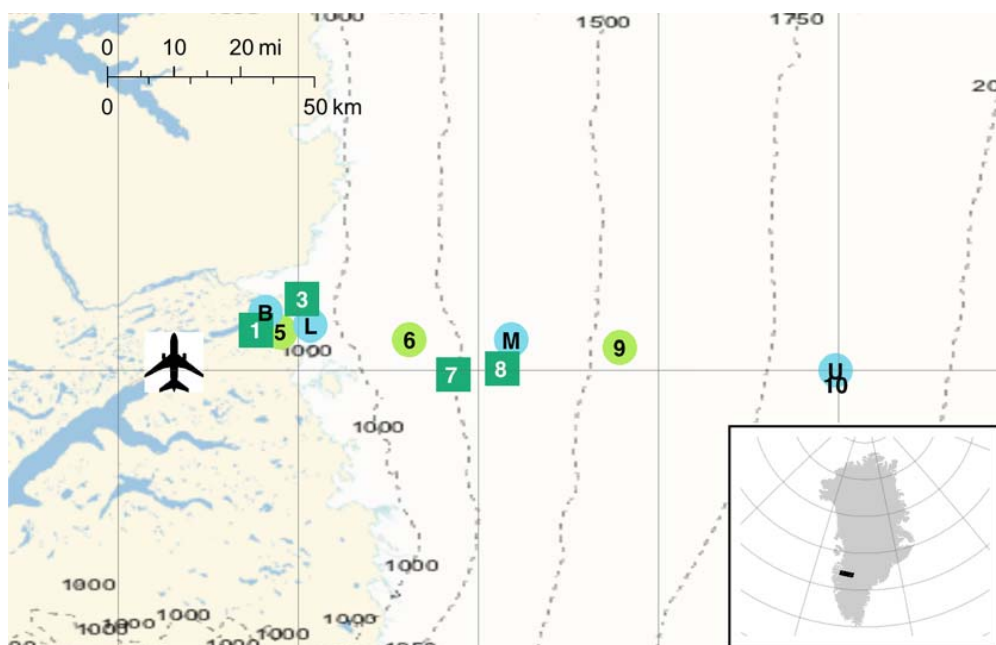

Figure 2.1: Weather stations and sampling sites at the K-transect in western Greenland, near the Kangerlussuaq airport. Blue circles mark the PROMICE weather stations operated by GEUS (without their prefix "KAN_") and the green circles mark the ones operated by IMAU (without their prefix "S"). The squares mark additional mass balance sites where ice samples have been taken (Wientjes et al., 2012). Station S9 is located near the equilibrium line and sites S6, S7, S8 and KAN_M are located in the "dark region" with lower albedos.

Accumulation in the K-transect is low compared to other parts of the GrIS (Burgess et al., 2010). At low elevation near station S5 snow is redistributed by wind into gullies and crevasses (Van den Broeke et al., 2008), causing ice exposure throughout the melting season. While at higher stations up to station S9, near the equilibrium line, ice is covered by snow in the beginning of the melt season and exposed later on.

It is also an interesting area because a "dark region" persists below the equilibrium line each melt season. The region is about 30 km wide and starts at approximately 30 km away from the margin (Wientjes and Oerlemans, 2010). Previously the cause of this dark region was believed to be meltwater (Zuo and Oerlemans, 1996), but now is attributed to dust (Wientjes and Oerlemans, 2010) and carbonaceous particles (Wientjes et al., 2012). This dark area, the available data and the ice exposure makes the K-transect an ideal test location for our model.

2.2 Model description

2.2.1 Model framework and setup

A full surface energy balance model is not feasible because it requires information about winds, cloud cover, relative humidity, etc. which are not available in stand-alone ice sheet models. Therefore, the centrepiece of the SMB model is a simplified energy balance which takes albedo into account. Our model framework consists of seven components shown in Figure 2.2 and the common parameters are listed in Table 2.1. The *temperature and precipitation parameterisation* and *impurity accumulation* components are our own developments, the snow and ice albedo component are largely based on Gardner and Sharp (2010), and the other components are based on Robinson et al. (2010).

The model simulates surface albedo, impurity loadings, snow thickness and SMB for one square meter on an ice sheet or glacier. It is realised in Mathematica (version 10, Wolfram Research, Inc., 2014) using self-coded solvers for the differential equations, with a time-step of one day. The following sections describe each component in the order of the flow chart.
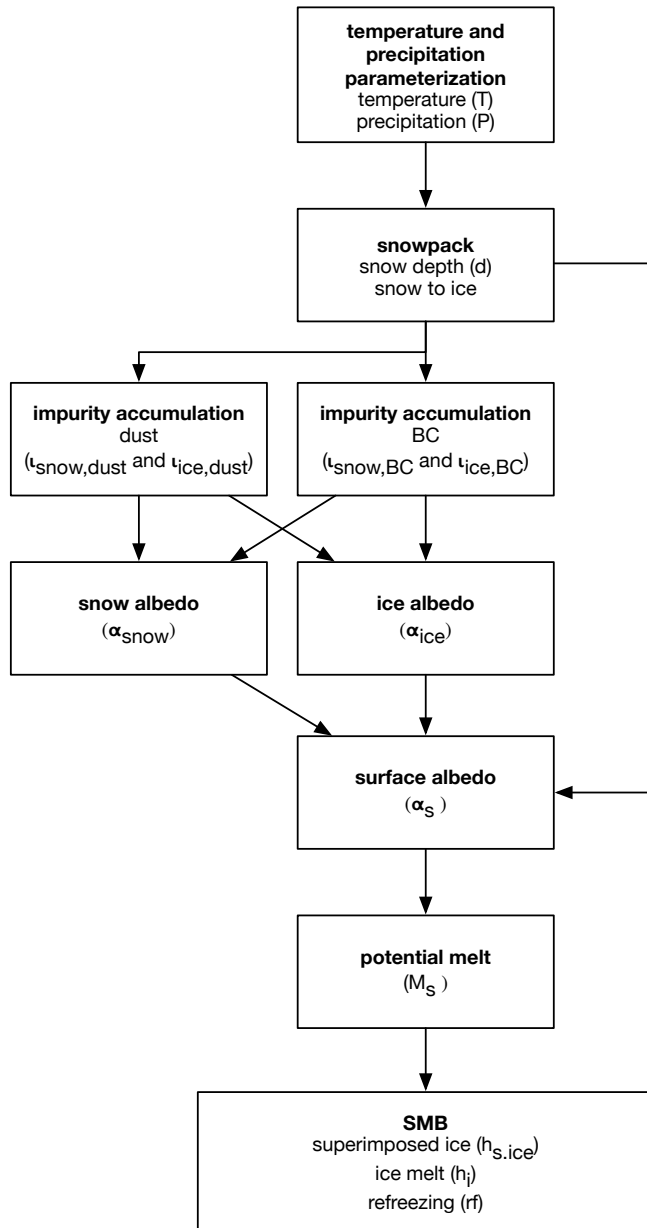
Figure 2.2: Flow chart of the surface albedo and surface mass balance model for one time-step of one day.

Table 2.1: Standard physical parameters.

Symbol	Constant	Value	Unit
ρ_{ice}	Density of ice	910	kg m^{-3}
ρ_{w}	Density of water	1000	kg m^{-3}
$t_{\odot,\text{start}}$	Start of summer	121	day of year
$t_{\odot,\text{end}}$	End of summer	244	day of year
λ	Longwave radiation coeff.	10	$\text{W m}^{-2}\,\text{K}^{-1}$
c	Melt model coefficient	-55	W m^{-2}
r_{max}	Max. fraction of refreezing	0.6	–
L_{m}	Latent heat for melting	$3.34\ 10^5$	J kg
d_{eff}	Effective depth on ice	5	m
$\alpha_{\hat{S},ds}$	Dry snow albedo[a]	0.65	

[a]zenith angle 0, no clouds

2.2.2 Temperature and precipitation parameterisation

The near-surface temperatures at the ablation zone of the GrIS are stable during the summer months due to the cooling effect of melting ice. Therefore, temperatures are stable during the summer and fluctuate during the winter months. Hence, we did not use a sinusoidal parameterisation, which is normally used (e.g. Reeh, 1991), but a trapezoid shape:

$$
T = \begin{cases}
T_{\oplus} & t_{\odot,\text{start}} \leq t \leq t_{\odot,\text{end}} \\
t \cdot \varsigma - t_{\odot,\text{start}} \cdot \varsigma + T_{\oplus} & t < t_{\odot,\text{start}} \\
-t \cdot \varsigma + t_{\odot,\text{end}} \cdot \varsigma + T_{\oplus} & t > t_{\odot,\text{end}}
\end{cases}
\tag{2.1}
$$

where $T_{\oplus}$ is the mean of all temperatures above $0\,°\text{C}$. The first day of the summer $t_{\odot,\text{start}}$ is set to May 1 and the last day with positive temperatures $t_{\odot,\text{end}}$ is set to September 1. The non-summer temperatures are defined by the slope ς in $°\text{C}$ per day when the time t is in days. This parameterisation of the negative temperatures is sufficient because melt is unaffected by them.

The precipitation rate is parameterised by the annual mean precipitation rate $P = \overline{P}$. This is justifiable because the snow depth is unaffected by high frequency

fluctuations of precipitation. The disadvantage of this simple parameterisation is that it makes it impossible to resolve individual snowfall events. Therefore, it is also impossible to account for snow grain growth as well as summer snowfall.

2.2.3 Snowpack

Snow depth (d) is required for the final SMB, and in order to distinguish between snow and ice surface. It is calculated by a balance between the solid precipitation rate P_{solid} and the melt rate M_s (Robinson et al., 2010):

$$\frac{\mathrm{d}}{\mathrm{d}t}d = P_{solid} - M_s, d \in (0, d_{max})$$ (2.2)

If the snow depth exceeds $d_{max} = 5\,\mathrm{m}$ w.e. (Robinson et al., 2010; Fitzgerald et al., 2012) the snow depth is reset to 5 meters and the surplus amount is added to the ice thickness. This accounts for the snow to ice metamorphism in the accumulation zone. The solid precipitation rate P_{solid} in Eq. (2.2) is based on a temperature-dependent fraction $f(T)$ and the total precipitation rate P (Robinson et al., 2010):

$$P_{solid} = P \cdot f(T)$$ (2.3)

where the surface temperature-depending fraction $f(T)$ is empirically based on data of Greenland (Bales et al., 2009; Calanca et al., 2000) and states that below a minimum temperature ($T_{min} = -7\,^{\circ}\mathrm{C}$) all precipitation is snow and above a maximum temperature ($T_{max} = +7\,^{\circ}\mathrm{C}$) rain:

$$f(T) = \begin{cases} 1 & T < T_{min} \\ 0 & T > T_{max} \\ \cos\left(\frac{T-T_{min}}{T_{max}-T_{min}}\right)\left(\frac{\pi}{2}\right) & T_{min} < T < T_{max} \end{cases}$$ (2.4)

2.2.4 Impurity accumulation

Particulate impurities such as BC and mineral dust as well as microbes have four different sources (Fig. 2.3):

- *atmosphere – distant sources*: (k_I) by dry or wet deposition,

- *atmosphere – local sources*: (k_{II}) by regionally transported material from the surrounding tundra,

- *flow*: (k_{III}) by transport from the accumulation zone to the ablation zone where impurities melt-out,

- *biological*: (k_{IV}) by local biological production of dark material on the ice or snow surface.

The magnitude of each source depends on the impurity species. Where the biological source k_{IV} is only relevant for organic matter associated with microbial production. Organic matter was found to contribute only about 5 % to the impurity mass on the ablation zone of the GrIS (Bøggild et al., 2010; Wientjes et al., 2011; Takeuchi et al., 2014). Due to its relative low concentration and unknown absorption we omit the biological production for now. Nevertheless, we still prepare the impurity accumulation in a way that biological activity can be included in the future.

The atmospheric sources (k_I and k_{II}) contribute to BC and dust accumulation both in the ice sheet interior and at the margin. While the melt-out of englacial impurities, source k_{III}, only contributes in the ablation zone when ice melts. The following equations are valid for BC (n=BC) and dust (n=dust).

Both atmospheric sources contribute directly to the impurity mass inside the snowpack $\iota_{snow,n}$ (ng m^{-2}) as well as the local biological production. We assume that impurities stay within the snowpack once they are inside. Therefore, the impurity concentration inside the snowpack is described by:

$$\frac{d\iota_{snow,n}}{dt} = \begin{cases} k_{I,n}(t) + k_{II,n}(t) + k_{IV,n}(t) & d > 0 \\ 0 & d = 0 \end{cases} \tag{2.5}$$

As ice is exposed (snow depth $d = 0$) englacial impurities as well as the atmospheric sources and local production all contribute to the impurity mass on the ice surface $\iota_{ice,n}$ (ng m^{-2}). The impurity accumulation is counteracted
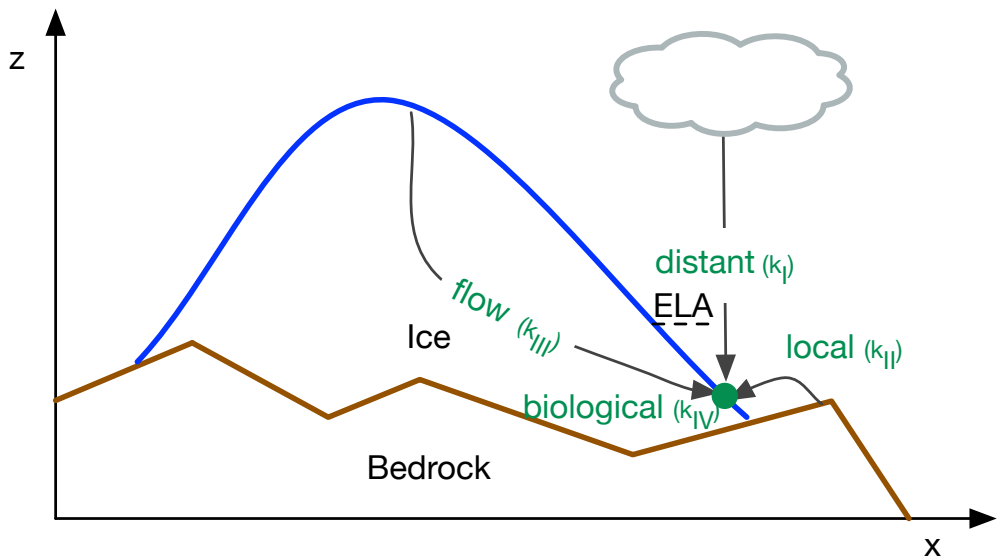
Figure 2.3: Cross section through an ice sheet showing the four different sources of impurities in the ablation zone. ELA stands for equilibrium line altitude.

by a reduction term ($r_{ice}(t)\, \iota_{ice,n}$), which describes removal by meltwater and is assumed to be the same for dust and BC. The removal by rain is not directly accounted for, since individual rainfall events are not captured by the precipitation parameterisation. We assume no resuspension of impurities, because the surface on which they reside is either wet or frozen. Further, we assume that once the snow cover disappears all the impurities in the snowpack get instantly added to the impurity content of the ice surface and no impurity flux from the ice towards the snowpack:

$$\frac{d\iota_{ice,n}}{dt} = \begin{cases} 0 & d > 0 \\ k_{I,n}(t) + k_{II,n}(t) + k_{III,n}(t) + \\ +k_{IV,n}(t) - r_{ice}(t)\iota_{ice,n} & d = 0 \end{cases} \tag{2.6}$$

The contribution of melt-out of englacial impurities $k_{III,n}(t)$, which are transported by ice flow, depends on the melt rate of ice and the englacial impurity concentration [$\iota_{englacial,n}$] (in ng g^{-1} or ppb). We assume that the impurity content in superimposed ice ($h_{s.ice}$) is 0, since observations indicate a very small impurity concentration in superimposed ice (Chandler et al., 2015) and impurities accumulate on the snow surface during melt:

$$k_{III,n}(t) = \begin{cases} [\iota_{englacial,n}]1000\frac{dh_{ice}}{dt}\rho_{ice} & h_{s.ice} = 0 \\ 0 & h_{s.ice} > 0 \end{cases} \tag{2.7}$$

in ng m^{-2} and where h_{ice} is the thickness of ice (see 2.2.9) and ρ_{ice} is the density of ice in kg m^{-3}.

2.2.5 Ice albedo

The albedo of ice depends on its specific surface area $\hat{S}$, the effect of impurities ($d\alpha_c$), the zenith angle of the sun ($d\alpha_{\theta_z}$) and the effect of clouds ($d\alpha_{clouds}$). Gardner and Sharp (2010) developed a parameterisation based on experiments with a radiative transfer model of snow and ice coupled to a similar model of the atmosphere:

$$\alpha_{\text{ice}} = \alpha_{\hat{S}} + \text{d}\alpha_{\text{c}} + \text{d}\alpha_{\theta_z} + \text{d}\alpha_{\text{clouds}} \tag{2.8}$$

Where $\alpha_{\hat{S}}$ is the albedo of clean ice with a zenith angle of 0 and no clouds. It is determined by the specific surface area $\hat{S}$ in $\text{cm}^2 \ \text{g}^{-1}$ of ice, which depends on the size and distribution of air bubbles and cracks (Gardner and Sharp, 2010):

$$\alpha_{\hat{S}} = 1.48 - \hat{S}^{-0.07} \tag{2.9}$$

The albedo reduction due to BC is modelled by the equation (Gardner and Sharp, 2010):

$$\text{d}\alpha_{\text{c}} = \max\left(0.04 - \alpha_{\hat{S}}, \frac{-c^{0.55}}{0.16 + 0.6\,\hat{S}^{0.5} + 1.8\,c^{0.6}\,\hat{S}^{-0.25}}\right) \tag{2.10}$$

which is designed for concentrations of BC (c in ppmw) and the effect of dust can be included by adding an BC equivalent term. We use a scaling factor of 1/200 to account for the lower absorption of dust (Gardner and Sharp, 2010; Dang et al., 2015). We define an effective concentration of BC and dust, which accounts for both englacial impurities and impurities located on the ice surface:

$$c = [\iota_{\text{eff,BC}}] + [\iota_{\text{eff,dust}}] \cdot 1/200 \tag{2.11}$$

where $[\iota_{\text{eff,n}}]$ is the effective aerosol concentration in ppmw, which depends on the englacial concentration as well as the *active* component of the impurities located on the ice surface. A certain fraction of impurities can be inside cryoconite holes, and therefore shielded from the low-standing sun (Bøggild et al., 2010). This is expressed by the active fraction $\mathcal{F}$, which is assumed to be the same for BC and dust, in the equation:

$$[\iota_{\text{eff,n}}] = [\iota_{\text{englacial,n}}] + [\iota_{\text{ice,n}}] \cdot \mathcal{F} \tag{2.12}$$

where only the active fraction $\mathcal{F}$ contributes to the ice albedo reduction. A value of one means that all impurities are dispersed on the ice surface and therefore all impurities reduce the ice albedo directly.

The impurity accumulation on ice (Eqn. 2.6) is calculated in ng per square meter, while Equation 2.10 requires the fractions of weight (ppmw). We therefore use the following equation to convert between the two quantities:

$$[\iota_{\text{ice,n}}] = \frac{\iota_{\text{ice,n}}}{\rho_{\text{ice}} \, d_{\text{eff}}} \, 10^6 \tag{2.13}$$

where d_{eff} is the effective depth (in meters). This assumes that impurities on the ice surface have an equivalent effect as the same amount of impurities uniformly distributed in the ice over the effective depth. The effective depth is derived from the extinction coefficient of ice and is set to 5 meters. At this depth less than one permille of the original energy remains, based on an extinction coefficient for clear white ice of 1.6 m^{-1} (Bøggild et al., 1995).

Clouds

Clouds cause a spectral shift in incident radiation which increases the albedo with increasing cloud optical thickness τ. The change of albedo caused by clouds is obtained by (Gardner and Sharp, 2010):

$$\text{d}\alpha_{\text{clouds}} = \frac{0.1\tau(\alpha_{\hat{s}} + d\alpha_{\text{c}})^{1.3}}{(1 + 1.5\tau)^{\alpha_{\hat{s}}}} \tag{2.14}$$

which depends, besides the cloud optical thickness τ, on the specific surface area and the impurity content.

The effective cloud optical thickness at the K-transect varies between 4 and 14 with an annual mean of 9.0 at S5, of 8.4 at S6 and of 8.0 at S9 (Van den Broeke et al., 2008). Hence, the cloud optical thickness decreases with elevation h (in m) and is expressed by (see Figure S1a in the supplements):

$$\tau = 9.45 - 0.001 \cdot h \tag{2.15}$$

and is constant over the year.

Zenith angle of the sun

Albedo increases with increasing zenith angle because light is less likely to penetrate deep into ice or snow. Hence, the path length is shorter and the albedo is higher. This is parameterised by (Gardner and Sharp, 2010):

$$d\alpha_{\theta_z} = 0.53\alpha_{\hat{S}}(1 - (\alpha_{\hat{S}} + d\alpha_c))(1 - \cos\theta_z)^{1.2} \tag{2.16}$$

where θ_z is the zenith angle. The influence of the zenith angle is highest in spring and autumn and causes an albedo increase of 0.13. At the same time solar radiation is low and therefore the impact of albedo on melt is also low. In mid-summer the effect at the K-transect is around 0.05 for clean ice and 0.08 for ice with 0.1 ppm BC (see Figure S1b in the supplements). Hence, $d\alpha_{\theta_z}$ is higher with higher impurity loading. Due to the shorter path length it is less likely that solar radiation encounters impurities and therefore the albedo is higher with high zenith angles. Nevertheless, the overall effect of impurities on albedo is still negative, but weakened when the zenith angle is high.

2.2.6 Snow albedo

We keep snow albedo unaffected by impurities in this study, since the concentrations are low and the effect on surface albedo in the ablation zone is short (see also Figure S2 in the supplements). Other than that, the same equations as for ice are used and the effect of clouds and the zenith angle (Eqn. 2.14 and 2.16) are still captured:

$$\alpha_{\text{snow}} = \alpha_{\hat{S}} + d\alpha_{\theta_z} + d\alpha_{\text{clouds}} \tag{2.17}$$

The precipitation rate is constant due to the parameterisation required for a stand-alone model. Therefore, individual snowfall events can not be captured. Thus, the effect of grain growth is approximated by two distinct values of $\alpha_{\hat{S}}$ in Equation 2.17: one for dry snow ($\alpha_{\hat{S}} = \alpha_{\hat{S},\text{ds}}$) and one for wet snow ($\alpha_{\hat{S}} = \alpha_{\hat{S},\text{ws}}$). Wet snow appears if there was melt at the previous time-step.

2.2.7 Surface albedo

The albedo at a geographical point on a glacier or ice sheet is determined by the surface type, clouds, the solar zenith angle and impurities. If the snow depth is below a critical mark d_{crit} the surface albedo is still influenced by the darker underlaying ice (see Figure 2.4). Above the critical snow depth d_{crit} the surface albedo is equivalent to the the albedo of α_{snow} (based on Van den Berg et al. (2008); Robinson et al. (2010)):

$$\alpha_s = \begin{cases} \alpha_{ice} & d = 0 \\ \alpha_{ice} + \frac{d}{d_{crit}}(\alpha_{snow} - \alpha_{ice}) & 0 < d < d_{crit} \\ \alpha_{snow} & d \geq d_{crit} \end{cases} \qquad (2.18)$$

This equation allows the snow albedo to be lower than the ice albedo, which could be the case, although rare, when debris rich wet snow covers clean ice.

2.2.8 Potential melt

Many parameterisations of surface melt with different levels of complexity exist, but only a few directly account for albedo. We use a simplified energy-balance model based on Oerlemans (2001) to derive the potential melt rate M_s:

$$M_s = \frac{1}{\rho_w L_m}[\tau_a(1 - \alpha_s)S_{TOA} + c + \lambda T] \qquad (2.19)$$

where ρ_w is the density of water, L_m is the latent heat of melting, τ_a is the transmissivity, S_{TOA} the insolation on top of the atmosphere, c and λ are empirical parameters, and T is the surface air temperature. The term $c + \lambda T$ is a parameterisation of the longwave radiation and turbulent heat flux optimised for Greenland (Robinson et al., 2010, 2011; Fitzgerald et al., 2012).

The term $\tau_a(1 - \alpha_s)S_{TOA}$ describes the net shortwave radiation and requires only the insolation on top of the atmosphere, which can be calculated for any time and location (Liou, 2002). The transmissivity τ_a is based on net shortwave radiation data and is a linear fit with elevation h in meters:
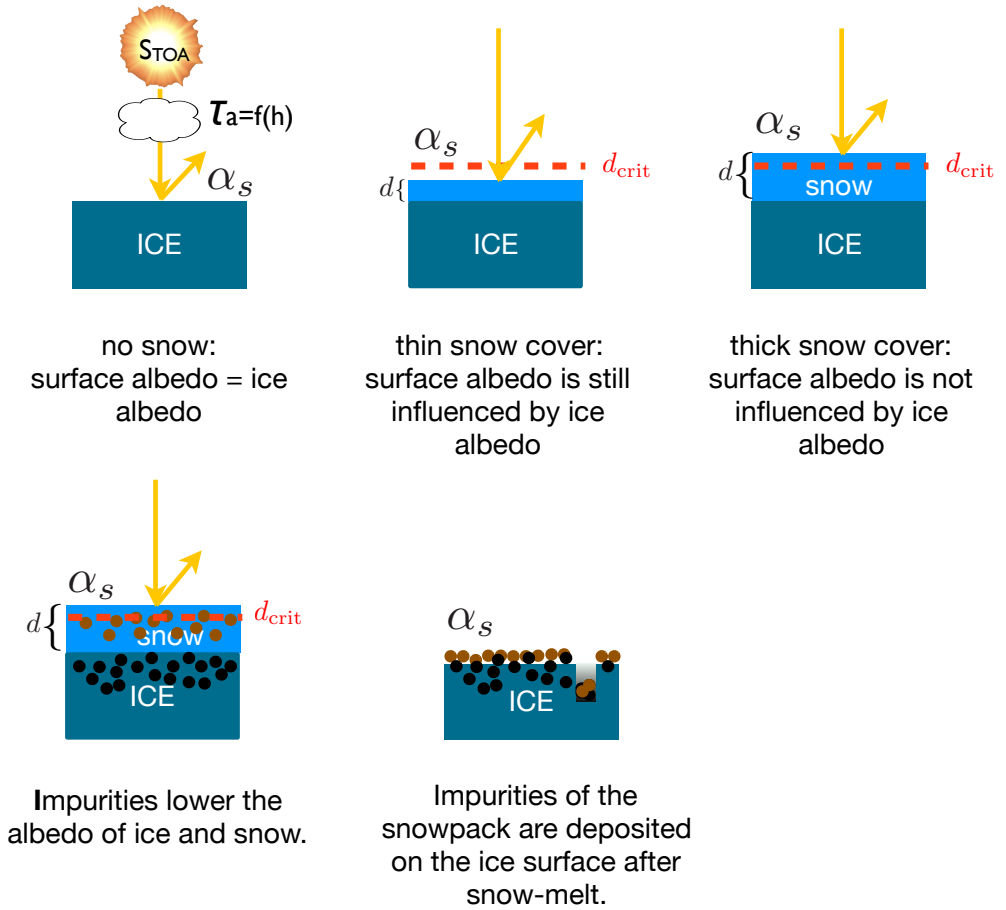
$$\tau_a = 0.56 + 0.00012\,h \qquad (2.20)$$

Figure 2.4: The relationship between ice albedo, snow albedo and impurity concentration to surface albedo (α_s). The surface albedo is still influenced by the underlaying ice surface if the snow depth (d) is lower than the critical snow depth (d_crit).

This equation was derived by comparison of the model net shortwave term $(\tau_a(1 - \alpha_s)S_{TOA})$ to radiation data (see Figure S3 in the supplements). The resulting transmissivity is higher than the one used by Robinson et al. (2010), which was based on ERA-40. While Eqn. 2.20 is based on data of the K-transect weather stations between 2005 and 2012.

2.2.9 Surface mass balance

The change of ice thickness h_{ice} in m w.e. together with the snow depth forms the SMB component of the model. The equation accounting for refreezing reads (Robinson et al., 2010):

$$\frac{\text{d}}{\text{d}t}h_{ice} = \begin{cases} M_s r_f & d > 0 \\ \min(P_{solid} - M_s, 0) & d = 0 \end{cases} \tag{2.21}$$

where r_f is the refreezing fraction within a snowpack as a function of the snow depth and the surface temperature T (Robinson et al., 2010):

$$r_f = \begin{cases} 0 & d = 0 \\ r_{max}f(T) & 0 < d \leq 1 \\ r_{max} + [(1 - r_{max})(d - 1)] & 1 < d \leq 2 \\ 1 & d > 2 \end{cases} \tag{2.22}$$

When the snow depth is below one meter the refreezing fraction is determined by the maximum fraction of refreezing r_{max} and the fraction of snow of total precipitation (Eqn. 2.4). Above one meter, but below two meters, the refreezing fraction increases linearly and reaches its maximum at two meters. The thickness of superimposed ice $h_{s.ice}$ is derived form the first part of Equation 2.21.

2.2.10 Calibration and evaluation

The response of the model to parameters is complex because, for example, a change of the melt component indirectly also alters the surface albedo due to feedbacks to impurity accumulation and the surface type. Due to these feedbacks we use a Monte Carlo approach to calibrate the model. As the criteria of the performance of the model we want to minimise the sum of the deviation between

simulated albedo and observed albedo, during the period of April 1 to September 30:

$$\sum_{01.04}^{30.09} |\alpha_s - \alpha_{AWS}| \tag{2.23}$$

where α_s is the simulated surface albedo (Eqn. 2.18) and α_{AWS} is the albedo derived from radiation data of the automatic weather stations. Reference surface albedo is calculated from daily mean data from the GEUS stations and hourly data for IMAU stations, where only data with a solar zenith angle below 75° is used. The calibration covers one full ablation season after a spin-up. The spin-up starts with zero impurities and no snow and lasts for 100 years. This long spin-up time allows the system to reach equilibrium with all possible parameter combinations.

We chose the free parameters based on available data. The free parameters are: the critical snow depth d_{crit}, the active fraction of BC and dust on ice $\mathcal{F}$, the reduction fraction on ice r_{ice}, the specific surface area of ice $\hat{S}$ and the albedo of clean wet snow $\alpha_{\hat{S},ws}$ without the effect of clouds, and the solar zenith angle.

The range of parameters is shown in Figure 2.5. The critical snow depth determines the rate of change from the summer to the winter surface albedo as well as the change from wet snow to bare ice. It cannot be measured and is therefore a free parameter. The active fraction bundles all surface processes together and is a free parameter which accounts for impurity dynamics on the ice surface and cryoconite hole formation. The runoff fraction on ice is also a free parameter, as it is currently not observed and the range of the runoff fraction is derived from observed impurity masses on the GrIS ablation zone. The specific surface area of ice needs to be calibrated because data is sparse and the parameter range is based on Dadic et al. (2013). The albedo of wet snow accounts for grain growth and is not directly measured, and therefore also calibrated. One set of standard parameters will be chosen and applied to different locations and mass balance years.

2.2.11 Forcing data

Station KAN_M (1270 m a.s.l.) and S5 (460 m a.s.l.) are chosen as the test sites. S5 is situated in the lower ablation zone with high melt rates and little accumulation, and KAN_M is located in the dark area. A simulation of the impurity accumulation, the surface albedo and the SMB requires – besides the common parameters

listed in Table 2.1 and the free parameters – the following inputs: temperature and precipitation, the atmospheric input rates (k_I, k_{II}), and the concentrations of dust and BC in ice.

The temperature parameters $T_\oplus$ and ς are either based on yearly data or the mean values of the whole period (2005-2012). Since the precipitation is not recorded by the AWS we used output of a regional climate model (MAR; Tedesco et al. (2014)) to derive $\overline{P}$.

The atmospheric input rate from distant sources (k_I) of BC is 0.001 g m^{-2} a^{-1} obtained from ice cores (Lee et al., 2013). For dust the atmospheric deposition is 0.01 g m^{-2} a^{-1}, based on model simulation (Mahowald et al., 2011) and ice core analysis (Albani et al., 2015). The local atmospheric input (k_{II}) for both dust and BC is set to zero, since we do not distinguish between those two sources at the moment.

The englacial concentration ($[\iota_{englacial,n}]$) of dust and BC can be provided by a tracer transport module (Goelles et al., 2015), but in this study we will use data from ice cores (Wientjes et al., 2012). The englacial concentration of BC at KAN_M is 4 ng g^{-1}, based on the core at S8 (7.25 km south-west). At S5 the BC concentration is 1 ng g^{-1}, based on the nearby S1 core.

Dust concentration measurements were not included in the shallow cores above, therefore the dust concentrations are based on the NGRIP core (Ruth, 2007). Since KAN_M is located in the dark area we assume a higher dust concentration of 2000 ng g^{-1} and a lower one of 100 ng g^{-1} at S5.

2.3 Modelling results

2.3.1 Calibration

Figure 2.5 presents an overview of simulated and measured surface albedos with the ranges and values of the free parameters listed in the lower section of the graph (surface height change can be found in the supplementary Figure S5). The measured albedo in the summer of 2009 is about 0.20 higher than in the following years. If the model is calibrated on data of 2009 (orange) the match to observed data in 2010 and later is poor. Similarly, if the model is calibrated with data of 2010, 2011 or 2012 it underestimates the ice albedo in 2009.

The reduction fraction on ice r_{ice} and the wet snow albedo $\alpha_{\hat{S},ws}$ are similar for all four calibrations. In contrast, the active fraction $\mathcal{F}$ and critical snow depth d_{crit} vary over a wider range.
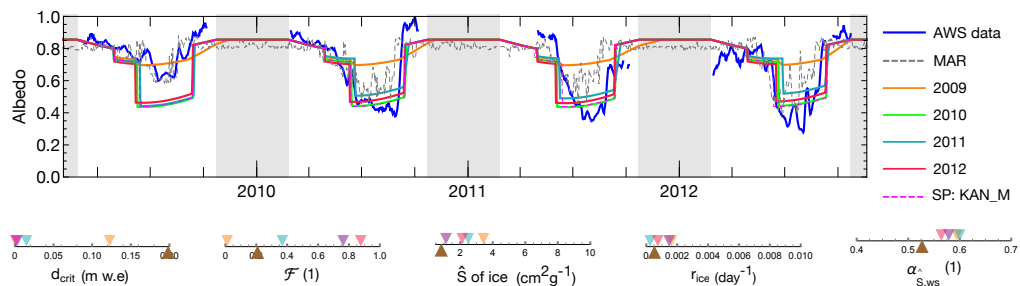
Figure 2.5: Albedo evolution of the KAN_M station from 2009 to 2012. Grey areas indicate periods when the sun zenith angle is higher than 90° (i.e. the sun is below the horizon at mid-day). The albedo data of the AWS (in blue) and of the regional climate model MAR (in dashed black) are shown for comparison and are smoothed with a moving average over a seven-day window. The lower section of the graph presents the free parameter realisations. Each year has its own colour code in the albedo chart and the parameter overview. The dashed magenta line represents a run with the standard parameter set and the mean values of temperature and precipitation of the period (2005-2012). In addition, the parameter set of S5 in 2011 is shown in brown below the scale.

The parameters obtained from 2010 at KAN_M are chosen as the standard parameter set, since the match between model and observation is good over the whole period, except 2009. The model run "SP:KAN_M" uses the standard parameters and the mean temperature parameters $T_{\oplus}$ (1.39 °C with a SD of 0.04) and ς (0.23 °C day $^{-1}$). The resulting albedo of "SP:KAN_M" matches the 2010 simulation closely.

2.3.2 Station KAN_M in 2010

Figure 2.6 displays the simulations of the KAN_M station in the year 2010 in more detail. The amount of dust and BC inside the snowpack (panel c) builds up until all the snow has melted in June (panel e). At the same time, superimposed ice has formed (panel f, and Figure S5) which was assumed to hold no impurities. This causes a drop in dust concentration immediately after the ice is exposed, since the amount of released dust by snow melt is insignificant and the constant runoff kicks in. In contrast, the BC contribution from snow melt causes a sudden increase of the BC amount as ice is exposed, which soon afterwards is reduced due to the same effect.

The lowering of the simulated albedo from March to May is solely due the effect of the zenith angle on albedo. The trend of the albedo is captured well during that period, even without the effects of snow ageing and impurities ($\alpha_{\hat{S},ds}$ is constant).

Similarly, the albedo variation during summer (panel g) is also due to the solar zenith angle. The effect of the small variations of impurities during one summer (panel d) on albedo is too little to be recognised when the system is in equilibrium. However, the total effect of accumulated remains and is about 0.06.

The model realisation "SP:KAN_M" uses the standard free parameters and the temperature and precipitation parameterisation of mean values over the whole period (2005-2012). The resulting albedo (magenta) is almost indistinguishable from the model with the parameterisations of temperature and precipitation derived from the 2010 data (green).

The simulated maximum amount of BC on the ice surface is $0.068\,\mathrm{g\,m^{-2}}$ and of dust is $29.55\,\mathrm{g\,m^{-2}}$. Hence, the mass of dust on the ice surface is 434 times larger than BC. The maximum amount in the snowpack is $0.75\,\mathrm{mg\,m^{-2}}$ BC and $7.45\,\mathrm{mg\,m^{-2}}$ dust.

2.3.3 Stations S5 in 2011

Figure 2.7 displays the simulation of station S5 in 2011 with the parameters shown in Figure 2.5 and the standard parameter set. The duration of the snow cover is more than a month shorter (panel e) when the temperature and precipitation parameterisation is used. This is caused by the overestimated temperature in May (panel a).

The simulated impurity concentrations are lower than at KAN_M due to the lower concentrations of englacial BC and dust. Where the maximum amount of BC on the ice surface is $0.06\,\mathrm{g\,m^{-2}}$ and of dust is $4.04\,\mathrm{g\,m^{-2}}$, which is about 67 times more than BC. Therefore, the albedo lowering at S5 is mostly caused by BC due to the 200 times higher absorption. The maximum amount in the snowpack is also lower than at KAN_M, due to the shorter duration of snow cover (0.638 $\mathrm{mg\,m^{-2}}$ BC and $6.383\,\mathrm{mg\,m^{-2}}$ dust).

The measured SMB at S5 in 2011 was -4.06 meters, while the simulation yielded -2.98 meters. This is mainly due to the overestimated albedo combined with a too-low transmissivity until May, causing a too-low net shortwave radiation (see Figure S6 in the supplements). A graph similar to Figure 2.5 for station S5 can be found in the supplements (Figure S7).
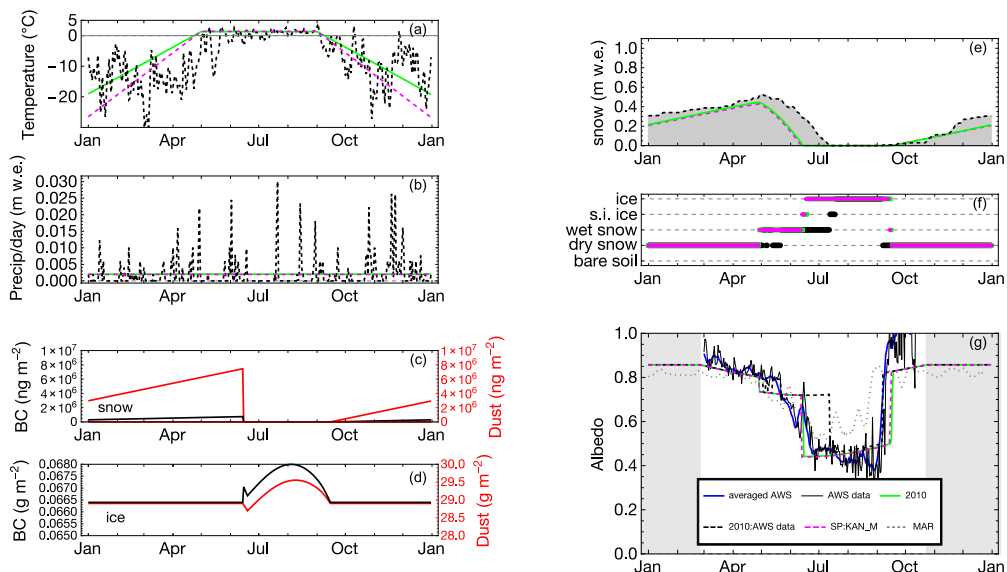
Figure 2.6: Detailed results of station KAN_M in 2010. (a) near-surface temperature parameterisation in green, observation in dashed black and the mean (2005-2012) in magenta. (b) daily precipitation from regional climate model MAR (dashed black), the parameterisation in green, and the mean parameterisation in magenta. (c, d) shows the evolution of dust (red) and BC (black) inside the snowpack and on the ice surface. (e) snow depth evolution with the parameterised temperature and precipitation in green, the "SP:KAN_M" setup in magenta and the setup with temperature from the AWS station and precipitation from the MAR model in black. (f) surface type; s.i. ice stands for superimposed ice. (g) surface albedo evolution of data (blue and thin black) and simulations. The AWS data is shown as a thin black line and the smoothed (over 7 days) data as a thick blue line. The "2010" setup, in green, uses the parameters and the temperature and precipitation parameterisation based on 2010 data. The simulation "2010:AWS data" uses the actual AWS temperature and MAR precipitation, and the "SP:KAN_M" setup uses the standard parameters and the temperature and precipitation means.
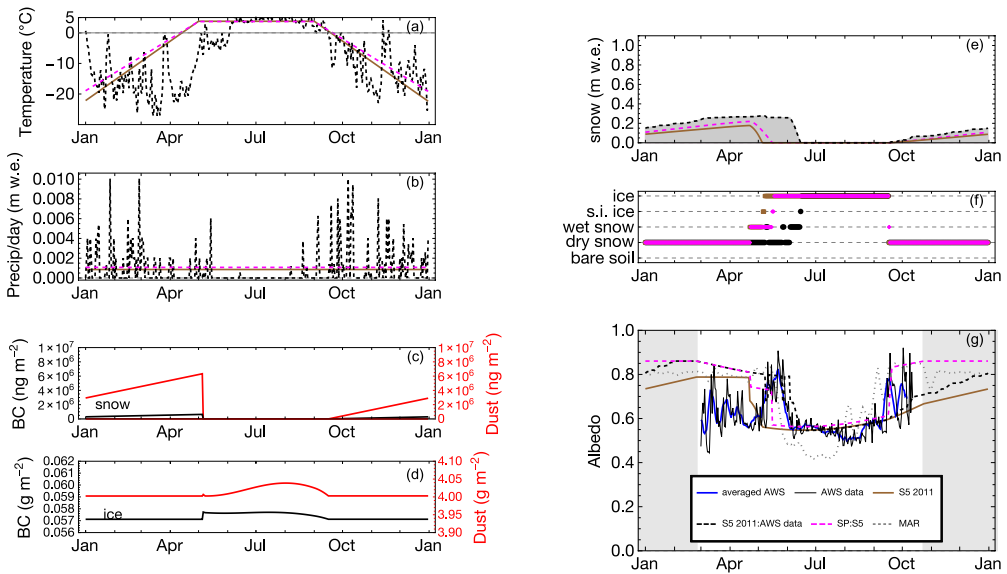
Figure 2.7: Detailed results of station S5 in 2011. The model realisation "SP: S5" (in magenta) uses the standard parameters and the mean values of temperature and precipitation at S5. (a) near-surface temperature parameterisation in brown, based on AWS data of 2011 (dashed black). The magenta line represents the mean values of the period 2005 to 2012 ($T_\oplus$ = 3.70°C with a SD of 0.02 and ς = 0.19 °C day^{-1}) (b) daily precipitation from regional climate model MAR in dashed black, the parameterisation in brown and the mean (2005 - 2012) in magenta ($\overline{P}$ = 1.24 10^{-8} m w.e s^{-1}), (c, d) shows the evolution of dust (red) and BC (black) inside the snowpack and on the ice surface. (e) simulated snow depth evolution based on 2011 data (black), the 2011 parameterisation (brown) and the "SP:S5" configuration (magenta). (f) surface type; s.i. ice stands for superimposed ice. (g) surface albedo evolution of data and simulations. The AWS data is shown as a thin black line and the smoothed (over 7 days) data as a thick blue line. The "2011" setup, in brown, uses the parameters and the temperature and precipitation parameterisation based on 2011 data. The simulation "S5 2011:AWS data" uses the actual AWS temperature and MAR precipitation, and the "SP: S5" setup uses the standard parameters and the temperature and precipitation means.

2.4 Discussion

2.4.1 Assumptions and uncertainties

Due to the design goal, we chose a simplified energy balance, a single-layer snowpack model and a parameterisation of near-surface temperature and precipitation. Therefore, it has to be clear that the model can not compete with full energy balance studies performed in the same area. The goal was that the model takes impurity melt-out and accumulation into account and that it can be used as an alternative to positive degree day models, with only a few required inputs. The simplified energy balance is largely based on Robinson et al. (2010) (sections 2.2.3, 2.2.7, 2.2.8, 2.2.9) where the associated uncertainties have been studied in detail in Fitzgerald et al. (2012). We now briefly discuss the assumptions and uncertainties of each model component, again in the order of the flow chart (Fig. 2.2).

The temperature parameterisation follows the observation reasonably well during the melt period. Also the low standard deviations of $T_\oplus$ at both stations is an indicator of the quality of the temperature parameterisation. At station S5 the start of the positive temperatures was set too early in the presented year and others, causing a too-early melt initiation of the seasonal snow. Further analysis of AWS data is needed in order to derive a parameterisation of the start and end dates of positive temperatures which is valid for the whole GrIS.

The precipitation parameterisation via the annual mean yields a similar snow-depth evolution as when the daily precipitation data from the MAR model is used. Our parameterisation neglects summer snowfall and makes it impossible to account for snow grain growth, which has a big influence on the albedo of snow. Nevertheless, for its simplicity, the precipitation parameterisation performs sufficiently well.

The next component to discuss is the impurity accumulation inside the snowpack and on the ice surface. The impurity accumulation inside the snowpack depends solely on the atmospheric inputs and biological production. Since the atmospheric fallout rates of both BC and dust are low, the impact on the albedo of snow is also low (see also Fig. S2). The constant influx of dust and BC is a simplification – in nature the influx of impurities is very erratic – as can be seen in ice core records (Ruth, 2007; McConnell et al., 2007). Therefore, the impurity concentration inside the snowpack also follows this erratic behaviour in nature. A time-dependent influx of dust and BC could be obtained from atmospheric models in the future

which would allow a more detailed study of the accumulation zone. Along with a multilayer snowpack model and a more sophisticated snow albedo model which takes ageing and impurities into account (e.g. Gabbi et al., 2015).

In addition to the atmospheric inputs, the impurity accumulation on the ice surface depends on ice melt and the englacial concentration via the source k_{III} and the reduction term. The englacial values of BC were obtained from nearby located shallow ice cores. Englacial values of impurities can differ substantially over a short distance due the erratic nature of impurity deposition. Short ice cores located at the AWS sites as well as measurements of surface impurities would be needed to further study the effect of the impurity melt-out. In addition, time-lapse cameras on the weather masts and frequent measurements of surface concentrations could be used to derive the reduction term.

Model snow albedo was unaffected by impurities and only indirectly affected by grain growth. The effect of impurities in snow at the ablation zone is short and low (see also Fig. S2), but the grain growth could cause a difference in surface albedo of more than 0.20. In general, the fixed dry snow albedo matches the observations well until the onset of melt. During snow melt the match becomes weaker due to the neglected grain growth. A time-dependent parameterisation which gradually lowers the albedo of snow after the onset of melt might improve the albedo match in spring. Although the period of snow cover can be long, the effects of the snow albedo on melt in the ablation zone is limited due to the low incoming radiation when the seasonal snow cover is still intact. Nevertheless, in the accumulation zone the snow albedo has a big impact on the overall SMB of the GrIS due to the huge area.

The biggest uncertainties connected to the ice albedo are the active fraction and the parameterisation of the albedo reduction due to impurities. The parameterisation of ice albedo (Eqn. 2.10) assumes external mixture of carbon particles (located outside of ice grains, Gardner and Sharp (2010)). We assumed that particles located on the ice surface have a similar effect on albedo as this external mixture. This might be an oversimplification, which most likely will not hold at very high concentrations when the radiation is fully absorbed by particles on the surface. Although, the isolating effect of dust starts at a thickness of 1.33 mm (Adhikary et al., 2000), which corresponds to surface concentrations in order of kg per square meter. While at both stations the total impurity loading was in the order of a few gram per square meter. Nevertheless, a study of impurities located *on* the ice surface is required in order to further test this assumption or replace the parameterisation by one which takes surface concentrations into account.

The active fraction varied over almost the entire range (Fig. 2.5). This is partly due to model ambiguity: different parameter combinations can lead to the same result, which is a common problem of models with several parameters. For example the combination of a high specific surface area with a high active fraction could lead to the same result as the combination of a low specific surface area with a low active fraction. Therefore, better constrains on the specific surface area are required in order to lower the uncertainty of the active fraction. Similarly, a high impurity concentration and a low active fraction can have the same effect as a low concentration and a high active fraction. Therefore, direct measurements of the englacial concentration and observations of dust and BC deposition can further constrain the active fraction. The active fraction itself could possibly be obtained by time-lapse cameras and further studies on the dynamics of cryoconite holes.

The lower albedos at KAN_M after 2009 could have been caused by an increase in the active fraction – for example, by the releases of impurities from cryoconite holes. Since the dynamics of the active fraction, i.e. the surface processes, are not captured at the moment, no model setup is able to capture 2009 and 2010. For now, the active fraction bundles all surface processes together, but it could be a model component on its own in the future.

Both the albedo of snow and ice are altered by clouds. We developed a linear parameterisation of clouds by elevation. Since this linear parameterisation gives a constant albedo alteration due to clouds, the albedo can be overestimated by up to 0.10 on days with a clear sky and clean ice. The error is smaller with higher impurity loadings and on monthly average the error is in the order of 0.02 (see Figure S1a).

The zenith angle of the sun has a high impact on the albedo of ice due to its low specific surface area. Since the angle of the sun is easy to derive accurately the associated uncertainties are low and solely determined by the parameterisation. Also, the slope of the GrIS is small and therefore plays no role in the effective zenith angle, while this is not be the case for steep valley glaciers.

The free parameter of the surface albedo component (Eqn. 2.18) is the critical snow depth which ranges from 0.01 to 0.20 m w.e.. The change of the observed albedo in the autumn of the years 2010, 2011 and 2012 at KAN_M is abrupt after the first snowfall, which is reflected in a low critical snow depth at those years. The highest critical snow depth was calibrated at S5, where ice might be exposed the whole time due to low accumulation rate and wind drift. Therefore, S5 is not suited to calibrate the critical snow-depth. Hence, the critical snow depth is in the region of 0.02 m w.e..

The potential melt rate influences the surface albedo indirectly via feedbacks to impurity melt-out and via the snow depth. Most significantly it determines the SMB which could be used as a boundary condition for glacier and ice sheet models as well as regional climate models. Potential melt was calculated with a simplified energy balance which depends on, the surface albedo, the insolation on top of the atmosphere and the transmissivity. The transmissivity parameterisation used in previous studies (Robinson et al., 2010, 2011) was found to produce too low values. In this study we derived a transmissivity parameterisation by comparison of modelled and observed net shortwave radiation. Therefore, the overall effect of transmissivity is captured well (see Figure S4 in the supplements). Nevertheless, similar to the effect of clouds on albedo, the melt rate is underestimated on clear sky days because the transmissivity was assumed to be constant.

The standard set of parameters was taken from the model calibration of 2010 at KAN_M. With these parameters the model performed well at both locations and at different years, demonstrating the site and time independence.

Overall, the performance of the model is satisfying, especially of the net radiation (see Fig. S4 and S6), even though the parameterisation of temperature and precipitation is very simple. The design goal in this study was that the model works in a stand-alone application, which required a parameterisation of temperature and precipitation. Although, the model framework is not limited to stand-alone applications. Temperature and precipitation could be provided by an atmospheric model which would allow a more detailed treatment of the snowpack and snow-albedo, including snow grain growth, summer-snowfall and clouds.

2.4.2 Melt-out and runoff of impurities

Dust is the main contributor to impurity mass at both stations, which was also found in observations at different places of the GrIS (Bøggild et al., 2010; Takeuchi et al., 2014). The question is which is the main source of dust and BC on ice: melt-out or the atmospheric sources? The accumulated impurity mass at KAN_M is about ten times larger than at S5. This indicates that melt-out is the main contributor to impurity mass, since the atmospheric input rates are the same for both stations and the impurity runoff is similar (r_{ice}, see Figure 2.5).

One meter of ice melt releases englacial impurities, which have been deposited over years or decades in the accumulation zone several thousand years ago. Dust concentrations in ice formed during the last glacial are 10-100 times higher than in ice formed during the Holocene (Steffensen, 1997). Therefore, currently dust melt-out dominates over atmospheric deposition. For example, one meter melt

of ice with a dust concentration of $1{,}000$ ng g^{-1} releases 0.91 g m^{-2} of dust. At the current rate of atmospheric deposition from large-scale transport it would take about 100 years to deposit the same amount of dust (see also Figure S8).

Atmospheric deposition of dust could play a significant role close to the margin if the transport by wind from the surrounding tundra is effective. The local dust source is likely restricted to the outermost ablation zone because of the prevailing katabatic winds. Therefore, there might be a "threshold elevation" up to which local dust from the tundra contributes significantly. Above this threshold, large-scale transport from distant sources dominates.

For BC the answer is less clear. Ice formed during 1851 to 1951 has a mean concentration of BC of 4 ng g^{-1}, while the pre-industrial concentration is 1.7 ng g^{-1} (McConnell et al., 2007). Atmospheric deposition is the dominant source of BC, up to annual melt rates of one meter and a BC concentrations of 1.0 ng g^{-1} (see Figure S8). At higher melt rates melt-out dominates, but the atmospheric deposition still contributes significantly to the amount of BC on the ice surface.

The reduction fraction r_{ice} of 0.001 per day causes a residence time of the impurities on the ice surface of several decades. This is linked to the slow movement of cryoconite on an exposed ice surface, as has been observed on Longyearbreen, Svalbard (Irvine-Fynn et al., 2011a). It takes more than 56 years in order to reduce from 30 g m^{-2} to below one g m^{-2} by assuming 60 days with exposed ice and exponential decay with one permille per day. Therefore, the impurities enhance ice melt over decades after deposition.

2.5 Conclusions

We developed a surface mass balance model which includes the effect of accumulation of dust and black carbon on the albedo of ice, besides the effects of clouds and the zenith angle of the sun. The model requires only a small number of inputs and is therefore suitable as the surface mass balance component of stand-alone ice sheet or glacier models.

The inferred runoff of impurities is in the order of one permille per day, which corresponds to a residence time of decades on the ice surface during which the albedo is lowered and melt is enhanced. Dust is the main contributor to impurity mass, of which melt-out is the main source. Melt-out of BC is the dominant source at annual melt rates above one meter. Current atmospheric deposition of BC contributes considerably to the total amount of BC on the ice surface. Therefore,

mitigation of BC emissions has an immediate effect on the albedo of the ice surface.

The system has a positive feedback between impurity melt-out and ice melt due to the decadal residence time and the dominant source of melt-out. A high melt event releases large amounts of englacial impurities from within the ice, which lowers the albedo and in turn enhances melt which further releases impurities.

The presented model can be used to study the long-term effect of dust and BC on the future melt of the GrIS and smaller glaciers. Goelles et al. (2015) applied the model to a simplified geometry mimicking the GrIS. They found that, without considering all feedback processes, an additional mass loss of up to 7 % in the year 3000 can be expected if impurity melt-out and accumulation is considered.
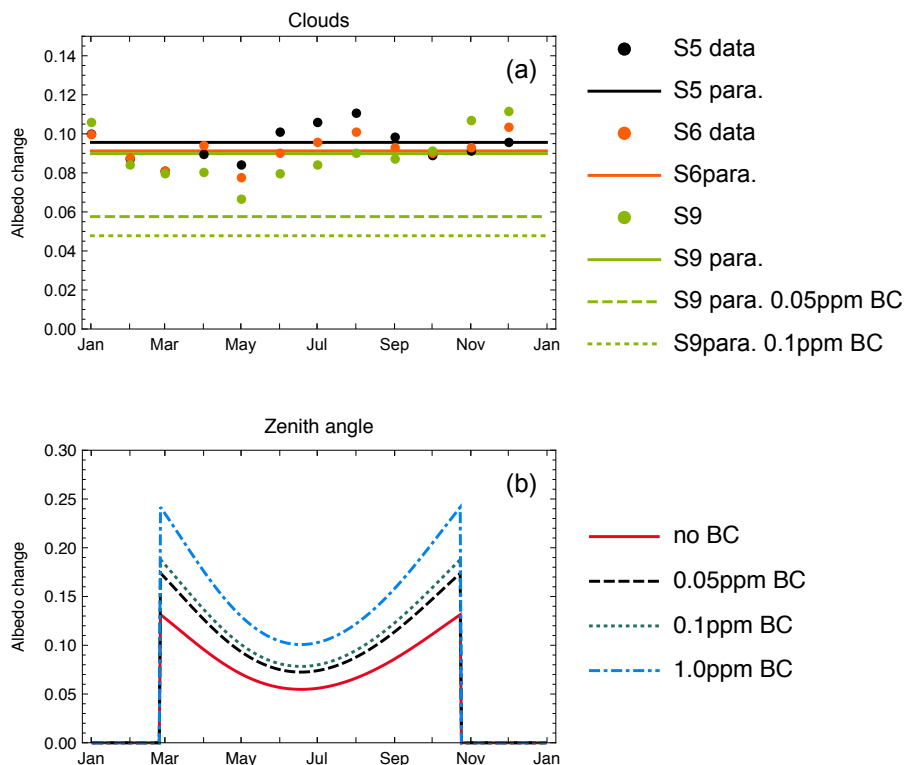
Acknowledgements

2.6 Supplement

Figure 2.8: Albedo effect of clouds **(a)** and the zenith angle of the sun **(b)** at the K-transect. Calculated by Equations 14 and 16, based on a specific surface area of ice of 2 cm^2g^{-1}. The dots in panel **(a)** represent the mean of measurements by Van den Broeke et al. (2008) for the Stations S5, S6 and S9 during 2003-2007. The cloud effect depends on the cloud optical thickness with is parameterized by a function of elevation (full lines). The cloud effect is lower on dirty ice (dashed lines). The effect of the zenith angle of the sun **(b)** is zero when the sun is below the horizon and highest in spring and autumn when the zenith angles are high. The overall negative effect of high BC remains it is only weakened by the low-standing sun. For example, the darkening effect of BC ($d\alpha_c$) with 1 ppm BC is -0.40 which is reduced by the zenith angle to -0.15 in early spring and about -0.30 in mid summer.
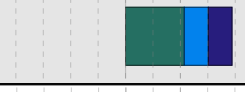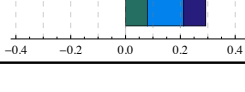
Process	Potential albedo change	Sub–process	Values	Reference
Snow impurities		BC dust	−0.04 −0.019	with 20 cm^2g^{-1} and 0.02 ppm BC with 20 cm^2g^{-1} and 1. ppm dust
Snow other		SSA: ageing zenith angle clouds	0.214 0.088 0.086	difference between 1600 and 20 cm^2g^{-1} with 200 cm^2g^{-1} and 89.9° and no impurities with 200 cm^2g^{-1} no BC, at S5 elevation and τ=12
Ice impurities		BC dust	−0.203 −0.146	with 2 cm^2g^{-1} and 0.1 ppm BC with 2 cm^2g^{-1} and 9. ppm dust
Ice other		SSA: cracks ... zenith angle clouds	0.08 0.132 0.08	difference between 7 and 2. cm^2g^{-1} with 2 cm^2g^{-1} and 89.9° and no impurities with 2 cm^2g^{-1}, no BC, at S5 elevation and τ=12

Figure 2.9: Ranges of albedo changes at the ablation zone of Greenland derived from the parameterization of Gardner and Sharp (2010). The ranges of albedo lowering due to dust and BC in snow are low, even with high impurity loadings and very dense snow. Snow aging has the potentially biggest influence on albedo of snow. Impurities on ice have a range of about 0.35 in total, due to the low specific surface area of ice and the high impurity concentrations caused by accumulation over several years and melt-out from highly contaminated ice. In addition the zenith angle has a high, positive effect on the albedo of ice.
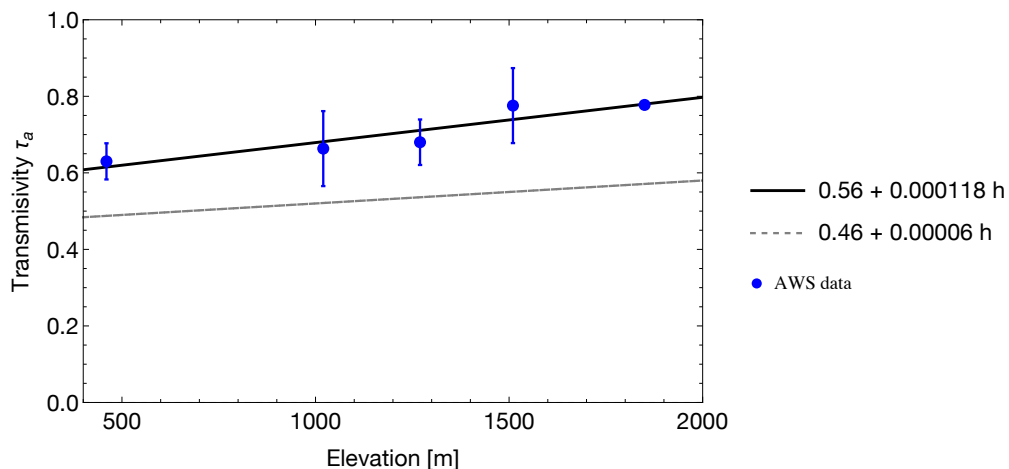
Figure 2.10: Transmissivity versus elevation with the linear fit of Robinson et al. (2010) (dashed line) and a linear fit obtained by comparing the modeled net shortwave radiation with observations for the years 2005-2012. The blue dots are calculated transmissivity values for each station with standard deviations. These values were obtained be minimizing the difference of observed net shortwave radiation and the modeled one $(\tau_a(1-\alpha_s)S_{\text{TOA}})$ with the observed albedo, see also Figure 2.11 below.
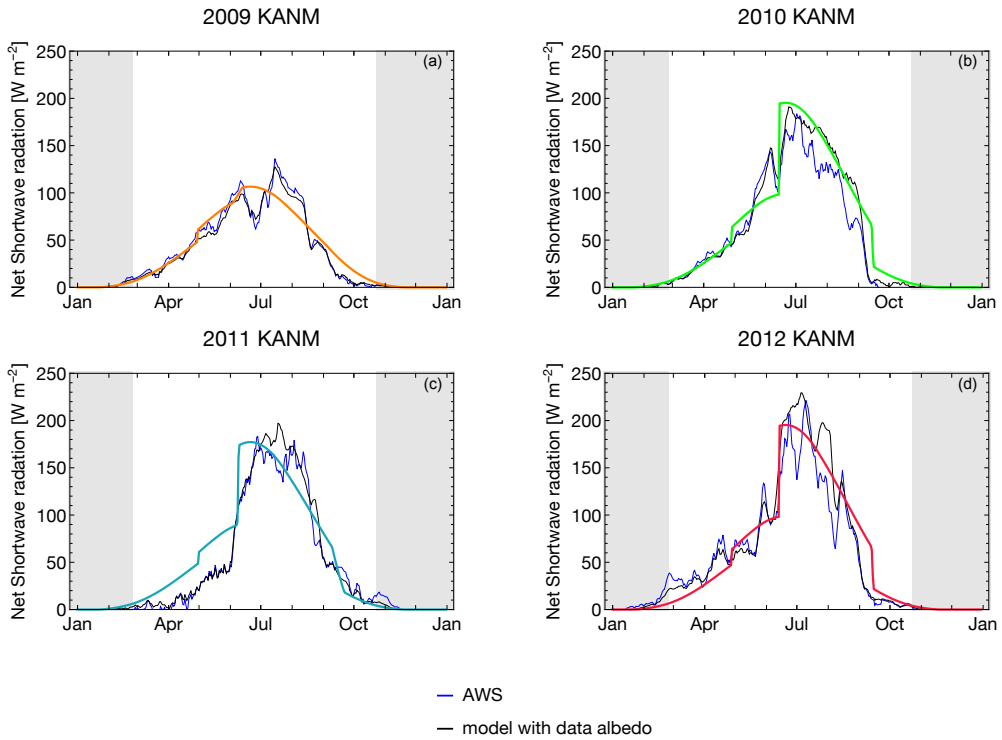
Figure 2.11: Comparison of net short wave radiation of the station KAN_M of the years 2009-2012. The grey areas indicate periods when the sun is below the horizon. The black line is the modeled net shortwave radiation $\tau_a(1-\alpha_s)S_{\text{TOA}}$ with the albedo derived from AWS measurements. The similarity between the AWS net shortwave radiation (in blue) and the black line is an indicator of the quality of the transmissivity τ_a (see Figure 2.10 above). The green line is the modeled net shortwave radiation with the free parameters calibrated to each year (see Figure 2.11 in the main text).
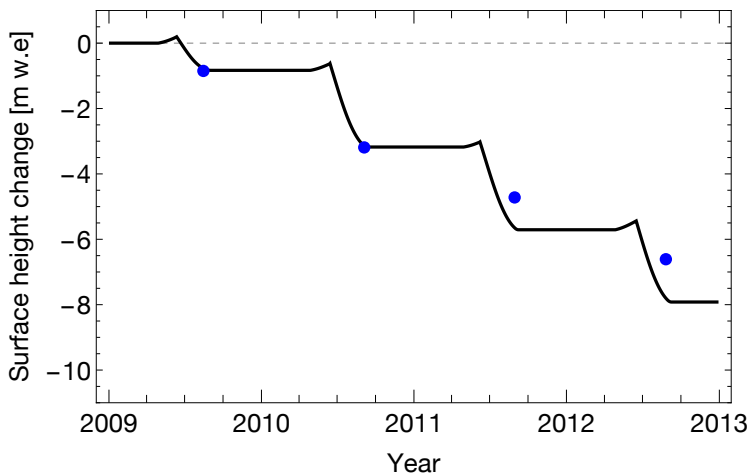
Figure 2.12: Surface height change of KAN_M with the calibrated model runs compared to data in blue from Machguth et al, submitted. The increase in surface height during spring each year is caused by superimposed ice formation.
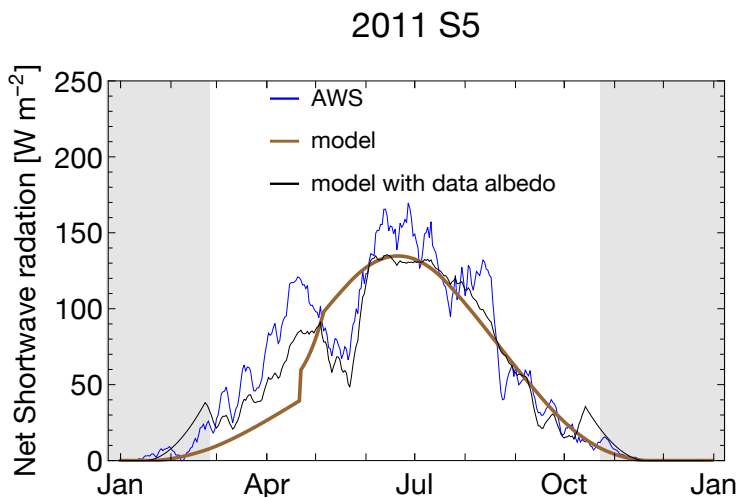
Figure 2.13: Same as Figure 2.11, but for station S5.
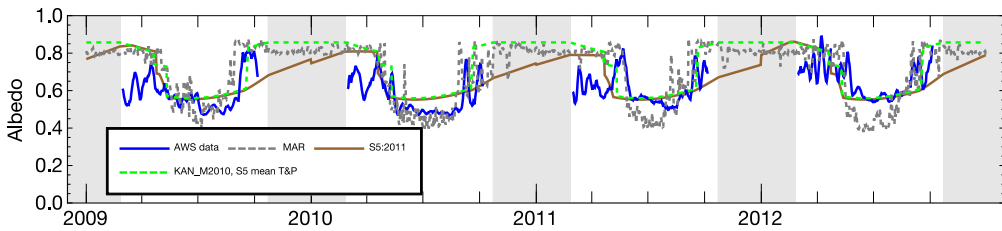
Figure 2.14: Albedo data and simulation for station S5 with parameters optimized for 2011 (in brown) and the mean model configuration of KAN_M in 2010 (green) with the mean temperature and precipitation of S5 ($\overline{P}$ (1.24 10^{-8} m w.e s^{-1}) , $T_{\oplus}$ (3.70°C) and ς (0.19 °C day^{-1}). The albedo data of the AWS (in blue) and of the regional climate model MAR (in dashed black) are shown for comparison and are smoothed with a moving average over a seven-day window. Grey areas indicate periods when the sun zenith angle is higher than 90°(i.e. the sun is below the horizon at mid-day).
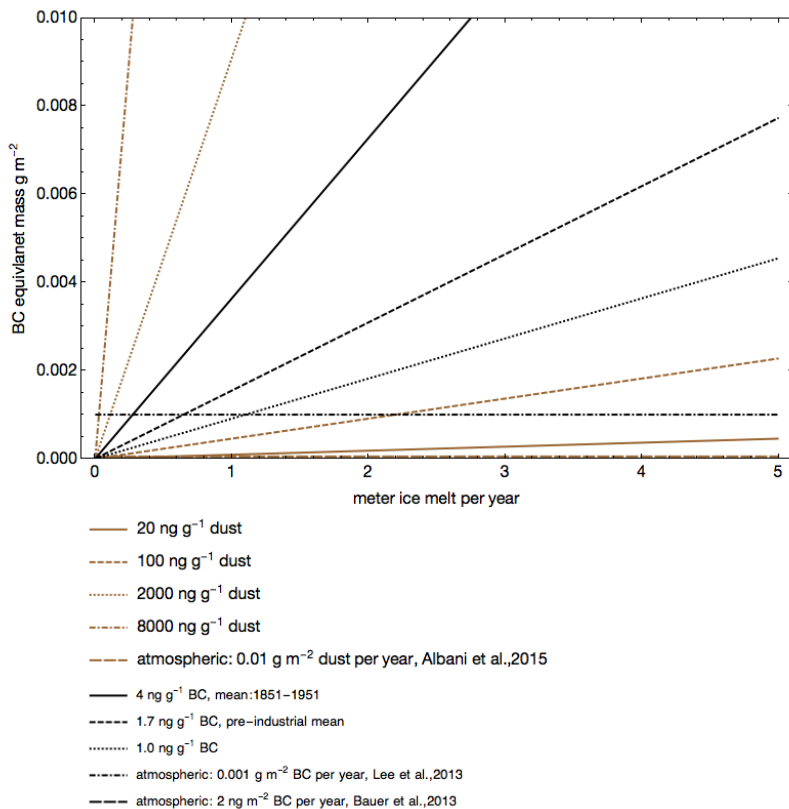
Figure 2.15: Comparison of annual melt-out and atmospheric deposition of BC (black) and dust (brown). The values of dust are converted in BC by assuming a 200 times weaker absorption. The atmospheric rate of deposition of dust is too low to be visible, therefore melt-out of dust is always the dominant source. The atmospheric deposition of BC is the dominant source when the englacial concentration is 1.0 $ng\,g^{-1}$ and the annual melt below one meters. Otherwise, BC deposition is dominated by melt-out but atmospheric deposition still plays a significant role. This graph can also be used to guess which impurity is mostly responsible for lowering the ice albedo. If the concentrations of BC and dust are known then the steepest line belongs to the main contributor. For example, at S5 the BC concentration is 1.0 $ng\,g^{-1}$ and the dust concentration 100 $ng\,g^{-1}$. The line of the BC concentration is steeper and therefore S5 is dominated by BC, which was also the result from the detailed simulation.

Chapter 3

Article II

Goelles, T., Bøggild, C. E. and Greve, R.

Ice sheet mass loss caused by dust and black carbon accumulation

Abstract

Albedo is the dominant factor governing surface melt variability in the ablation area of ice sheets and glaciers. Aerosols such as mineral dust and black carbon (soot) accumulate on the ice surface and cause a darker surface and therefore a lower albedo. The darkening effect on the ice surface is currently not included in sea level projections, and the effect is unknown. We present a model framework which includes ice dynamics, aerosol transport, aerosol accumulation and the darkening effect on ice albedo and its consequences for surface melt. The model is applied to a simplified geometry resembling the conditions of the Greenland ice sheet, and it is forced by several temperature scenarios to quantify the darkening effect of aerosols on future mass loss. The effect of aerosols depends non-linearly on the temperature rise due to the feedback between aerosol accumulation and surface melt. According to our conceptual model, accounting for black carbon and dust in future projections of ice sheet changes until the year 3000 could induce an

additional volume loss of 7 %. Since we have ignored some feedback processes, the impact might be even larger.

3.1 Introduction

The Greenland ice sheet contributes to sea level rise through dynamic processes and surface mass balance (SMB). After the year 2009, about 84 % mass loss of the Greenland ice sheet was due to a reduced SMB (Enderlin et al., 2014). The SMB is the net balance between snow accumulation and ablation consisting of melt and sublimation of snow and ice. Therefore calculations of SMB depend on the accuracy of snowfall and ablation. Ablation is largely controlled by near-surface temperature and absorbed short-wave radiation. Surface albedo and the amount of incident radiation controls the portion of absorbed short-wave radiation (e.g. van Angelen et al., 2012; Bougamont et al., 2005; Tedesco et al., 2011).

In the Fifth Assessment Report (AR5; Stocker et al., 2013), ablation was computed by energy balance models (EBMs) and with the positive-degree-day (PDD) method, which does not explicitly include surface albedo. Regional climate models with energy balance models produced a 14–31 % higher sea level rise contribution from the Greenland ice sheet than models using PDD (Goelzer et al., 2013) because PDD can not account for the positive feedback of albedo to near-surface temperature. Surface albedo implementations vary through the different EBMs considered in the AR5. The surface albedo is primarily determined by whether the surface consists of snow or ice and by the optical properties of the surface. All the EBMs in the AR5 used for sea level rise predictions have rather sophisticated snow albedo schemes, while the ice albedo is often constant in space and time (e.g. Mernild et al., 2010; Rae et al., 2012).

Surface albedo is determined by the optical properties of the surface, the angle of incidence of downward radiation and the ratio of direct to diffuse radiation. The optical properties of ice are mainly determined by the specific surface area of ice (that results from the combined effect of air bubbles, cracks, etc.). In addition, the optical properties are altered by the content of liquid water and impurities (Cuffey and Paterson, 2010). These impurities consist of aerosols such as mineral dust and black carbon (BC) and impurities related to biological activity. Dust makes up most of the impurity mass on ice (Bøggild et al., 2010; Takeuchi et al., 2014), but BC has a higher effect on albedo per mass (Warren and Wiscombe, 1980). The darkening effect and dynamics of biological-related impurities remain to be quantified (Stibal et al., 2012; Yallop et al., 2012).
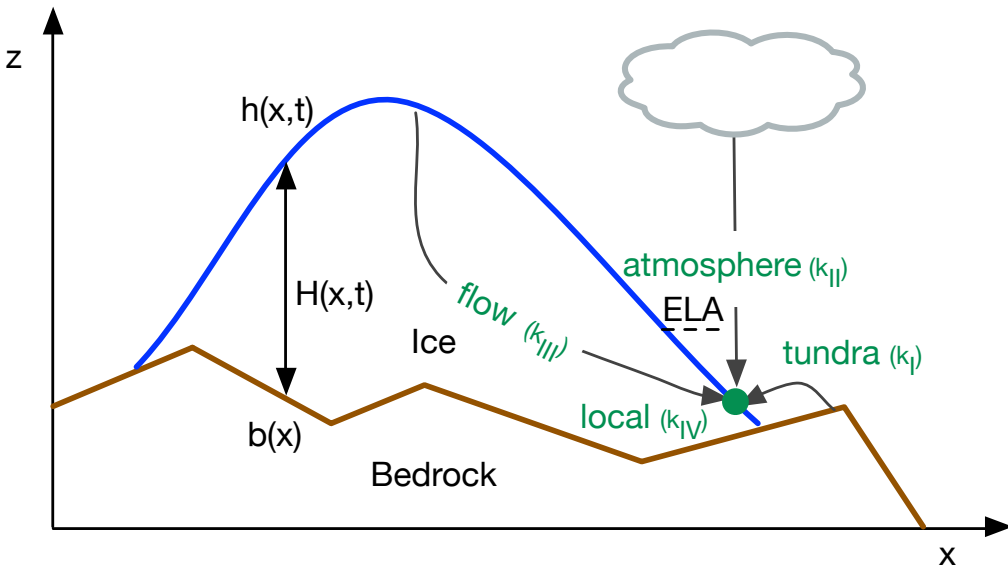
Figure 3.1: Cross section through an ice sheet: the different mechanisms of aerosol transport to the ablation zone. ELA stands for equilibrium line altitude, b is the (fixed) bedrock elevation, h the ice surface elevation and H the ice thickness.

BC is a carbonaceous material which strongly absorbs visible light and is formed primarily in flames (Bond et al., 2013). Ice core data from Greenland revealed higher concentrations in ice dated younger than 1850 (McConnell et al., 2007) due to increased emissions after the industrial revolution. BC concentrations decreased back to almost pre-industrial levels around 1950 due to successful mitigation in North America, which was found to be the source of BC in Greenland during that period. In contrast to that, BC emissions in Asia have been rising since the year 2000 (Lei et al., 2011; Lu et al., 2011).

Asia was found to be the main source of dust during the last glacial (Biscaye et al., 1997). During glacials the dust concentration in ice is 10–100 times higher than during interglacials such as the current Holocene (Steffensen, 1997). Ice from the last glacial is found in the deeper parts of the Greenland ice sheet (MacGregor et al., 2015) and therefore acts as a reservoir for large amounts of dust (Reeh et al., 1991; Bøggild et al., 1996).

Dust and BC are transported with the ice flow towards the ablation zone, where melt releases the particles. Over time the impurities from melt-out and atmospheric deposition accumulate, which enhances melt and therefore causes more particles

to be released. This positive feedback is currently unquantified and not included in the AR5 sea level rise experiments.

In this study, we investigate the impact on ice sheet volume caused by the darkening effect of dust and BC on the ice surface of the Greenland ice sheet. We introduce a new model framework which includes transport, melt-out and accumulation of aerosols and its effect on ice albedo coupled to the SMB and ice dynamics. This model is then applied to a simplified geometry and forced by future climate scenarios until the year 3000.

3.2 Model description

3.2.1 Model framework and set-up

Aerosols reach the ablation zone by four different mechanisms (Fig. 3.1): via direct atmospheric deposition from local sources (k_{I}), by large-scale transport (k_{II}) or by melt-out of englacial particles which have been transported via ice flow (k_{III}). Local production (k_{IV}) is only relevant for microbiological activity and is 0 for dust and BC considered in this study. The atmospheric contribution (k_{II}) and input from the surrounding tundra (k_{I}) are prescribed and constant in the simulations. Melt-out of aerosols (k_{III}) requires, besides the SMB, the near-surface concentration of englacial aerosols ($[\iota_{\mathrm{n,englacial}}]$). This is calculated via a tracer transport module which depends on the aerosol time series, velocities and ice sheet dimensions (Fig. 3.2).

Aerosol accumulation, ice albedo and surface mass balance are presented in detail in Goelles and Bøggild (2015), and therefore their description is kept to a minimum in the following sections. The common quantities and physical constants are listed in Table 3.1. The model is realised in Mathematica (version 10; Wolfram Research, Inc., 2014) using self-coded solvers for the differential equations.

Table 3.1: Standard physical parameters and constants.

Symbol	Short description	Value	Unit
x_{su}	Location of the summit	750	km
$T_{+,\mathrm{su}}$	Temperature in summer at summit	−8	°C

|			
S_T	Horizontal temperature gradient	1.67×10^{-2}	$\mathrm{K\,km^{-1}}$
ρ_{ice}	Density of ice	910	$\mathrm{kg\,m^{-3}}$
ρ_{w}	Density of water	1000	$\mathrm{kg\,m^{-3}}$
$\mathcal{A}$	Seconds per year	31 556 926	–
r_{max}	Refreezing fraction	0.6	–
$t_{\bigcirc,\mathrm{start}}$	Start of summer	121	day of the year
$t_{\bigcirc,\mathrm{end}}$	End of summer	244	day of the year
ς	Temperature slope	0.2	$\mathrm{K\,day^{-1}}$
λ	Long-wave radiation coefficient	10	$\mathrm{W\,m^{-2}\,K^{-1}}$
c	Short-wave radiation and sensible heat flux constant	-55	$\mathrm{W\,m^{-2}}$
L_{m}	Latent heat for melting of ice	334 000	$\mathrm{J\,kg^{-1}}$
d_{eff}	Effective depth of ice	5	m
r_{ice}	Reduction fraction, ice	0.001	$\mathrm{day^{-1}}$
r_{snow}	Reduction fraction, snow	0	–
–	Dust-to-BC conversion factor	$1/200$	–
Δt_{dyn}	Ice dynamics time step for the spin-up	50	years
Δt_{dyn}	Ice dynamics time step for the experiments	1	year
Δt_{SMB}	SMB and accumulation time step	1	day
T_{b}'	Basal temperature relative to pressure melting	-2	$^{\circ}\mathrm{C}$
$\mathcal{F}_{\mathrm{ice}}$	Active fraction for dust and BC on ice	0.5	–
$\alpha_{\mathrm{snow,\ wet}}$	Wet snow albedo	0.6	–
$\alpha_{\mathrm{snow,\ dry}}$	Dry snow albedo	0.8	–
d_{crit}	Critical snow depth	0.05	m w.e.
$k_{\mathrm{II,BC}}$	Atmospheric input of BC	6.34196×10^{-7}	$\mathrm{ng\,s^{-1}}$
$k_{\mathrm{II,dust}}$	Atmospheric input of dust	0.3	$\mathrm{ng\,s^{-1}}$
$\hat{S}$	Specific surface area of ice	2	$\mathrm{cm^2\,g^{-1}}$
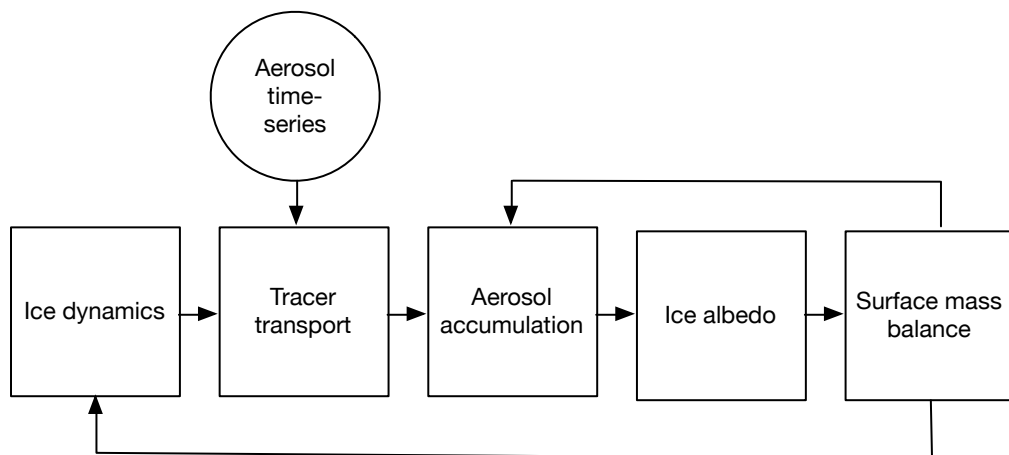
Figure 3.2: Model framework: the ice dynamics component delivers velocity and ice sheet dimensions to the tracer transport module. An aerosol time series in conjunction with the tracer transport conveys englacial aerosol concentrations to the accumulation module. The SMB module delivers snow depth and melt rates to the accumulation module, which calculates dust and BC amounts separately in the snowpack and on the ice surface. These results are then fed into the ice albedo module which is used by the SMB component (based on a simplified energy balance). The SMB is then fed back into the ice dynamics module.

3.2.2 Ice dynamics

We employed the shallow ice approximation in plane strain, that is, only the vertical $x–z$ plane is considered. The corresponding finite difference discretisation is described in detail by Greve and Blatter (2009). The ice thickness equation is solved by an implicit scheme (e.g Greve and Calov, 2002). A terrain-following coordinate transformation is used in order to explicitly compute surface values. These are required for the tracer transport in order to calculate the englacial aerosol concentration close to the surface and ultimately ice albedo values. Basal sliding is implemented with a Weertman-type sliding law including sub-melt sliding (Greve, 2005).

3.2.3 Tracer transport

Dust and BC concentrations are indirectly derived from the time of deposition t_d and the aerosol time series (see next section). Besides the time t_d, also the x coordinate of deposition x_d is calculated via a semi-Lagrangian transport scheme based on Clarke and Marshall (2002). The scheme provides both t_d and x_d as functions of (t, x, z). It has advanced stability compared to Eulerian advection while still using a regular grid. The scheme is common in atmospheric models and has been used before in ice sheet models for δ^{18}O transport (Clarke and Marshall, 2002; Clarke et al., 2005; Lhomme et al., 2005a; Lhomme, 2004; Goelles et al., 2014). Especially the indirect method is suited for discontinuous data such as aerosol concentration while still using a coarse vertical resolution. At each grid point a back trajectory is calculated based on the velocity field from the ice dynamics module. Here we use the first-order backtracking (Clarke and Marshall, 2002; Clarke et al., 2005; Lhomme et al., 2005a; Lhomme, 2004) for simplicity and efficiency, knowing that this method has its limitations close to the margin (Goelles et al., 2014) (see discussion in Sect. 3.5.2).

3.2.4 Aerosol time series

The aerosol concentration $[\iota_\mathrm{n,englacial}]$ of every grid point can be derived from the aerosol time series $f(t_\mathrm{d})$ and the depositional time $t_\mathrm{d}(t, x, z)$ via the relationship

$$[\iota_\mathrm{n,englacial}(t, x, z)] = f(t_\mathrm{d}(t, x, z)). \tag{3.1}$$

Data from ice cores with an established age-depth model are required for the right-hand side of Eq. (3.1). A comparison between the NGRIP and NEEM ice cores (Bigler, 2012) of Greenland showed very similar results in the two cores although they are more then 350 km apart. Therefore, we use only the information of one ice core for the whole ice sheet, and f in Eq. (3.1) has no explicit dependence on x. The aerosol time series in Fig. 3.3 are extended beyond the data range in order to allow simulations until the year 3000.

3.2.5 Aerosol accumulation

The accumulation module handles both bulk BC and dust content of the snowpack and the mass per area on the ice surface. It is described in detail in Goelles and Bøggild (2015). Aerosols accumulate in the snowpack from sources k_I and k_II and
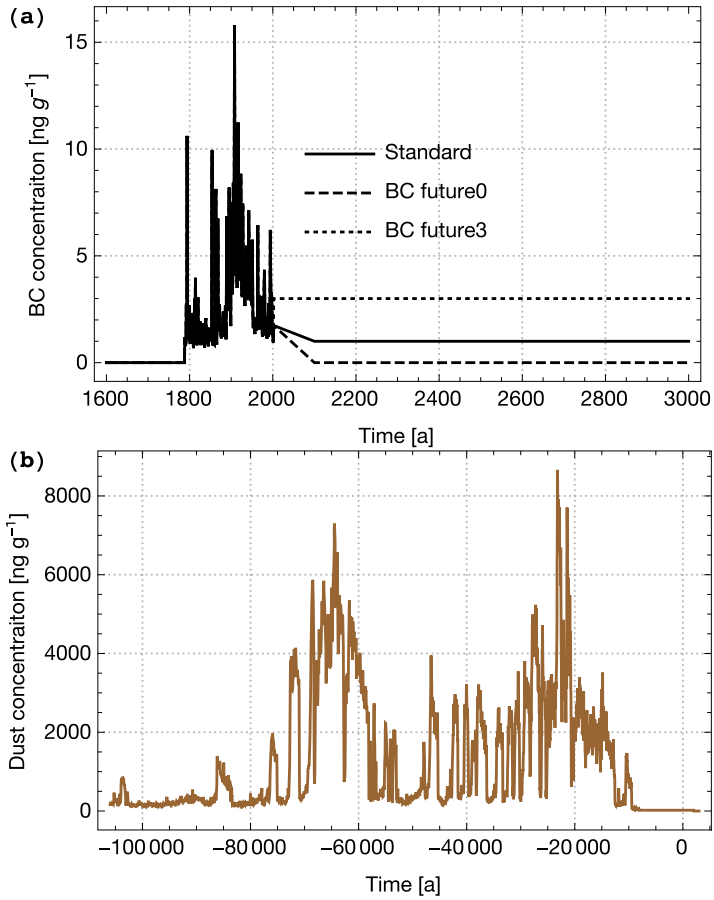
(a)

(b)

Figure 3.3: Aerosol time series of **(a)** black carbon (BC) and **(b)** dust. **(a)** The standard BC time series consists of ice core data by McConnell et al. (2007) and projections based on Bauer et al. (2013) with two additional trajectories of the future. In the period before data are available the BC concentration is set to 0. **(b)** The dust concentration from NGRIP (Ruth, 2007), where the missing Holocene period (after -8 ka) is assigned a constant value of $20\,\mathrm{ng\,g^{-1}}$, and a value of 0 is assumed after the year 2000.

are released onto the ice surface as the snow disappears at the start of the melt season. As ice is exposed, the sources k_I and k_II, in addition to aerosols from melt-out (k_III), directly contribute to the aerosol amount on the ice surface. The accumulation is counteracted by a daily reduction fraction r_ice of the order of 1 per mille per day when ice is exposed. In the snowpack all aerosols are conserved ($r_\mathrm{snow} = 0$).

3.2.6 Ice albedo

Ice albedo is determined via the specific surface area of ice $\hat{S}$ and the reductions caused by dust and BC, as described in Goelles and Bøggild (2015). The dust concentration is converted into an equivalent BC concentration, and the albedo reduction is calculated with the parameterisation $d\alpha_{\iota,1}$ by Gardner and Sharp (2010). A conversion from aerosol mass per area to ppm is required as the parameterisation is formulated in terms of BC concentration. This is done via the effective depth d_{eff} representing the absorption length in ice. Only an active fraction $\mathcal{F}$ of the aerosols influences the ice albedo, while the remainder is concealed in cryoconite holes.

3.2.7 Surface mass balance

The surface mass balance is calculated with a simplified energy-balance model (e.g. Oerlemans, 2001) which is optimised for Greenland (Robinson et al., 2010, 2011; Goelles and Bøggild, 2015). It also includes a simple snowpack model and refreezing. If the snow depth exceeds 5 m, the ice equivalent part is added to the ice thickness $H(x, t)$. The snow depth is also required for the surface albedo to distinguish between ice and snow. The snow albedo is divided into the two values $\alpha_{\text{snow, dry}}$ and $\alpha_{\text{snow, wet}}$. These values are kept constant throughout the experiments in order to separate the ice albedo effect.

3.3 Experimental design and parameters

3.3.1 EISMINT and RCPs

The experiments are based on the set-up of the European Ice Sheet Modelling Initiative (EISMINT Phase 2; Payne et al., 2000) combined with AR5 temperature projections for Representative Concentration Pathways (RCP; Stocker et al., 2013), with standard parameters listed in Table 2.1. These parameters are common for all simulations unless stated otherwise.

The EISMINT boundary conditions are symmetrical around x_{su} and roughly mimic conditions of a west–east cross section of Greenland. The simple, symmetric geometry is ideally suited as a test case for new methods with the additional benefit of ease of interpretation. In Goelles and Bøggild (2015) we introduced an

annual temperature parameterisation with a trapezoidal shape:

$$T = \begin{cases} T_+ & t_{\bigcirc,\text{start}} \le t \le t_{\bigcirc,\text{end}} \\ t\,\varsigma - t_{\bigcirc,\text{start}}\,\varsigma + T_+ & t < t_{\bigcirc,\text{start}} \\ -t\,\varsigma + t_{\bigcirc,\text{end}}\,\varsigma + T_+ & t > t_{\bigcirc,\text{end}}, \end{cases} \tag{3.2}$$

where T_+ is the mean summer temperature between $t_{\bigcirc,\text{start}}$ and $t_{\bigcirc,\text{end}}$. Based on the EISMINT set-up the temperature distribution in x direction is

$$T_+(x) = T_{+,\text{su}} + S_T\sqrt{x - x_{\text{su}}}, \tag{3.3}$$

where $T_{+,\text{su}}$ is the minimum temperature located in at the summit and S_T is the gradient with horizontal distance.

Temperature evolution scenarios are based on long-term projections until 2300 for the global annual mean surface temperature (Fig. 3.4). The RCPs are named after their expected radiative forcing in the year 2100 compared to pre-industrial values. The four scenarios are RCP2.6, which is a mitigation scenario leading to low forcing, two stabilising scenarios (RCP4.5 and RCP6.0) and one scenario with very high concentrations (RCP8.5). The temperature anomalies are added each year to every grid cell.

The precipitation (see Fig. 3.11a in the Supplement) is kept on the same level for all RCP scenarios and corresponds to 0.5 m a^{-1} ice equivalent in the accumulation zone, except for one experiment with an increase of 20 % in precipitation (RCP4.5 + 20 % precip †).

The insolation at the top of the atmosphere (see Fig. 3.11b) is based on the calculations by Liou (2002) for 67° N, in the centre–south of the Greenland ice sheet for which the EISMINT boundary conditions are roughly representative.

3.3.2 Spin-up

A spin-up model run acts as the common starting point for all experiments. The ice sheet after the spin-up is in steady state with the dust and BC concentrations computed over the whole domain. The spin-up starts at -30 ka and ends in the year 2000 with a resolution in x of 25 km and 20 layers in z direction. During the spin-up, the ice albedo is based on a specific surface area of 2 cm^2 g^{-1} of ice of a density of 880 kg m^{-3} and above (Dadic et al., 2013), equivalent to a clean ice albedo of 0.53.
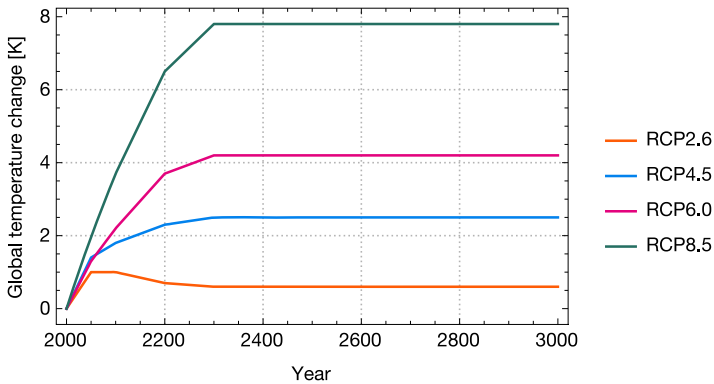
Figure 3.4: Global annual mean surface air temperature anomalies for different representative concentration pathways (Stocker et al., 2013; Table 12.2). After 2300 the temperature anomalies are kept constant.

3.4 Results

3.4.1 Spin-up

It takes about 10 000 years for the spin-up to reach equilibrium (see Fig. 3.12).

The simulated englacial aerosol concentration, depositional x and time are shown in Fig. 3.5. Of those quantities, the depositional time t_d (panel d) is the most important one as the englacial BC and dust concentrations are inferred from it (Eq. 3.1). Ice older than -20 ka can only be found at the very bottom and not close to the surface, which indicates that the spin-up is sufficiently long.

Figure 3.6 shows surface values of the same quantities as in Fig. 3.5. At each time step, the values are joined together, which results in graphs showing the surface evolution of the respective quantities over the whole period. The ice sheet expands in the first few thousand years until a dynamic equilibrium is reached, as can be seen in the widening of the surface values in the upper sections of the graphs.

The high BC concentrations during the period 1850–1950 are indicated in light green in Figs. 3.5d and 3.6d. This period is short compared to the whole spin-up and is visible as a thin light-green stripe close to the surface in the cross section (Fig. 3.5b) and in the bottom part of the time series plot (Fig. 3.6b). Most of the ice was deposited before 1850, and therefore most parts of the ice have a 0 BC concentration.
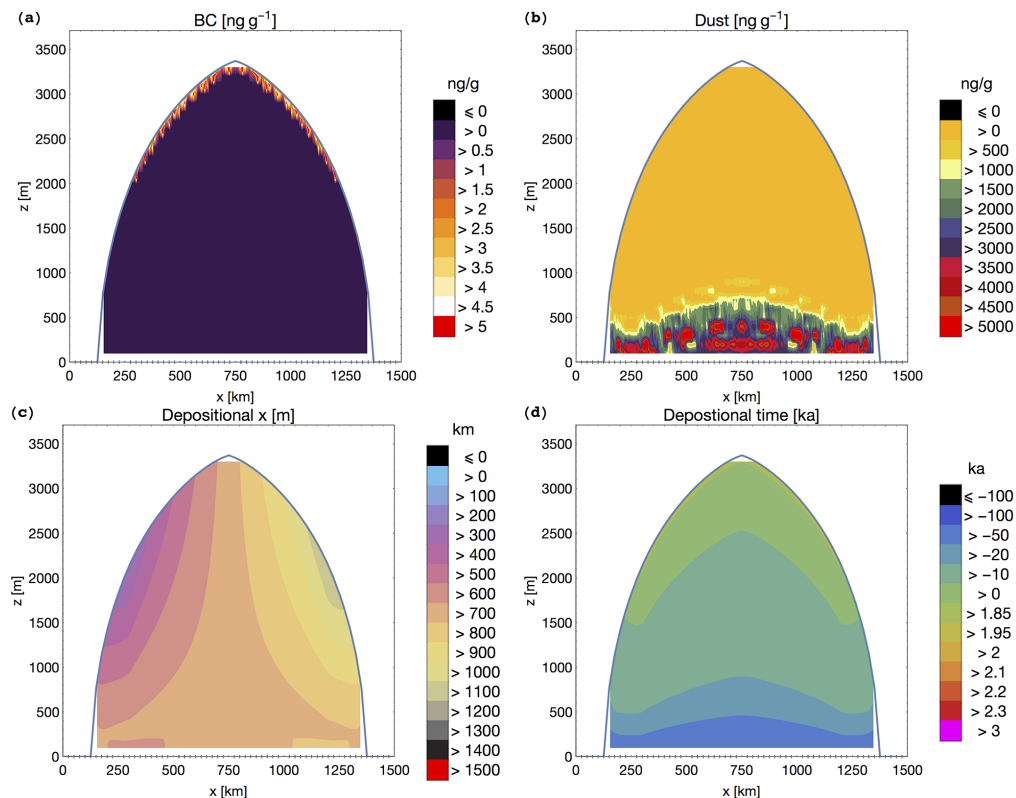
Figure 3.5: Cross section of the spin-up ice sheet in the year 2000: **(a)** englacial black carbon concentration, **(b)** dust concentration, **(c)** depositional x (provenance) and **(d)** depositional time (where 2 ka is the year 2000 AD).

The sequence of peaks in the dust time series can be seen in Fig. 3.6a as a sequence of red stripes, indicating high concentrations. The stripes are first visible in the accumulation area in the centre and later in the ablation zone on the sides. The low Holocene values dominate after -10 ka, and dust concentrations are only high in the outermost grid cells on each site. This is the region where ice from the last glacial reaches the surface (Fig. 3.6d).

3.4.2 Ice sheet volume evolution

Results of the experiments driven by the four RCP scenarios with (dashed lines) and without (solid lines) aerosols from the year 2000 to 3000 are shown in Fig. 3.7. In general, the ice sheet is thinner everywhere in the year 3000 when dust and
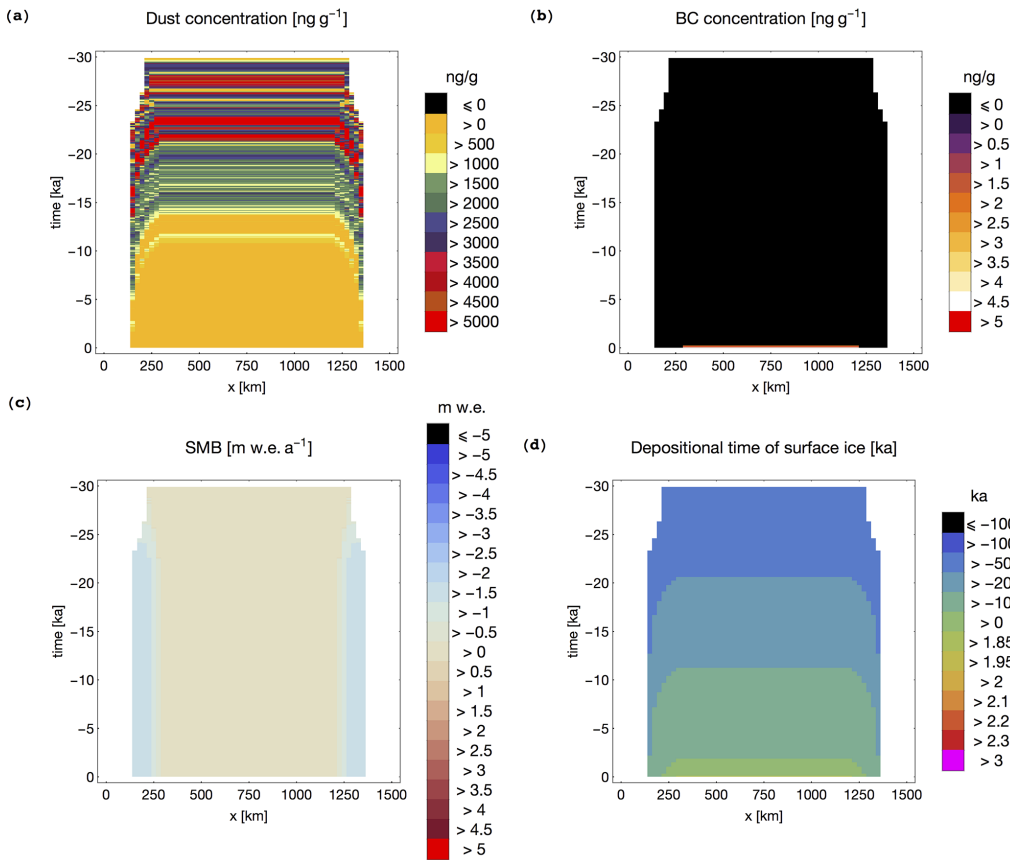
(a) Dust concentration [ng g^{-1}]

(b) BC concentration [ng g^{-1}]

(c) SMB [m w.e. a^{-1}]

(d) Depositional time of surface ice [ka]

Figure 3.6: Time series of the surface values of **(a)** englacial dust, **(b)** englacial BC, **(c)** surface mass balance and **(d)** time of deposition. The vertical axis shows time with the start of simulation at the top.

BC are considered (panel b). The main height differences (panel c) are located at the margin. This is a result of the lower annual SMB (panel d), which in general is lower in the ablation zone when aerosols are considered. Panel e shows the volume change relative to the constant climate/no-aerosols run. The inset shows the period with transient temperatures until 2300 in more detail. Panel f displays the volume change of each RCP scenario when aerosols are considered relative to the no-aerosols run. The higher the temperatures, the more influential are the aerosols.

In the year 2100, the volume change relative to no aerosols (Fig. 3.7f) is below one percent for all scenarios. For RCP8.5 it is −0.26 % and for RCP4.5 −0.16 %.
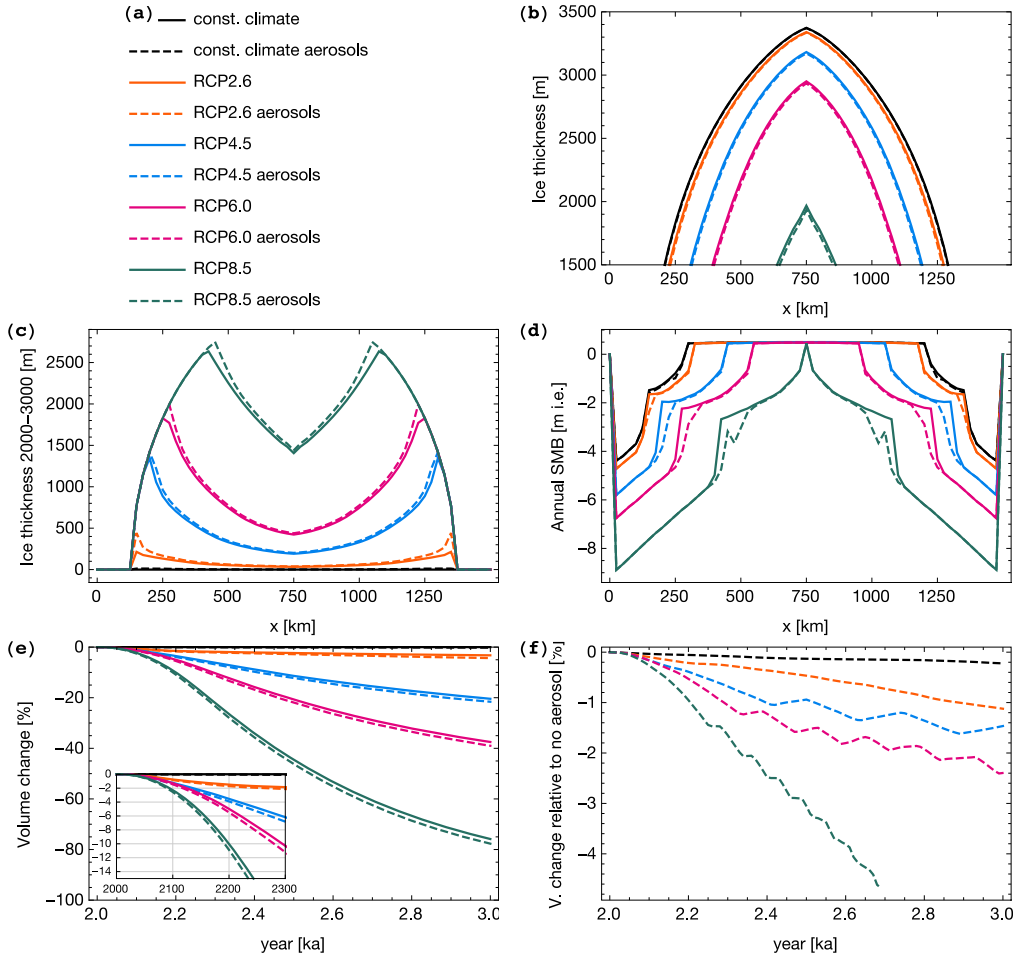
Figure 3.7: Results of the simulations driven by the representative concentration pathways: **(a)** common curve styles, **(b)** ice thickness in the year 3000, **(c)** elevation difference compared to the constant climate run, **(d)** SMB in the year 3000, **(e)** relative volume change compared to the constant climate/no-aerosols scenario (inset: detailed plot for the period until 2300) and **(f)** volume change due to the inclusion of aerosols.

In the year 2300, the influence of aerosols for RCP 2.6 is −0.08 %, for RCP 4.5 −0.68 %, for RCP6.0 −1.05 % and for RCP8.5 −1.65 %. After the year 2300, the temperatures remain unchanged at the 2300 level, and the ice dynamics still responds to the increased melt at the margin, and in addition aerosols continue to accumulate and fade away.

In the year 3000, the ice sheet volume is 1.46 % smaller for RCP4.5 and 7.61 % smaller for RCP8.5 when aerosols are considered.

3.4.3 RCP4.5 in more detail

The evolution of the RCP4.5 simulation with aerosols (RCP4.5 aerosols) is now presented in more detail. Figure 3.8 shows the ice albedo time series, in which the low values at the very margin are caused by dust (see Fig. 3.9a and c). The low values below 0.40 close the accumulation zone are caused by BC, as the younger ice there contains BC from the period with higher concentrations. Until 2300 black carbon lowers the ice albedo of up to three grid points, and later on only one is affected.

The main part of the ablation zone in Fig. 3.9 has low values of aerosol concentrations. This is because the englacial BC is 0 when the age of the ice is younger than at the start of the time series but older than glacial ice with high dust concentrations. Therefore, the BC content at the surface is only due to the atmospheric deposition which is low (Goelles and Bøggild, 2015). The surface amount of BC accumulates to just $200 \, \text{ng m}^{-2}$. The surface content of dust contains, besides the atmospheric signal, melt-out of the low englacial concentration during the Holocene of $20 \, \text{ng g}^{-1}$ and accumulates to $0.4 \, \text{g m}^{-2}$. The combined effect of dust and BC causes a constant albedo reduction of about 1.0 %. This causes a lower SMB in the central part of the ablation zone when aerosols are considered (Fig. 3.7).

Irregular peaks in the aerosol concentration can be seen in the englacial concentrations in panels a and b. Those peaks cause also higher amounts of aerosols at the surface due to the slow loss of aerosols at the surface. Nevertheless, over millennial time scales, the prolonged residence time of some decades is comparably short. This can be seen for example in Fig. 3.9b and d after the year 2550.

Figure 3.10 shows the volume change relative to the RCP4.5 simulation without aerosols, and how the results depend on different parameter values. The blue thick line is the same as in Fig. 3.7f. The simulations marked with † are compared to another reference. Run RCP4.5 mound aerosol † is compared to a run with
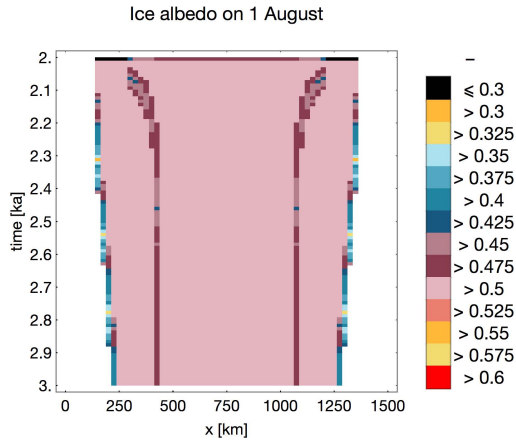
Figure 3.8: Simulation RCP4.5 aerosols: ice albedo on 1 August.

mound topography and RCP4.5 conditions but no aerosols. RCP4.5 + 20 % precip † is compared to a simulation with 20 % more precipitation and RCP4.5 conditions but no aerosols. Simulation RCP4.5 aerosols † is compared to a reference for which the ice albedo already considers the 1.0 % reduction mentioned above. Experiment RCP4.5 mound aerosol † uses 500 m mounds from the EISMINT (experiment K) set-up, and the volume change is calculated from a spin-up with these mounds. The effect of aerosols is slightly lower during the simulation but very close to the original simulation in the year 3000.

The highest impact of aerosols was reached with an active fraction $\mathcal{F}$ of 0.8, closely followed by an effective depth d_{eff} of 3 m. Both parameters determine how much aerosols influence the ice albedo.

Considering only BC (RCP4.5 BC only) leads to 0.42 % and dust alone to 1.16 % additional ice sheet volume loss in the year 3000 compared to the simulation RCP4.5 without aerosols. Therefore, dust is responsible for the major part of ice sheet loss.

3.5 Discussion

3.5.1 The effect of aerosols on ice volume

The additional ice loss caused by aerosols increases non-linearly with temperature (Fig. 3.7e and f). The non-linearity is caused by the relationship between BC concentration and albedo reduction (Fig. 3.14) as well as a positive feedback
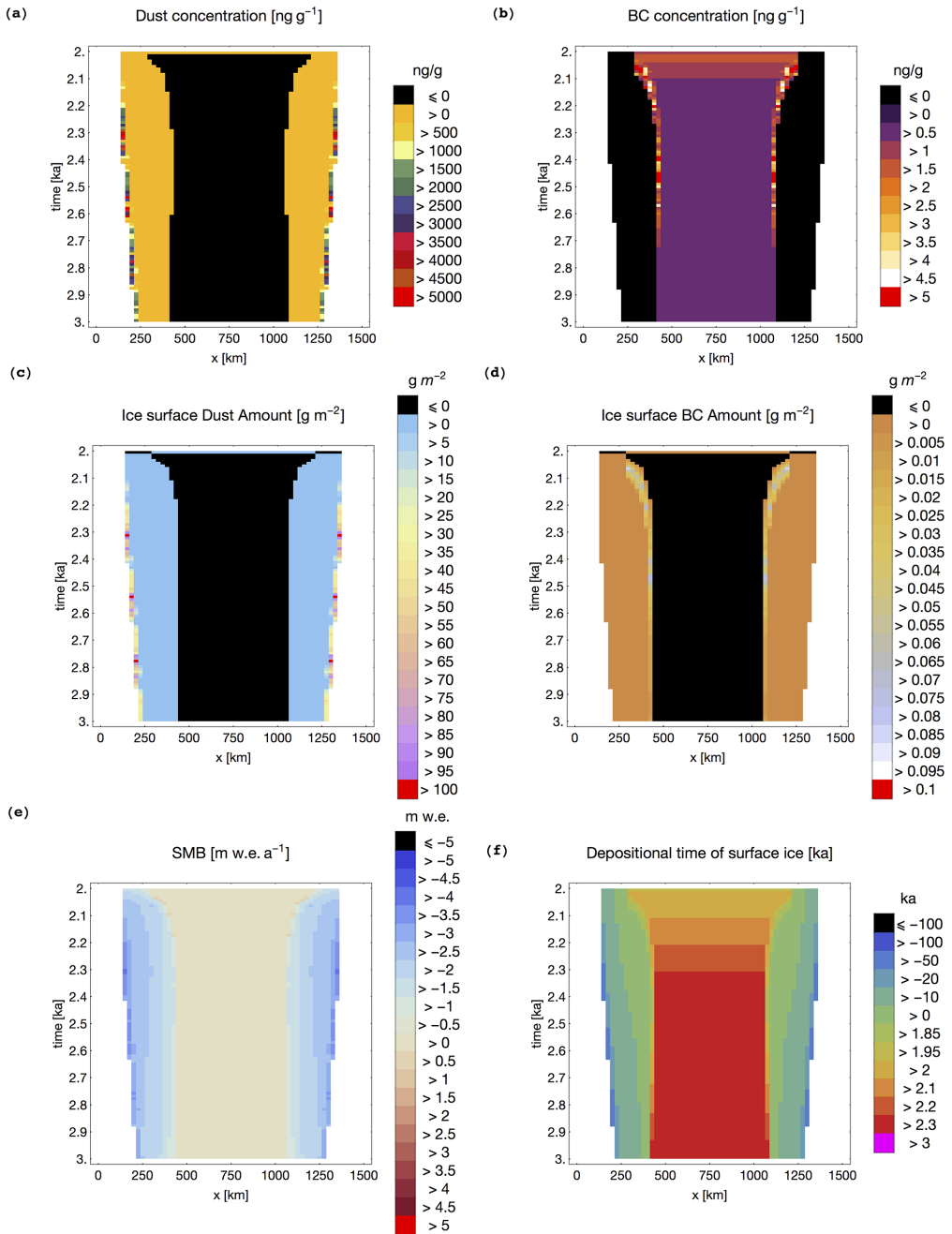
Figure 3.9: Time series of the RCP 4.5 scenario including aerosols: **(a)** englacial dust, **(b)** BC concentrations, (**c** and **d**) respective surface amount on 1 August, **(e)** surface mass balance and **(f)** depositional time of ice at the surface.
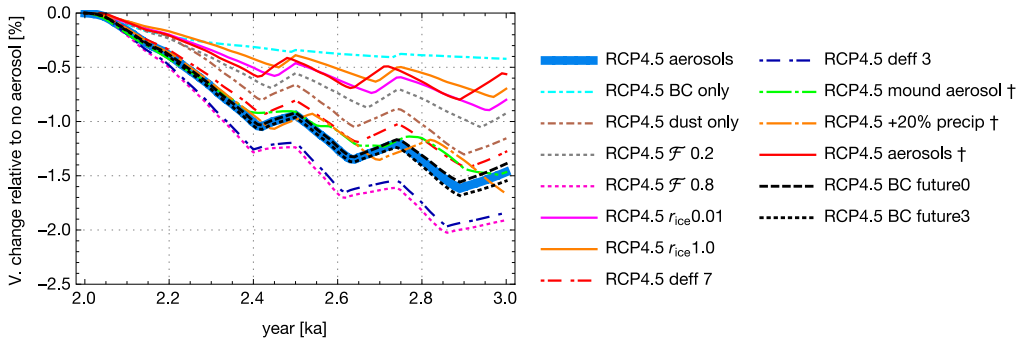
Figure 3.10: Simulations with RCP4.5 forcing: ice sheet volume change with aerosols (for different parameter settings) compared to the standard RCP4.5 run without aerosols. Simulations marked with a † are compared to a different reference; see main text.

between ice melt and aerosol accumulation. We did not include other feedbacks such as the elevation feedback and the albedo feedback to temperature. There is a weak negative elevation feedback included due to the parameterisation of the transmissivity (Robinson et al., 2010). Otherwise, the elevation and albedo feedbacks are positive, which further enhances melt. Due to this, and since we used global temperature anomalies for the simulations, the strength of the aerosol effect found in this study is expected to be a lower boundary.

The two BC scenarios (RCP4.5 BC future0 and RCP4.5 BC future3) result in a similar evolution as the standard set-up. This is a consequence of the time lag between aerosol deposition and melt-out at the ablation zone. Only the highest grid point in the ablation zone is affected by aerosols deposited after 2000 (see Fig. 3.9f). Therefore the effect of different BC and also dust emissions from the year 2000 onwards is limited until the year 3000. Nevertheless, BC and dust deposition has a direct effect on snow albedo and a long-term effect on ice albedo.

Ice albedo is sensitive to the small addition of impurities when the ice is clean (Fig. 3.14a). If the same amount of impurities is added to an already dark ice surface, the additional effect is weaker as compared to a clean surface. This could lead to an overestimation of the effect, whereas the missing feedbacks can lead to an underestimation; which effects dominate requires additional research. Nevertheless, the non-linear nature of the effect and the amplification due to rising temperatures presented in this study remain.

3.5.2 Assumptions, simplifications and uncertainties

The magnitude and non-linear dependence on future temperature of the aerosol effect were shown with a new model framework and applied to a simplified geometry experiment. Here we discuss if and how the assumptions and simplifications could have lead to an overestimation of the effect.

The experiments were performed using a flat bedrock topography; however, the effect of 500 m high mounds was also investigated (Fig. 3.10, run RCP4.5 mound aerosol †). The effect was sometimes weaker but very similar at the end of the simulation. The topography of the bedrock below the Greenland ice sheet is more complicated than sinusoidal mounds (Bamber et al., 2013); nevertheless, the effect remained even though the timing when aerosols emerge is influenced by the topography.

The ice dynamics module was compared to an analytical solution (Cuffey and Paterson, 2010). Close to the ice margin the shallow-ice approximation employed can be violated, and thus velocities can be computed incorrectly when the surface slope is steep (e.g. Ahlkrona et al., 2013; Greve and Blatter, 2009). This typically occurs in areas where the ice sheet reaches the coast and calving is present. However, in our case, we have pronounced ablation zones on both sides of the two-dimensional domain (Fig. 3.13). Therefore, the simulated ice sheet never reaches the boundaries of the domain and maximal surface slopes at the ice margin are just around $1°$, which is well within acceptable limits for the validity of the shallow-ice approximation.

The tracer transport, which is used to derive the englacial aerosol concentration, influences the rate of melt-out and therefore the amount of accumulated aerosols on the ice surface. The accuracy of the module depends on the velocities and the numerics of the transport scheme. Here we use a first-order scheme which was found to deliver different results in the ablation zone (Goelles et al., 2014). Nevertheless the calculated ages are comparable to radio stratigraphy from Greenland (MacGregor et al., 2015) as the horizon of the boundary between Holocene and glacial ice is at similar depths.

The aerosol time series of mineral dust and BC have a more direct effect on the results. They determine the englacial concentration, which directly influences the ice albedo and determines the amount of melt-out. We assumed that the aerosol concentration solely depends on the age of the ice because distant ice cores correlate well (Bigler, 2012).

However, if this were not the case, and aerosols were deposited in smaller patches rather than uniformly, then they would also be released in smaller areas

in the ablation zone. Owing to the reduced response when aerosols are added to an already dark surface (Fig. 3.14), the effect of aerosols would then be smaller.

Nevertheless, close to the ELA the surrounding tundra could contribute locally to the englacial dust concentration (Wientjes et al., 2012). As mentioned in Goelles and Bøggild (2015) there might be a "threshold elevation" up to which local dust contributes.

BC concentration peaks due to forest fires (Fig. 3.3) are only available between 1788 and 2000. Also, dust ice core data of the Holocene are not available. Since the central part of the ablation zone has its origin in the Holocene, the englacial aerosols consist of only dust which has a low and constant value. This is the cause for the slight decrease of albedo in the centre part of the ablation zone.

The aerosol accumulation determines the amount of aerosols which darken the ice surface and therefore plays an important role in the overall estimation of the effect. The direct input from the atmosphere (k_{II}) was constant in this study, and the input from the tundra was 0. This is most likely true for BC as local sources on Greenland are negligible. Below the "threshold elevation", dust from the surrounding tundra might contribute significantly. The dust amount at the margin is already large due to melt-out of glacial dust. Therefore, an additional amount of dust from the tundra has a smaller effect as the surface is already dark (Fig. 3.14). Beside the input, the daily reduction on ice r_{ice} determines the surface amount. This parameter was found to be of the order of 1 per mille per day, which is comparable with measurements (Goelles and Bøggild, 2015). Under warming scenarios, the daily reduction might increase with increased surface run-off due to meltwater and rainfall, which would have a stabilising effect that is currently not captured.

Under recent conditions, the amount of meltwater run-off is typically 1 to 2 magnitudes higher than summer rainfall. Therefore, even with more rainfall during summer in the future, the potential increase of the daily reduction will most likely be determined by the meltwater run-off.

The relationship of aerosols and ice albedo depends on the specific surface area of ice, englacial concentration, the amount at the surface, the conversion to BC concentration and the darkening parameterisation as well as the active fraction $\mathcal{F}$. The conversion to concentration is necessary because of the formulation of the darkening parameterisation and depends on the effective depth d_{eff}. The value is based on the absorption length in ice which varies greatly with wavelength (Warren and Brandt, 2008). The conversion of mass per area to concentration (ppm) would not be necessary if an ice albedo reduction parameterisation based on mass of BC per area existed. Also, the active fraction $\mathcal{F}$ is similarly powerful as the

effective depth and not well constrained. The parameter lumps together all surface processes which keep aerosols from darkening the ice surface. This part of the model is based on a lower level of understanding and yet causes a wide spread in the outcome; therefore it requires more attention (see Goelles and Bøggild, 2015; Hodson, 2014). Nevertheless, even at a low active fraction or a high effective depth the effect remains (Fig. 3.10).

The surface mass balance determines the snow depth, which governs how long ice is exposed and the amount of outcropping aerosols (k_{III}). The time span of ice exposure is important for the actual effect of ice albedo and, secondly, for the period of aerosol reduction ($r_{\mathrm{ice},n}$). Especially the long-wave radiation coefficient λ is very influential as it scales the temperature dependence of melt (Fig. 3.14). Nevertheless, tests with data from western Greenland showed results comparable to observations (Goelles and Bøggild, 2015).

Overall the magnitude of the effect of aerosols depends on all the parts discussed, but even though limitations exist the effect is intuitively understandable. More ice melt causes an increase of outcropping aerosols, which have a long residence time at the surface. These aerosols darken the ice surface, which further enhances ice melt. The presented model components capture the main effect, while the exact timing when and where aerosols emerge is harder to achieve.

3.6 Conclusions

We tested the ice volume response to darker ice in the ablation zone caused by accumulation of dust and black carbon. We introduced a new model framework which includes advection, melt-out and accumulation of aerosols and its darkening effect on the surface mass balance. The response of the ice volume to the aerosols depends non-linearly on the future temperature because of a positive feedback between ice melt and aerosol melt-out which is disproportionally larger in warmer climate scenarios. The exact timing when and where darkening occurs is difficult to achieve; however, the overall effect is captured with the presented framework.

In order to isolate the effect of ice albedo, we kept the snow albedo unaffected by impurities. A 0.01 lower fresh snow albedo causes a decrease of $27\,\mathrm{Gt\,a^{-1}}$ of the total surface mass balance for the Greenland ice sheet (Dumont et al., 2014). Therefore the combined effect of impurities on snow and ice albedo is significantly larger then the ice albedo effect alone.

The effect of black carbon from the industrial revolution was significant and will have an effect for a long time to come. Currently, Asian black carbon emissions

are rising which could lead, besides to the darkening of snow, to darker ice via direct deposition and over long time scales via ice flow.

The presented principles are not just limited to Greenland in the future but could also be applied to palaeo-climatic studies, detailed studies for alpine glaciers or the termination of the little ice age (Painter et al., 2013).

We investigated the response under the RCP4.5 scenario in more detail and tested the sensitivity to several parameters. Considering that the temperatures in the Arctic rise higher than the global mean and the elevation and ice albedo feedbacks were not considered, the estimated effect can be seen as a lower boundary estimate. The presented simulations were based on a simplified geometry in two dimensions; nevertheless the age structure and overall system resembles the Greenland ice sheet. The presented simulations should not be seen as forecasts but emphasise the importance of the effect.

The Supplement related to this article is available online at doi:10.5194/tc-9-1845-2015-supplement

Acknowledgements
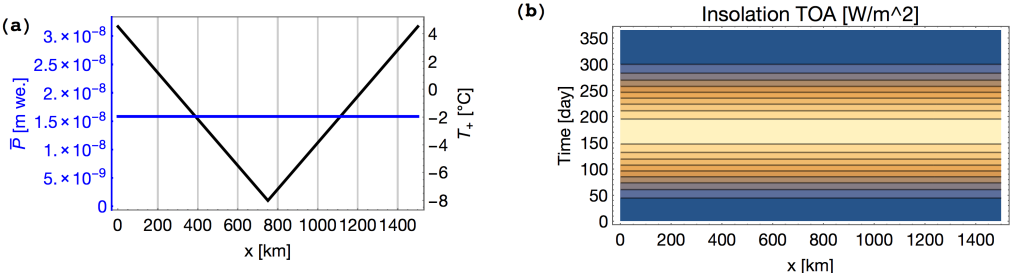
3.7 Supplement

Figure 3.11: Climate conditions for the spin-up: **(a)** mean summer surface temperature and annual mean precipitation over the whole domain, **(b)** insolation S_{TOA} on top of the atmosphere at $67°$ N.

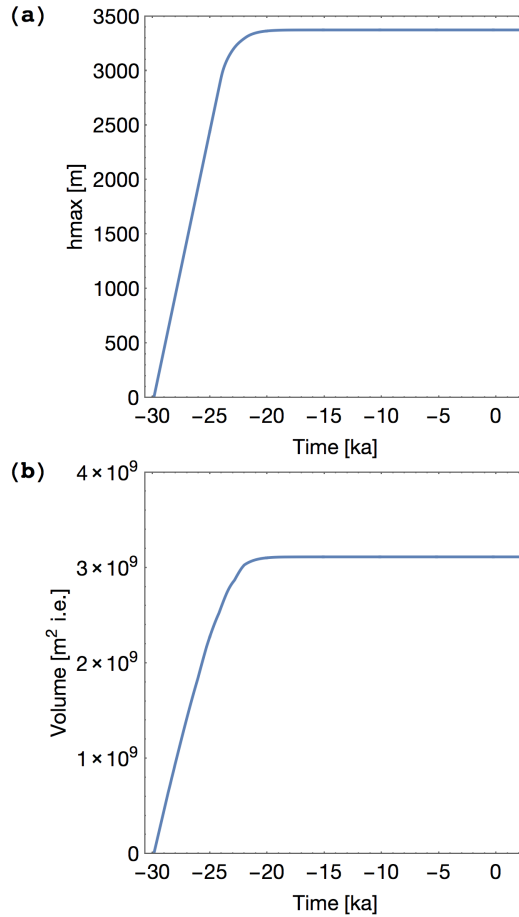**Figure 3.12:** Spin-up: **(a)** evolution of the maximum ice thickness, **(b)** evolution of the ice volume. Equilibrium is reached after approximately 10 ka.
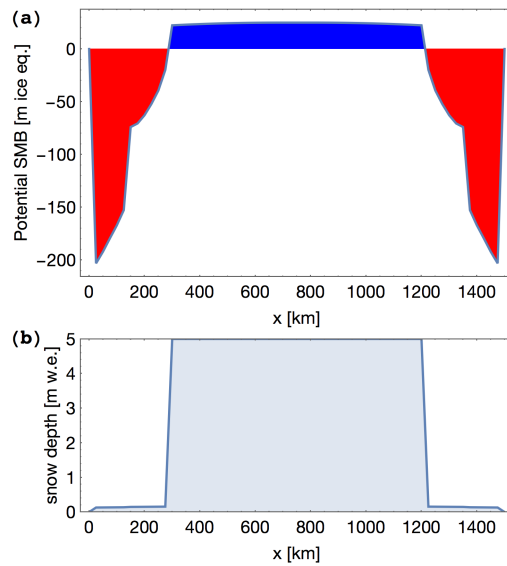
Figure 3.13: End of the spin-up: **(a)** potential surface mass balance for the 50 year time step, **(b)** snow thickness on 1 January. The SMB and snow depth are not calculated at the outermost points, which are never reached by the ice sheet.
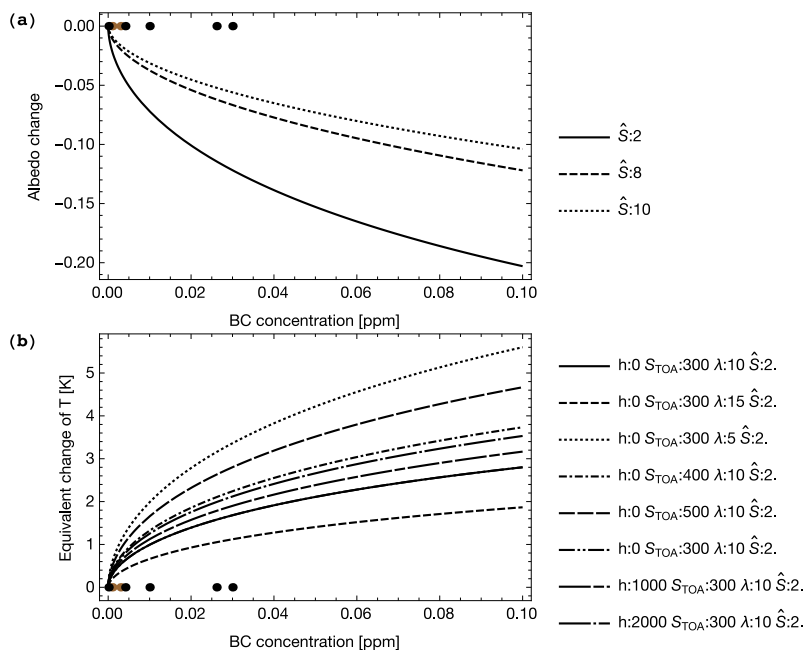
Figure 3.14: Black carbon (BC) influence on albedo: **(a)** for different specific surface areas of ice in $\mathrm{cm^2\,g^{-1}}$ (Gardner and Sharp, 2010), **(b)** melt-equivalent temperature change for different parameters of the SMB model. The dots indicate measured BC (black) and dust concentrations both from ice cores and from converted surface values as a reference. The influence of additional BC is strongest when the initial BC concentration is close to zero. See also the interactive CDF (Computable Document Format) file S4.cdf (included in the Supplement) for further details.

Chapter 4

Article III

Goelles, T., Grosfeld, K. and Lohmann, G.

Semi-Lagrangian transport of oxygen isotopes in polythermal ice sheets: implementation and first results

Abstract

Modelling the evolution of the Earth system on long timescales requires the knowledge and understanding of driving mechanisms, such as the hydrological cycle. This is dominant in all components of the Earth's system, such as atmosphere, ocean, land surfaces/vegetation and the cryosphere. Observations and measurements of stable water isotopes in climate archives can help to decipher and reconstruct climate change and its regional variations. For the cryosphere, the δ^{18}O cycle in the current generation of Earth system models is missing and an efficient and accurate tracer transport scheme is required. We describe ISOPOLIS 1.0, a modular semi-Lagrangian transport scheme of second-order accuracy, which is coupled to the polythermal and thermomechanical ice sheet model SICOPOLIS (version 2.9). Model skill is demonstrated by experiments with a simplified ice sheet geometry and by comparisons of simulated ice cores with data from Greenland (GRIP) and Antarctica (Vostok). The presented method is a valuable tool to

investigate the transport of any kind of passive tracer inside the cold ice part of a polythermal ice sheet and is an important step to model the whole $\delta^{18}O$ cycle.

4.1 Introduction

Oxygen isotopes are an important proxy for the reconstruction of temperatures of the past. Air temperature is related to stable isotopic composition of precipitation as indicated by observations (e.g. Dansgaard, 1964; Gat, 1996; Jouzel et al., 1997; Gornitz, 2009). When assuming this relationship remains the same in the past, it is possible to reconstruct past temperatures from ice or sediment cores. To model the whole isotopic cycle in an Earth system model (ESM), components for the atmosphere, ocean and cryosphere are required. The biggest components of today's cryosphere are the two huge ice sheets of Greenland and Antarctica which together contain about 99 % of the Earth's ice volume and about 80 % of global fresh water. Therein and in smaller glaciers ice appears in two different states; as "cold" ice with temperatures below the pressure-melting point and "temperate" or "warm" ice where temperatures are at the pressure melting point. Ice masses neither pure "cold" or "temperate" are called polythermal ice. Temperate ice may have liquid water in it and, therefore, may be considered as at least a two-component fluid. In ice sheets this temperate ice may exit as a thin layer near the base. Although it is much less in volume than cold ice, temperate ice has significant consequences on the ice dynamics (Lliboutry and Duval, 1985) and therefore on isotope and tracer transport in general.

Models for oxygen isotopes in the atmosphere, ocean and land-biosphere have existed for some time (e.g. Jouzel et al., 1987; Hoffmann et al., 1998; Sturm et al., 2010) but the cryospheric part was first successfully modelled by Clarke and Marshall (2002) for Greenland. Until then, thermomechanical ice sheet models were mainly unsuccessful or had large limitations in their dimension, spatial extent, temporal coverage or steady-state assumptions. Problems were mainly associated with the Eulerian scheme which is commonly used to solve for advection processes in numerical ice sheet models. The main problems are discontinuities of the advected property which is usually tackled by an artificial diffusion term. This leads to an inaccurate solution near the base, and reliable solutions for tracer dispersion are only optioned for the upper half of the ice sheet (Rybak and Huybrechts, 2003).

Clarke and Marshall (2002) and the follow-up papers (Clarke et al., 2005; Lhomme et al., 2005a,b), therefore, use a semi-Lagrangian scheme to track

passive tracers. Tarasov and Peltier (2003) also uses a semi-Lagrangian scheme to model the transport of δ^{18}O directly while Clarke and Marshall derived the δ^{18}O value indirectly via ice age and ice provenance. In a semi-Lagrangian scheme a regular grid is used and particles are usually tracked back to its origin from one time step before. This backtracking is of importance for the overall performance and accuracy. A review by Staniforth and Côté (1991) recommends at least second-order accuracy for the backtracking scheme. Clarke and Marshall (2002), Clarke et al. (2005) and Lhomme et al. (2005a,b) use a first-order backtracking scheme in their ice sheet model, considering cold ice only.

In this study we are using the second-order backtracking scheme of de Almeida et al. (2009) together with a polythermal ice sheet model to simulate the δ^{18}O distribution in ice sheets. The whole model consists of three components: a polythermal ice sheet model, a semi-Lagrangian transport module and a post-processing tool which are described in detail in Sect. 4.2. As polythermal ice sheet model we use SICOPOLIS (Version 2.9.) which is based on Greve (1997a,b). SICOTRACE and SICOSTRAT are two new components designed for semi-Lagrangian transport and the reconstruction of the stratigraphy. While SICOTRACE calculates the transport variables, SICOSTRAT can be used to generate cross sections along grid points and ice cores at arbitrary locations with information such as δ^{18}O concentration, place of origin and age of the ice. The performance of the model is demonstrated with a simplified geometry of the EISMINT (Payne et al., 2000) inter-comparison project and later applied to Greenland and Antarctica (Sect. 4.3). A summary of the paper and general conclusions are given in Sect. 4.4.

4.2 Model description

The diffusion of δ^{18}O over multi-annual periods is considered to be negligible in cold ice (e.g. Jean-Baptiste et al., 1998). Therefore, it can be considered as a passive tracer in cold ice which is not altered chemically or physically on its way through the ice sheet and does not influence the flow.

When ice crosses the cold–temperate surface (CTS) and enters the temperate regime the passive trace assumption is no longer true since diffusion is possible in the liquid water which my be present there. Therefore it would be possible to introduce a marker which indicates whether the ice crossed the CTS at some time in its flow history. This would possibly aid ice core interpretation but will not be implemented at this stage in the model.

The advection of such a passive tracer in Eulerian description is

$$\frac{\partial \Psi}{\partial t} + \vec{v} \cdot \nabla \Psi = 0, \tag{4.1}$$

where the transported property Ψ itself and its gradient must be given. This is not the case when discontinuities are present, e.g. when two ice-flow branches are merging or when the surface mass balance or conditions near the bedrock are changing (Clarke et al., 2005).

In contrast, a Lagrangian description is not influenced by such discontinuities as individual particles are tracked, although the Lagrangian description encounters other problems such as error accumulation along the trajectory because of the required velocity interpolation (Rybak and Huybrechts, 2003). Due to the divergence of ice flow there are areas with very low particle density which lead to very low information density at the same time. This necessitates having a large number of modelled particles whereby new ones are constantly introduced at the ice surface and old ones are removed at the ice sheet's base (Lhomme, 2004). These and other practicalities linked to the irregular grid render Lagrangian schemes unsuitable in ice sheet modelling.

To overcome the drawbacks of the Eulerian and Lagrangian scheme, the semi-Lagrangian scheme tries to combine the best of both, namely the regular grid of the Eulerian and the better stability of the Lagrangian scheme.

4.2.1 Temperature reconstruction with water isotopes

Today's $\delta^{18}O$ ratio in snow at any given location is controlled by the local temperature, the amount of precipitation, the distance from the coast and the altitude (e.g. Gornitz, 2009). Analyses indicate a strong correlation between $\delta^{18}O$ and surface temperature, especially for temperatures below $20\,^{\circ}C$ in mid-to-high latitudes and with the amount of precipitation at low latitudes.

The measured correlation between $\delta^{18}O$ and temperature in polar regions is strongest for annual means (e.g. Gornitz, 2009). Observational data indicate that the relationship of temperature and $\delta^{18}O$ are not spatially uniform and that it can be described as a linear function of the surface temperature $T_{\rm s}$ (Eq. 4.2) or a function of the present $\delta^{18}O$ value, local surface elevation ΔS and of temperature
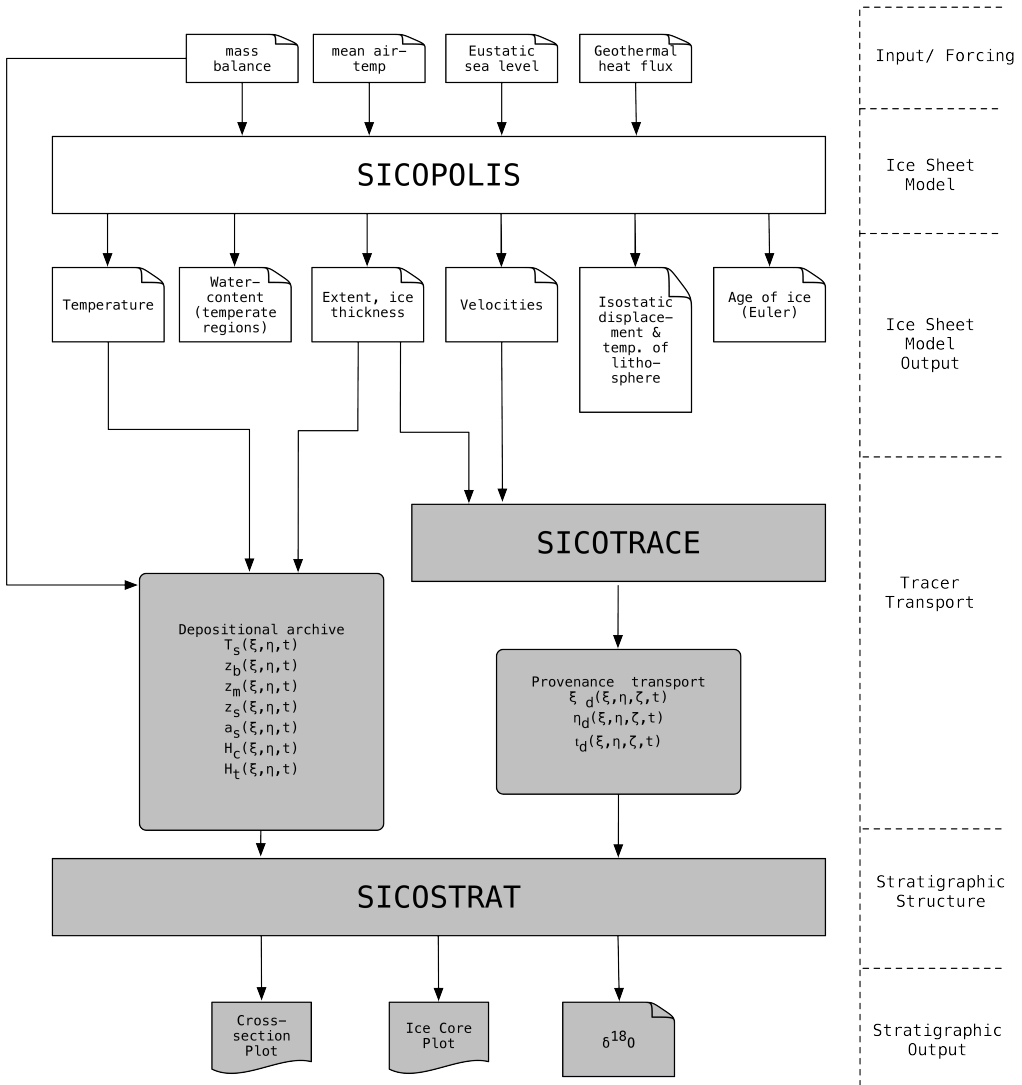
Figure 4.1: Flow chart of the three programs included in ISOPOLIS: SICOPOLIS – the polythermal ice sheet model. SICOTRACE the tracing program which uses the output from SICOPOLIS and calculates the semi-Lagrangian tracer transport method. SICOSTRAT is the plotting routine for the construct of the stratigraphy.

change ΔT over the ice sheet (Cuffey, 2000) (Eq. 4.3):

$$\delta^{18}O(x, y, t) = f(T_s(t, x, y)) \tag{4.2}$$

$$\delta^{18}O(x, y, t) = f(\delta^{18}O(x, y), \Delta T, \Delta S). \tag{4.3}$$

4.2.2 General framework

Clarke and Marshall (2002) formulate an indirect approach by transporting so-called "depositional provenance labels" t, x, y and by maintaining a "depositional archive" with information about surface temperatures, ice topography and mass balance (see Fig. 4.1). Hence, it is possible to reconstruct the $\delta^{18}O$ value with a transfer function in the form of Eqs. (4.2) or (4.3) and get the additional benefits of information of age and transport.
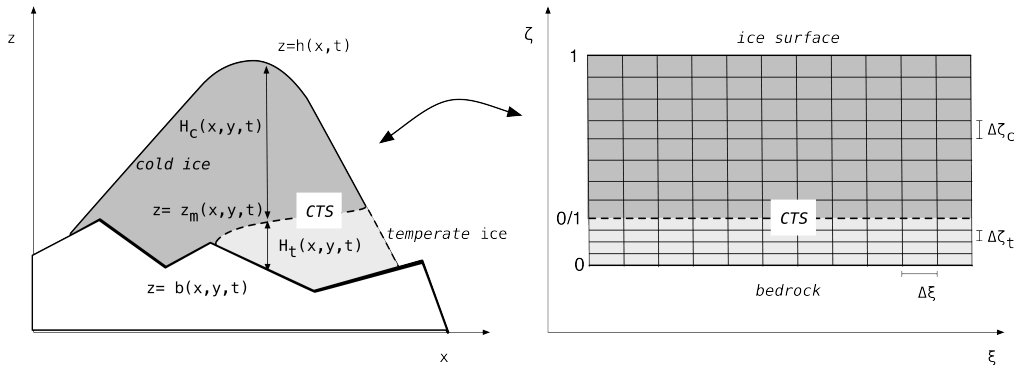

Figure 4.2: Terrain-following sigma transformation in the polythermal ice sheet. If temperate ice is present it is always below the cold ice. Hence, there are two separate sigma-transformed regular grids above each other, and they share their horizontal coordinate $x \to \xi$ and $y \to \eta$ (not shown here). The grid spacing $\Delta\zeta_c$ and $\Delta\zeta_t$ for cold and temperate are usually different and also the sigma-transformation is different for both domains (see Greve, 1997a). CTS denotes the cold–temperate surface.

If the history of the surface temperature is stored and the time and place of origin is known, the $\delta^{18}O$ can be calculated by inverting Eqs. (4.2) or (4.3). The history of the surface temperature is a climate variable which can either be an external input from an atmospheric model or prescribed as is the case here.

The other information of the origin (x, y) and time (t) of deposition is transported with the ice flow and is not altered on its way, i.e. it is a passive tracer. In order to

calculate a passive tracer, the velocity field needs to be known, which is calculated by the ice sheet model SICOPOLIS in our study.

Tarasov and Peltier (2003) modelled $\delta^{18}O$ directly and use a very high vertical resolution of up to 4096 layers on a sub-grid near ice core locations. Their approach is not feasible for our purpose because we need to know the $\delta^{18}O$ value in the whole ice sheet in order to close the hydrological cycle in the ESM framework.

The new transport model consists of three separate modules: SICOPOLIS which is the polythermal ice sheet model, SICOTRACE which is the tracer transport model and SICOSTRAT which reconstructs the stratigraphy. Figure 4.1 illustrates the framework with in- and outputs of each component.

4.2.3 Polythermal ice sheet model SICOPOLIS

SICOPOLIS (Greve, 1997a) is a three-dimensional polythermal ice sheet model and is based on the shallow ice approximation. The model has been applied previously for Greenland, Antarctica, the polar ice caps of Mars and the entire Northern Hemisphere. As input it uses the surface mass balance, mean air temperature, eustatic sea level and geothermal heat flux (e.g. Greve, 1997b). As output, temperature, water content in temperate regions, ice extent and thickness, ice velocities, isostatic displacement and the temperature of the lithosphere are calculated. In this study, the velocities in the cold ice v_c and temperate ice v_t, and the respective thickness H_c and H_t are of major importance. The two domains are separated by the CTS at $z = z_m$ (see Fig. 4.2). As an input for the transport component SICOTRACE the three-dimensional velocity field in the cold and temperate region as well as the ice extent and thickness is stored for every time step (Fig. 4.1) in a netCDF file (UNIDATA, 2016).

The numerical grid

SICOPOLIS uses three grids with different sigma-transformations on top of each other (see Fig. 4.2). A grid for the lithosphere is overlaid by a grid for temperate ice below cold ice. In general, values in the cold ice domain are denoted with subscript c and in the temperate region with subscript t.

For cold ice the σ-transformation is

$$x = \xi_c \tag{4.4a}$$

$$y = \eta_c \tag{4.4b}$$

$$z = \frac{H_c(e^{a\zeta_c} - 1) + z_m(e^a - 1)}{(e^a - 1)} := \sigma_c \tag{4.4c}$$

$$t = \tau_c, \tag{4.4d}$$

where a is a stretching parameter which is 5 herein (Greve, 1997a).

The transformation in temperate ice with bedrock elevation b (see Fig. 4.2) is

$$x = \xi_t \tag{4.5a}$$

$$y = \eta_t \tag{4.5b}$$

$$z = \zeta_t + bH_t := \sigma_t \tag{4.5c}$$

$$t = \tau_t. \tag{4.5d}$$

With this sigma transformation the depositional provenance labels are ξ_d, η_d, τ_d.

The two domains for cold and temperate ice use an Arakawa C-Grid (Arakawa, 1997) with the velocity components at intersections between grid point centres. In this grid the velocity components in cold and temperate ice, beside gradients, are placed in between grid points. All the other values, like temperature or water content for example are defined on the grid centre, itself.

The two different grids in the polythermal ice sheet model and the fact that the ice extent and the thicknesses of cold and temperate ice changes with time makes the semi-Lagrangian transport more difficult for glacier models than for atmospheric or ocean models. This will be discussed in more detail in the next section.

4.2.4 Semi-Lagrangian transport module SICOTRACE

SICOTRACE stands for SImulation COde of TRACErs and is a separate program which reads SICOPOLIS outputs and calculates the transport of the three provenance variables. In this section the semi-Lagrangian transport with backward trajectories is described as well as the problems and remedies associated with the specifics of ice sheet models, especially for polythermal ice.
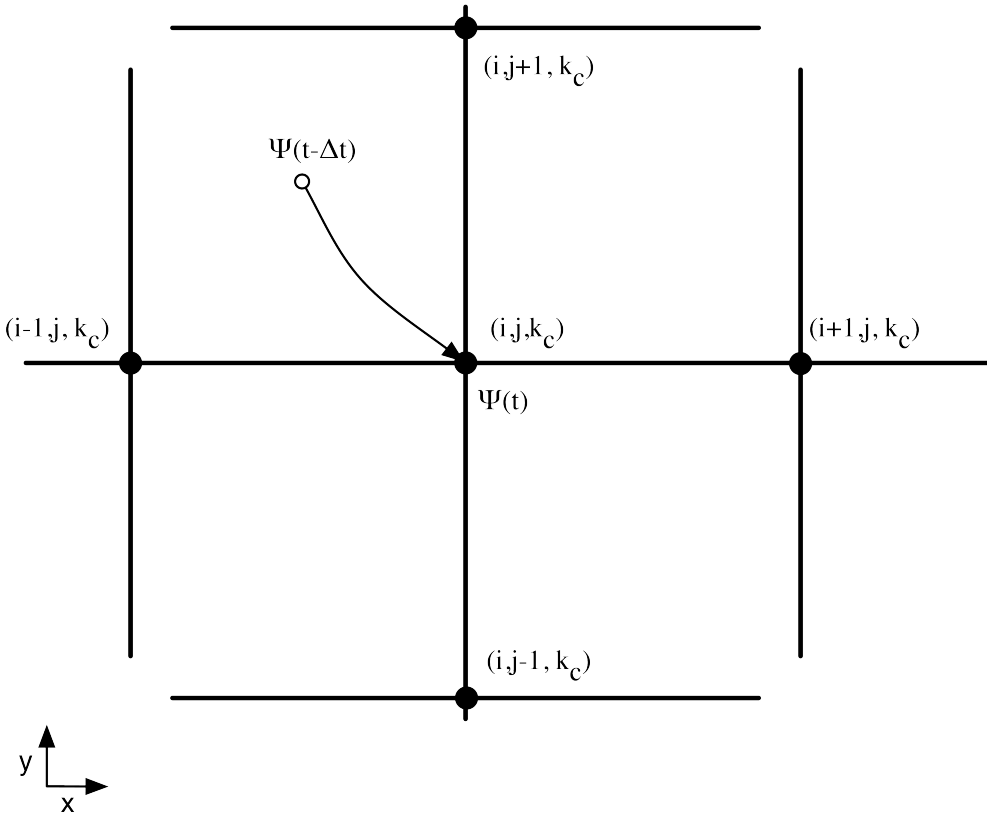
Semi-Lagrangian scheme

Figure 4.3: Basic principle of the semi-Lagrangian method explained in the cold ice grid. If the value of $\Psi(t - \Delta t)$ at the departure point (open circle) is known, the value $\Psi(t)$ at the desired grid point (i, j, k_c) can be calculated, where i and j are the indices of the horizontal grid and k_c the one for the vertical sigma coordinates in cold ice.

The basic idea of a semi-Lagrangian scheme is illustrated in Fig. 4.3. A transported property Ψ is constant over time and is not changing along its trajectory:

$$\frac{\mathrm{d}\Psi}{\mathrm{d}t} = 0. \tag{4.6}$$

If the place of origin at time $t - \Delta t$ is known, then the value of $\Psi(t)$ at the current time step is also known. A standard semi-Lagrangian scheme uses a regular spaced grid, and for each grid point the back trajectory is calculated to get the

position of the particle at one time step before. This position is usually not on the grid. Therefore, an interpolation is required to get the value $\Psi(t - \Delta t)$ for which we used a trilinear interpolation (Press et al., 1996).

In order to reach high accuracy, a review of semi-Lagrangian schemes for atmospheric models by Staniforth and Côté (1991) recommends the use of a back-tracking method with at least second-order accuracy. However, in the original work by Clarke and Marshall (2002) and subsequent papers (Clarke et al., 2005; Lhomme et al., 2005a) a first-order approximation was used. Much research has been done in developing accurate, cheap and robust backtracking methods, (e.g. McGregor, 1993; Nair et al., 2003; Purser and Leslie, 1994; Staniforth et al., 2003; Hortal, 2002). For our application we opt for the scheme of de Almeida et al. (2009) because it is of second-order accuracy and its robustness for small and large Courant number in the presence of weak and strong flow curvature makes it well suited for a transient and three-dimensional ice sheet model.

Numerical grid for the semi-Lagrangian transport

In general it is possible to perform semi-Lagrangian transport on the same grid as used by the Eulerian ice sheet model. In a polythermal model, however, two layers with σ-transformed coordinates are stacked on each other. Therefore, a new grid consisting of the same horizontal grid as in SICOPOLIS but with a σ-transformation including both cold and temperate ice (see Fig. 4.4) has been formulated:

$$ x = \xi_\mathrm{s}, \quad y = \eta_\mathrm{s}, \quad z = \zeta_\mathrm{s}(H_\mathrm{t} + H_\mathrm{c}) + b := \sigma_\mathrm{s}, \quad t = \tau_\mathrm{s}. \qquad (4.7) $$

The time step for the semi-Lagrangian transport remains the same as in SICOPOLIS. In general, it could be longer than for the Eulerian ice sheet model but for now it is set to be the same as in SICOPOLIS.

Trajectory calculation

The backtracking method is important for the overall performance of a standard semi-Lagrangian transport scheme. Here, we use the second-order accuracy scheme of de Almeida et al. (2009) which allows the velocity and acceleration vectors of particles to vary between t and $t - \Delta t$. Figure 4.5 shows the scheme in one dimension. The scheme is based upon the general idea of multistage methods, where each integration step requires the estimate of the dependent
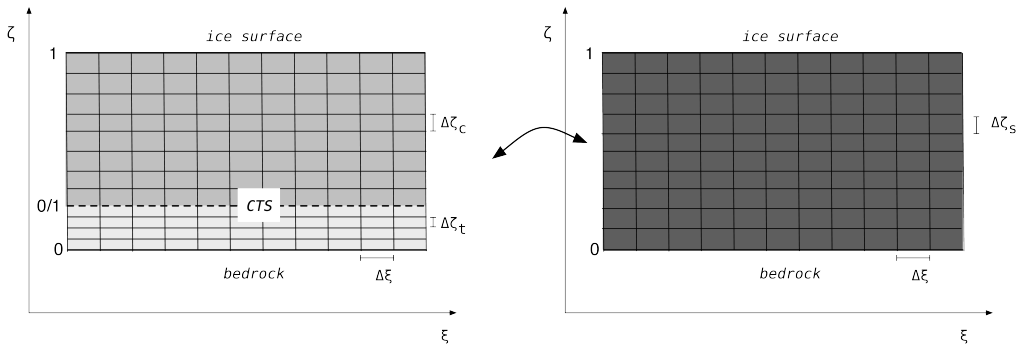
Figure 4.4: Semi-Lagrangian sigma-transformed grid. The original cold and temperate grid on the left are both covered by the semi-Lagrangian grid.

variable at several intermediate times, similar to Runge–Kutta (de Almeida et al., 2009).
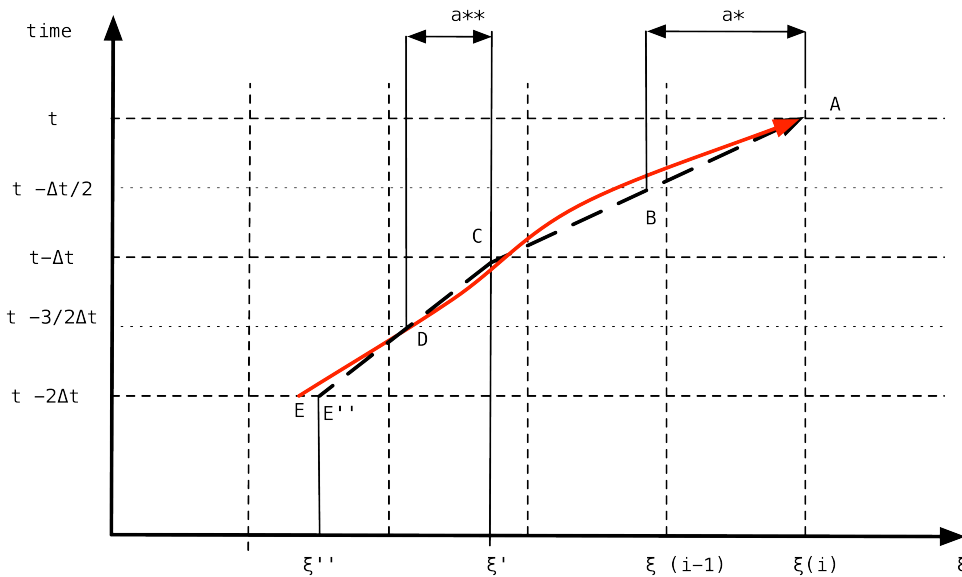
Figure 4.5: Schematic for the two-step three time level scheme for one dimension (ξ). The red solid curve is the actual trajectory of a particle and the dashed line is the approximation. a^* is the displacement to the intermediate position where the velocity is evaluated and a^{**} is the displacement of the second step.

Compared to first-order approximations the second-order scheme is known to be more accurate and exhibits better conservation properties (e.g. McGregor,

1993; Staniforth and Pudykiewicz, 1985). A discussion of the differences in our application is given below (Sect. 4.3.1).

Point A is the desired ending point on the grid point $\xi(i)$. The red line $\overline{EA}$ is the *exact* trajectory and the dashed black line $\overline{E''A}$ is the *approximate* one. We know the property Ψ at all grid points ξ_i at one $(t - \Delta t)$ and two time steps $(t - 2\Delta t)$ beforehand and we wish to obtain values at the same grid points at time t.

In this method the trajectory is split into two steps. In the first step, starting from grid point $\xi(i)$ at time t the particle is displaced backwards for a time interval Δt with the velocity calculated at an intermediate position at point B for time $t - \Delta t$. In the second step, starting from the particle position C at time $t - \Delta t$ calculated in the previous step, the particle is displaced backwards for another Δt, with the velocity calculated for the intermediate position D, also at time $t - \Delta t$. The intermediate points B and D are obtained by considering displacements of the particle for a time interval $\Delta t / 2$.

The velocities at point B and D need to be interpolated. For the interpolation of the velocity field we use a trilinear scheme which is sufficiently accurate (Behrens, 1996). The positions of the points themselves rely on the velocities and, hence, the whole process needs to be repeated until a convergence criterion of $\epsilon = 0.001$ m is met.

In three dimensions Eq. (4.6) is approximated by Eq. (4.8) by applying the described backtracking for all three co-ordinates (ξ, η, ζ_s):

$$\frac{\mathrm{d}\Psi}{\mathrm{d}t} \cong \frac{\Psi(\xi, \eta, \zeta_s, t) - \Psi(\xi'', \eta'', \zeta_s'', t - 2\Delta t)}{2\Delta t}, \tag{4.8}$$

where $\Psi(\xi'', \eta'', \zeta_s'', t - 2\Delta t)$ is usually not on the grid and is interpolated.

In three dimensions the first step is

$$a^{*(m+1)} = \frac{\Delta t}{2} \cdot v_x(\xi_i - a^{*(m)}, \eta_j - b^{*(m)}, \zeta^*, t - \Delta t) \tag{4.9a}$$

$$b^{*(m+1)} = \frac{\Delta t}{2} \cdot v_y(\xi_i - a^{*(m)}, \eta_j - b^{*(m)}, \zeta^*, t - \Delta t) \tag{4.9b}$$

$$c^{*(m+1)} = \frac{\Delta t}{2} \cdot v_z(\xi_i - a^{*(m)}, \eta_j - b^{*(m)}, \zeta^*, t - \Delta t) \tag{4.9c}$$

$$\xi' = \xi_i - 2a^* \tag{4.9d}$$

$$\eta' = \eta_i - 2b^* \tag{4.9e}$$

$$\zeta' = \sigma^{-1}(z' = z - 2c^*, H_c, H_t, z_m, b, t - \Delta t) \tag{4.9f}$$

and the second step is

$$a^{**(m+1)} =$$
$$\frac{\Delta t}{2} \cdot v_x(\xi' - a^{**(m)}, \eta' - b^{**(m)}, \zeta^{**}, t - \Delta t) \tag{4.10a}$$
$$b^{**(m+1)} =$$
$$\frac{\Delta t}{2} \cdot v_y(\xi' - a^{**(m)}, \eta' - b^{**(m)}, \zeta^{**}, t - \Delta t) \tag{4.10b}$$
$$c^{**(m+1)} =$$
$$\frac{\Delta t}{2} \cdot v_z(\xi' - a^{**(m)}, \eta' - b^{**(m)}, \zeta^{**}, t - \Delta t) \tag{4.10c}$$
$$\xi'' = \xi' - 2a^{**} \tag{4.10d}$$
$$\eta'' = \eta' - 2b^{**} \tag{4.10e}$$
$$\zeta'' = \sigma^{-1}(z'' = z' - 2c^{**}, H_c, H_t, z_m, b, t - \Delta t). \tag{4.10f}$$

Equations (4.9) and (4.10) are valid for cold and temperate ice with different velocities v_c, v_t and sigma transformations σ_c, σ_t. There are some difficulties associated with semi-Lagrangian transport and sigma coordinates in polythermal ice sheet models which are not encountered in models of other compartments of the climate system. These are discussed in the next section.

Polythermal ice sheet and sigma transformations

The sigma transformations σ_c, σ_t are dependent on the ice thickness of cold and temperate ice, the position of the cold–temperate surface and the bedrock elevation (see Eqs. 4.4c and 4.5c). These quantities are all dynamic which makes it necessary to calculate them at times $t - \frac{\Delta t}{2}$ and $t - \frac{3\Delta t}{2}$ in order to compute ζ^* and ζ^{**} (see Eqs. 4.9a–c and 4.10a–c):

$$\zeta^* = \sigma_s^{-1}(z = z_k - c^{*(m)}, H_c, H_t, z_m, b, t - \frac{\Delta t}{2}) \tag{4.11a}$$

$$\zeta^{**} = \sigma_s^{-1}(z = z' - c^{**(m)}, H_c, H_t, z_m, b, t - \frac{3\Delta t}{2}). \tag{4.11b}$$

Therefore the fields of H_c, H_t, z_m, b are calculated at times $t - \frac{\Delta t}{2}$ and $t - \frac{3\Delta t}{2}$ and then bilinearly interpolated at location $\xi i - a^{*(m)}, \eta_j - b^{*(m)}$. This is an additional

complication encountered in ice sheet models whereas in for example ocean models ζ^* would simply be $\sigma^{-1}(z = z_k - c^{*(m)}, t - \frac{\Delta t}{2})$. In addition it is possible that the tracked particle is crossing the CTS and therefore it is necessary to check at each iteration in which domain the particle is. This is done by checking whether the z coordinate is below or above the z_m at the current position ξ and η.

Boundary conditions at the ice–bedrock interface and the ice surface

Basal melting and isostatic adjustment are included in the velocity fields. Hence, no special treatment is required here. On the other hand, the boundary condition at the ice surface is expressed by the surface mass balance. A positive mass balance means that new ice is forming on top of the ice sheet while a negative mass balance means loss of ice. In the case of a positive mass balance the three provenance variables are the current values at that grid point, whereas t_d is the current time and x_d, y_d are the coordinates at the grid point. Since the applied backtracking scheme uses two time levels, it can arise that point C is at a position which was ice free at the last time step. In such a case the backtracking stops and the current value of provenance variable is interpolated from the field $\Psi(t - \Delta t)$.

4.2.5 Deriving the stratigraphy with SICOSTRAT

SICOSTRAT (Simulation COde for STRATigraphy) generates the stratigraphy of $\delta^{18}O$ everywhere within the ice sheet by inversion of Eqs. (4.2) or (4.3) and with the provenance labels as well as the values stored in the depositional archive.

To calculate the $\delta^{18}O$ value with the simple relationship in the form of Eq. (4.2), where $\delta^{18}O$ only depends on the surface temperature, the routine is as follows:

1. Convert z to ζ_s, then use trilinear interpolation to get ξ_d, η_d and t_d.

2. $T_s(x, y, t)$ can be interpolated bilinear in space and linear in time to calculate the surface temperature the particle had when it was deposited on the ice sheet surface.

3. Calculate $\delta^{18}O$ with the transfer function.

This procedure can be used to generate the isotopic stratigraphy of the whole ice sheet which can be written as a netCDF and later be used by an Earth system model. SICOSTRAT uses generic mapping tools (GMTs) to generate plots of ice cores at arbitrary locations and cross sections along grid lines. This makes it

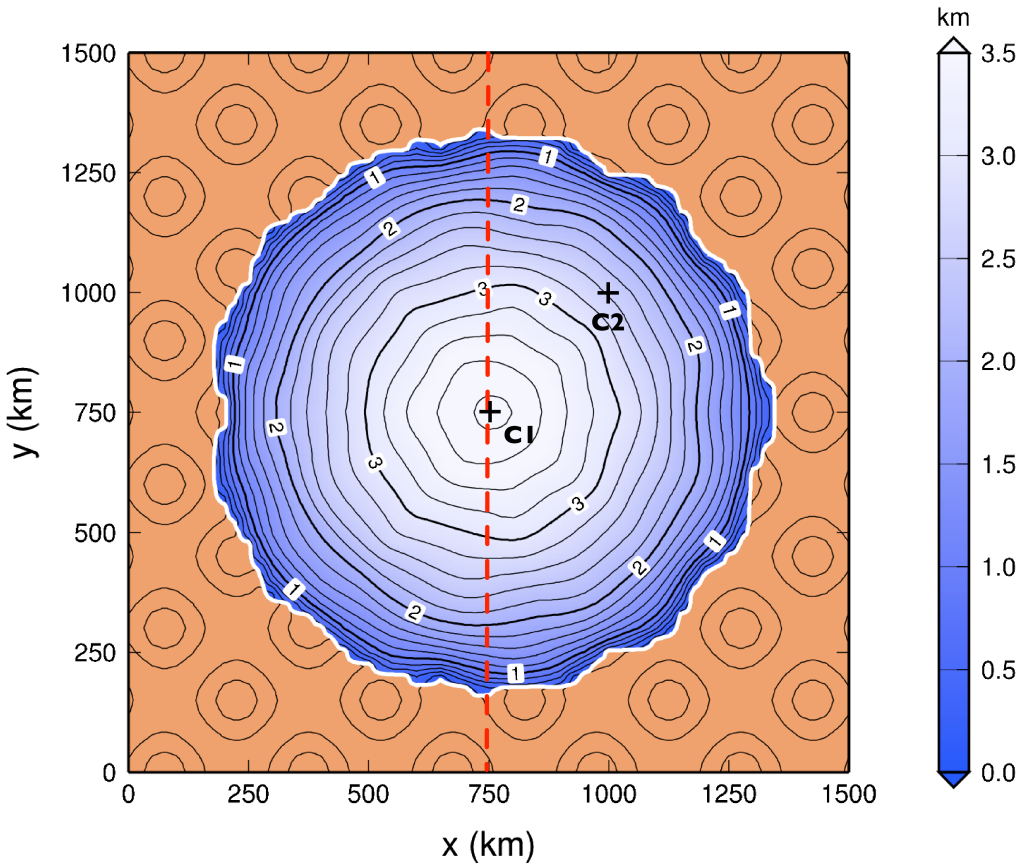**Figure 4.6:** Steady-state surface elevation of the EISMINT experiment K at simulation time 300 kyr. The two crosses mark the core locations C1 and C2, and the dashed red line indicates the cross section. This cross section cuts through the ice centre dome where core C1 is located.

possible to validate the model against ice core data and to get a general overview of the isotopic composition.

4.3 Results

In a first study, the model is applied to the EISMINT inter-comparison project and later to the ice sheets of Greenland and Antarctica.

4.3.1 EISMINT

The EISMINT experiment phase two (Payne et al., 2000) is a simplified geometry experiment with regular boundary conditions to compare thermomechanical ice-sheet models. All boundary conditions are symmetrical and time independent. Twelve experiments were defined and the experiment K is used here to test the transport model SICOTRACE and the post-processing tool SICOSTRAT. In experiment K the bedrock consists of a regular array of 500 m high mounds and with zero ice initial condition.

This EISMINT setup uses a $25 \text{ km} \times 25$ km horizontal grid in the model domain of the size $1500 \text{ km} \times 1500 \text{ km}$ and for the semi-Lagrangian grid we use 100 vertical layers for ζ_s. The time step in the SICOPOLIS simulation was 200 yr. The accumulation/ablation rate is a function of geographical position, which changes its sign in a given distance from the summit (for details see Payne et al., 2000). Figure 4.6 shows the steady-state ice surface at time 300 kyr. In addition, two ice-core locations C1 and C2 as well as one cross section are marked. The core C1 is located at the ice divide ($x = 750$ km, $y = 750$ km) and the results are shown in Fig. 4.11. Core C2 is located at the border of the region with positive mass balance at $x = y = 1000$ km, and the results of the isotope modelling are given in Fig. 4.12.

For the cross section the two depositional coordinates, the depositional age and the resulting δ^{18}O distributions are shown in Figs. 4.7–4.10.

Discussion for EISMINT

The simulated mass transport in the x direction at the cross section is small compared to the one in the y direction, which is expected due to the general ice flow from the centre to the outer regions for the given geometry. This can also be seen in Fig. 4.8 for the depositional provenance of y, changing from central deposition to radial origin.

In Fig. 4.8 the whole ice body is yellow which means that there is little transport perpendicular to the cross section. Inside the ice body the contour lines indicate
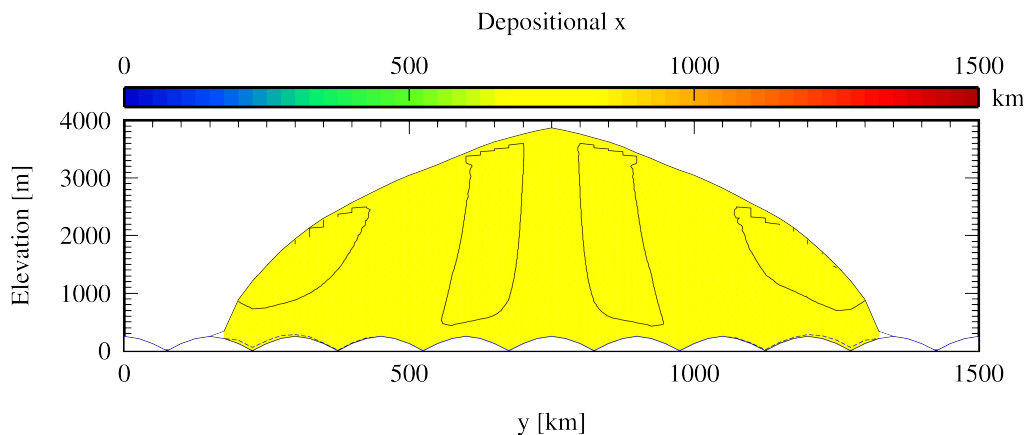
Figure 4.7: Cross section of the depositional provenance of x at time 300 kyr with the mound topography and the dashed contour of the temperate ice thickness H_t. The colour bar indicates the origin of the ice where blue for example means that the ice is coming from the x coordinate of 0 km.
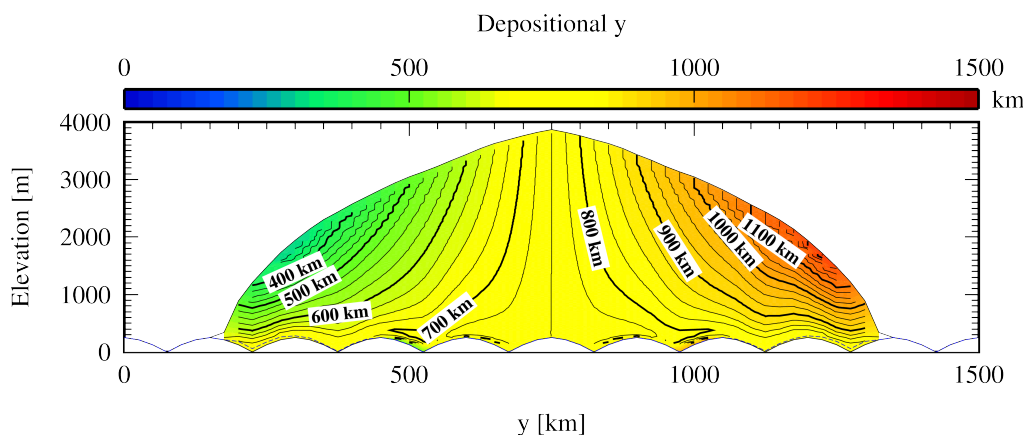
Figure 4.8: Cross section of the depositional provenance of y at time 300 kyr. The same colour coding as in Fig. 4.7 is applied here but for the y coordinate.

the depositional coordinate $x = 750$ km, which is a combination of topographical effect due to the mounts and numerical variations in the order of less than 10 km.

At the area with positive mass balance the oldest ice can be found close to the ice sheet base (Fig. 4.9). This is the ice deposited during the initial phase of the build-up process which remains located there for the whole time. It can also be

Figure 4.9: Age of the ice derived by calculating $t_{\text{final}} - t_{\text{d}}$ where t_{final} is the final time of the simulation. The older ice is located near the base and the majority of the ice is younger than 30 kyr.

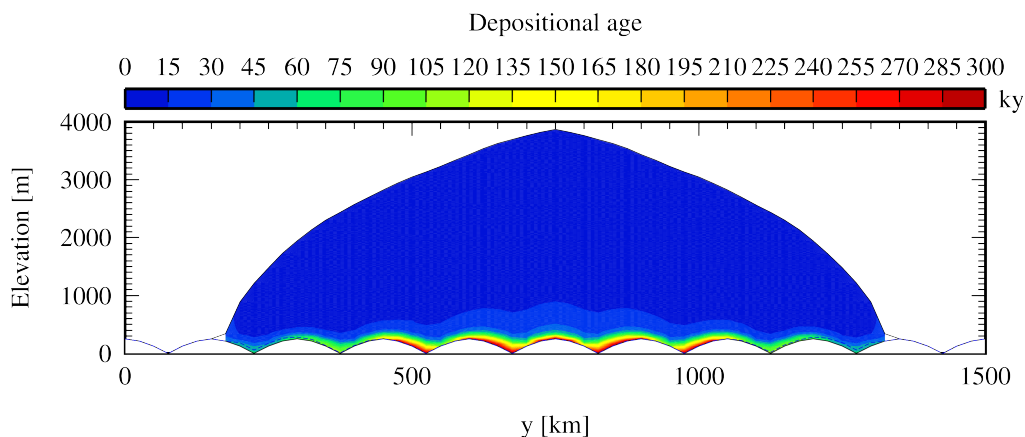seen in Fig. 4.8 where the ice has nearly the same depositional coordinate as the actual coordinate.

Since the surface temperature is constant over time, the $\delta^{18}O$ ratio is only influenced by the depositional coordinates and not by the age. This can be seen in the cross section Fig. 4.10 and the ice cores Figs. 4.11d and 4.12d. Especially in the ice cores, the $\delta^{18}O$ value is a mere combination of the depositional coordinates. This is due to the symmetry of the surface temperature with its lowest value at the centre of the ice sheet. The stepped behaviour of the profile at the upper levels are due to the step size of the vertical ζ_{s} coordinate used for semi-Lagrangian transport and are also influenced by the used time step. This behaviour disappears with shorter time step but for our experiments we chose a longer one in order to save computational time.

Comparison of backtracking schemes

Figure 4.13 illustrates the difference between the first-order backtracking method as used in the papers based on Clarke and Marshall (2002) and the backtracking scheme from de Almeida et al. (2009). The figure is based on the EISMINT experiment with flat topography (experiment A in Payne et al., 2000). We chose the flat topography because the effects of the different backtracking schemes are more obvious with flat ground than with the mound topography. The apparent feature in the figure is that the differences are close to zero in the accumulation
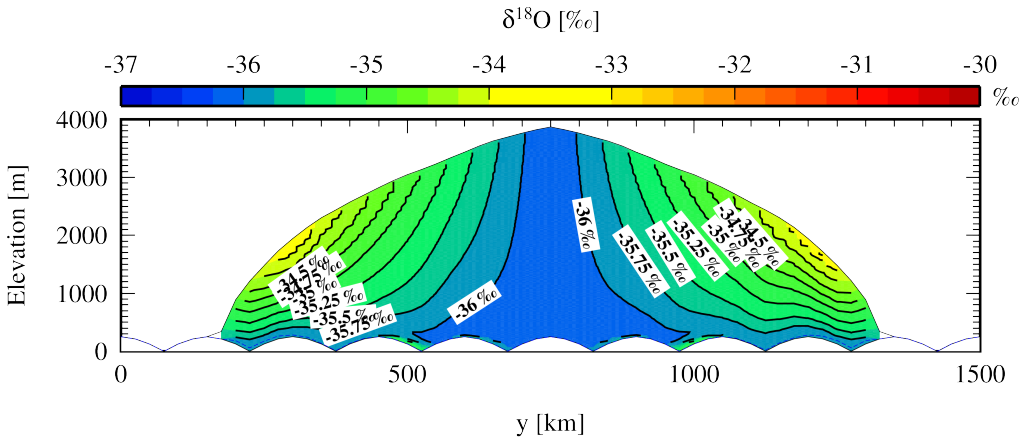
Figure 4.10: The cross section of the resulting δ^{18}O distribution as calculated in SICOS-TRAT. Since the boundary conditions are time independent, the δ^{18}O value is also independent of the ice age and is similar to Fig. 4.8 because the transport perpendicular to the cross section is small.
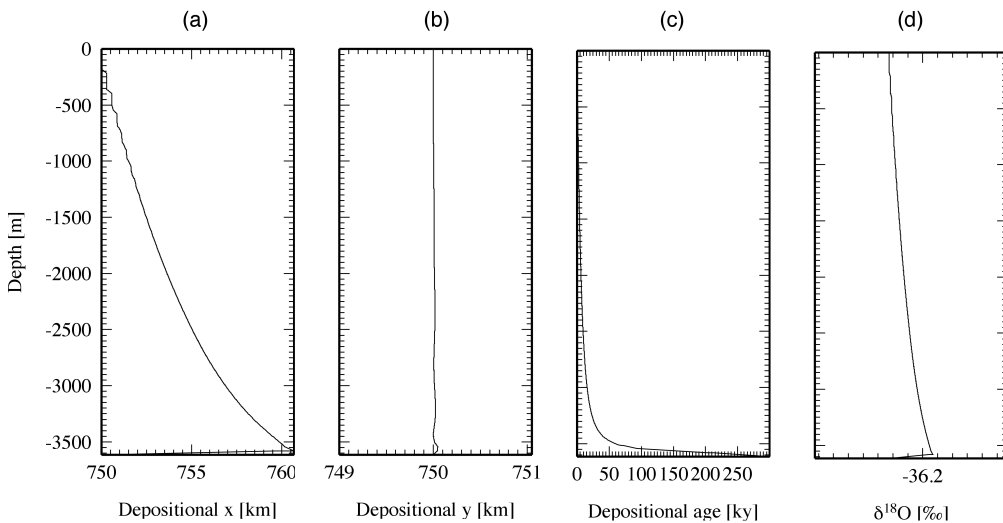
Figure 4.11: Simulated ice core C1 at $x = 750$ km, $y = 750$ km, with **(a)** depositional x (km), **(b)** depositional y (km), **(c)** depositional age (kyr), and **(d)** δ^{18}O value.

zone, which is within a radial distance of 450 km from the summit ($x = y = 750$ km). However in the ablation zone the deviations between the backtracking schemes are substantial. In general the first order scheme calculates older ice in the

Figure 4.12: Simulated ice core C2 at $x = 1000$ km, $y = 1000$ km, same arrangement as in Fig. 4.11.

ablation zone, as can be seen in additional plots in the supplement. While in the previous studies the δ^{18}O value in the ablation zone was of no particular interest, the values close to the margin are crucial in order to close the hydrological cycle.
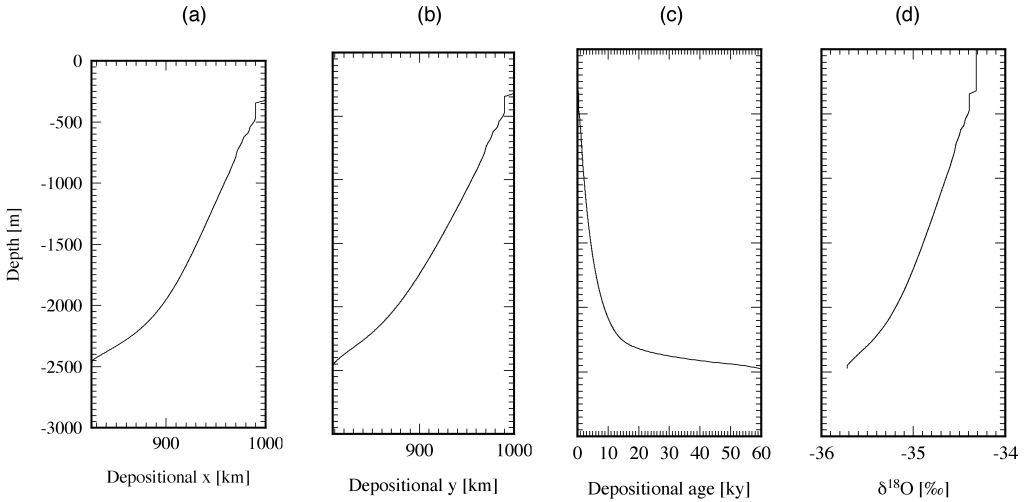
The backtracking scheme from de Almeida et al. (2009) is numerically more expensive than the first-order backtracking, mainly because of the required iterations and interpolations of the de Almeida et al. scheme.

These deviations between the backtracking methods in the ablation zone are likely associated with the greater velocity gradients near the margin. In addition, during ice sheet build-up the velocities vary more in the ablation zone, which is better handled by the two-level time scheme with second-order accuracy. Studies of atmospheric models by Staniforth and Pudykiewicz (1985) and McGregor (1993) found that first-order schemes are inaccurate for large Courant numbers and exhibit poor conservation properties and that a first-order scheme with straight lines and velocities taken at the end point produces an error of 4 % each time step for trajectories in a solid-body rotation problem.

4.3.2 Greenland and Antarctica

In order to apply the isotope transport model to real geometries we present some simulation results of the Greenland and Antarctic ice sheets. Both simulations
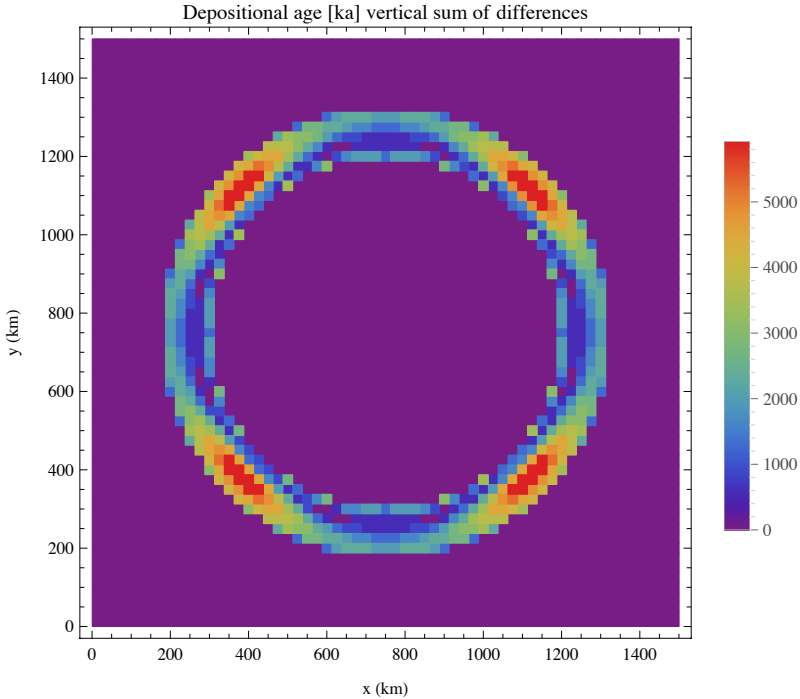
Figure 4.13: Difference of calculated age between first-order and de Almeida et al. (2009) backtracking with the EISMINT experiment A with flat topography. The colours indicate the vertical sum over all layers in the semi-Lagrangian grid of the absolute value of the differences at each grid cell: $\sum_{ks=1}^{ks\,\text{max}} \left| \frac{\text{first order}(ks) - \text{de Almeida et al.}(ks)}{\text{first order}(ks)} \right|$.

start at 422 kyr before the present (pre-industrial at 1950) with no initial ice and relaxed bedrock (in respect to glacio-isostatic adjustment). The horizontal grid is $20\,\text{km} \times 20\,\text{km}$ for Greenland and $40\,\text{km} \times 40\,\text{km}$ for Antarctica. This leads to $83 \times 141 \times 101$ grid points in the semi-Lagrangian grid for Greenland and $141 \times 121 \times 101$ points for Antarctica, respectively. We use 11 levels in the bedrock and temperate ice domain and 81 in the cold ice domain.

A glacial index $gi(t)$ is used to vary the air temperature and precipitation distribution by interpolating between the present and the last glacial maximum (LGM) conditions. This index is defined $gi = 1$ for conditions at the LGM and $gi = 0$ for present conditions (Forsström et al., 2003) and is based on data derived from the $\delta^{18}O$ GRIP ice core record from Greenland and from the δD Vostok ice core record from Antarctica (Dansgaard et al., 1993; Johnsen et al., 1995; Petit et al.,

1999). For the first 100 kyr BP the GRIP record is used and prior to that the Vostok ice core. This is necessary since the GRIP record is believed to be corrupted due to ice-flow irregularities (Greve, 2005). In total, the glacial index reaches 422 kyr back in time.

With these settings the total computational time including the semi-Lagrangian transport and writing of the depositional archive on one core of a 2.8 GHz dual-core AMD Opteron was 141.3 h for Antarctica and 214.7 h for Greenland.

As boundary condition and forcing function, a linear isotope transfer function is used:

$$\delta^{18}O = a \cdot T_s + b \tag{4.12}$$

with $a = 0.80\,‰\,(°C)^{-1}$ and $b = -8.11\,‰$ for Antarctica (Masson-Delmotte et al., 2008) and with $a = 0.327\,‰\,(°C)^{-1}$ and $b = -24.8\,‰$ for Greenland (Cuffey and Clow, 1997), respectively.
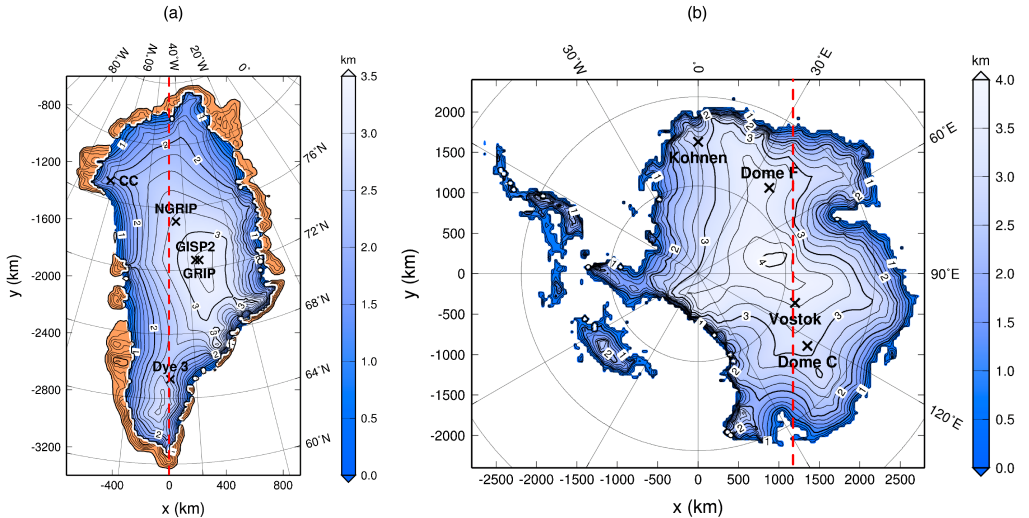
Figure 4.14: Simulated present-day surface topography with 200 m contours of elevation in km a.s.l. Major ice core locations are marked with crosses and the location of the cross sections are marked with a red dashed line. **(a)** Greenland and **(b)** Antarctica, without the ice shelves because SICOPOLIS 2.9 does not include ice shelf dynamics.

As an example of a simulated Greenland ice core the GRIP core is shown in Fig. 4.15a which is located in the central region of the Greenland Ice Sheet (see Fig. 4.14a for its location). For Antarctica the Vostok Station has been chosen, which is located in central East Antarctic Ice Sheet (see Fig. 4.14b). The modelled
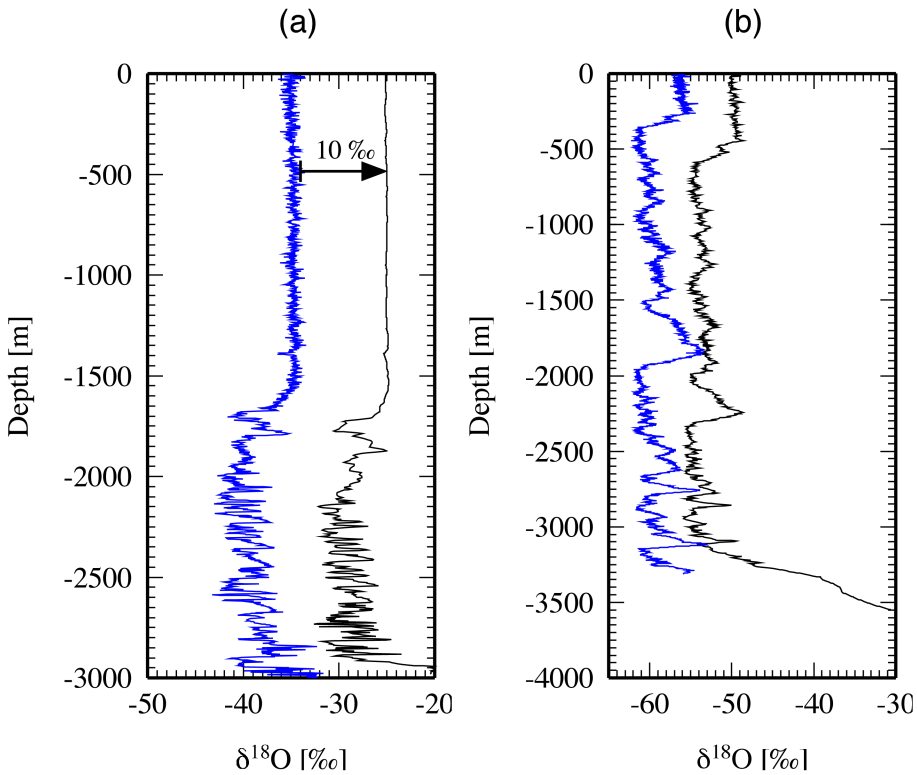
Figure 4.15: Comparison of modelled δ^{18}O values in black and observed values in blue. The modelled data in the GRIP core **(a)** have an offset of 10 per mille to the right in order to make the comparison more easy to read. The vertical axis is the ice core depth and level 0 is defined as the ice surface in both, measured and modelled ice core. For the GRIP core **(a)** the modelled depth is 2945 compared to observed 3029 m with reliable δ^{18}O data until 2983.2 m, and for the Vostok core **(b)** the modelled depth is 3549 m compared to 3623 m in reality and data are available until 3310 m.

δ^{18}O depth profiles are compared to observational data by Johnsen et al. (1997) for the GRIP ice core and by Petit et al. (1999) for the Vostok ice core. Since there is a difference between the modelled and the observed ice thickness we defined level 0 to be the modelled height of the real ice surface.

Figure 4.16a shows two cross sections through the (a) Greenland and (b) Antarctic ice sheets and the vertical δ^{18}O distribution close to the chosen ice-core locations. The Antarctic cross section reveals a broader range of δ^{18}O variation

with more depleted values than the Greenland cross section. Hence, the colour bars are chosen differently.

Discussion for Greenland and Antarctica

The comparison between the simulated cores and observational data shows in general a good agreement of the isotope records. Taking into consideration that the core data stems from a single ice core with high vertical and horizontal resolution (on the cm scale) and the simulated core is based on $20 \text{ km} \times 20 \text{ km}$ and $40 \text{ km} \times 40 \text{ km}$ model simulations for Greenland and Antarctica, respectively, the overall coincidence is satisfying. Looking into more detail, however, the observational data shows more high-frequency variability and a shift in the main signals for the Antarctic record (Fig. 4.15). There are several reasons which need to be discussed when comparing the records.

Firstly, the ice dynamic model SICOPOLIS was taken as a given tool and no effort was made to tune the model for the present day. This was beyond the scope of the study and we used the standard setting here. As a second argument, the isotope boundary condition comes into play which is taken from transfer functions and is, therefore, not a correct local function. While this works properly for Greenland, a mismatch for the Vostok location of about 8 per mille can be found between observations and model results. Third, the time step for the Greenland simulation is five years and for Antarctica is ten years while the measurements resolve the seasonal scale. In addition, the glacial index of the surface temperature forcing is also smoothed to 100 yr so the small-scale variations cannot be resolved.

On the other hand, the overall variability of $\delta^{18}O$ is comparable with the measurements, while the absolute position of the spikes is also influenced by the difference of the ice thickness. In the cross section for the Greenland Ice Sheet the sequences of values between −40 per mille (green) and −35 per mille (yellow) indicates the different glacial–interglacial cycles of the past, also seen in the lower section of the GRIP ice core. The profile is just a cross section near the GRIP location but SICOSTRAT generates a complete netCDF output of the whole three-dimensional isotope field.

For the Vostok ice core (Fig. 4.15b) the modelled values show the same variations as the measurements but the values are generally higher and the features are up to 500 m deeper than in the measurements. Here, the ice dynamics need to be adjusted and more care has to be given to the ice dynamic model performance. The very low accumulation rates in central East Antarctica are challenging to the ice dynamics and lead to too low signals in the simulation (e.g. at 2000 m depth).

In addition, the $40\,\mathrm{km}$ grid does not resolve details in the bedrock topography, which has a strong influence on the stratigraphy of the Vostok ice core (Parrenin et al., 2004).
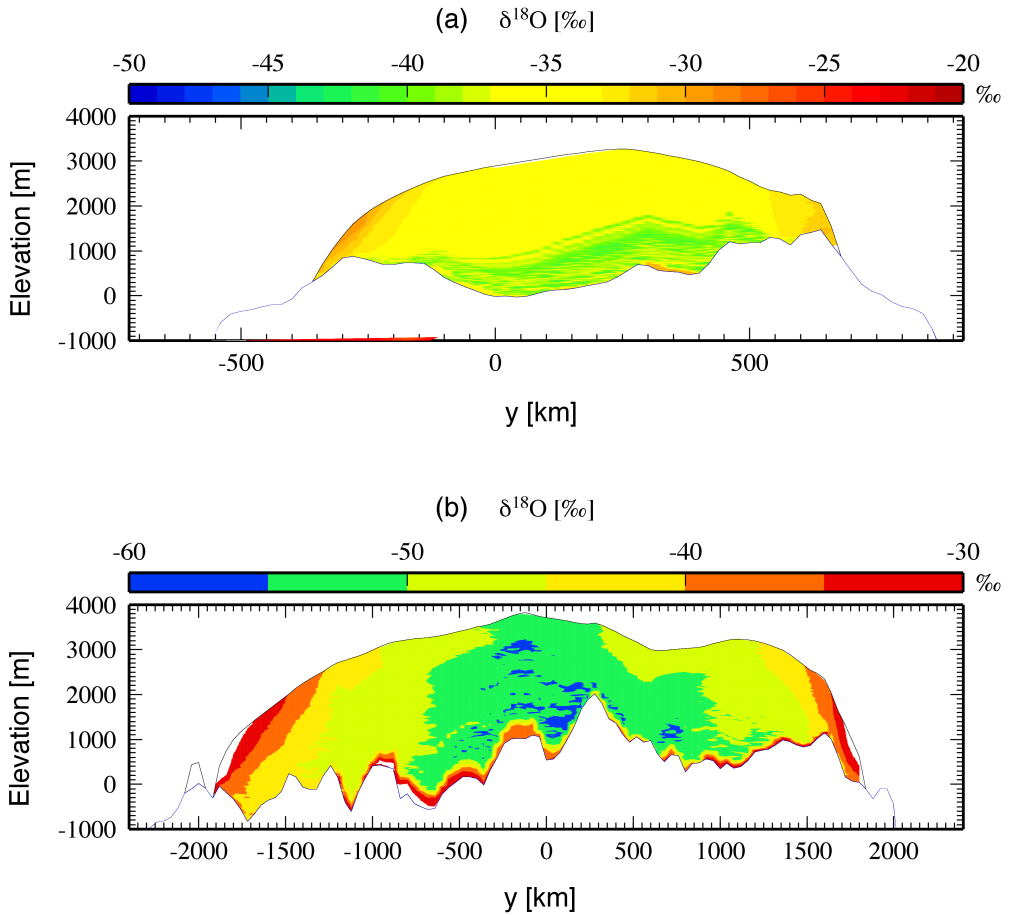

Figure 4.16: Two cross sections of the **(a)** Greenland and **(b)** Antarctic ice sheets showing the δ^{18}O distribution close to the GRIP and Vostok ice cores.

4.4 Conclusions

In this paper, an oxygen isotope transport model for polythermal ice sheets has been presented, which makes it possible to study the oxygen isotope ratio inside polythermal ice sheets where the shallow ice approximation is valid. The model was applied to the EISMINT inter-comparison phase 2 project and applied to the Greenland and Antarctic ice sheets. As an example, one simulated ice core of each ice sheet has been compared to measured ice core data. The model has been developed to tackle two goals – firstly, to use local comparison of vertical profiles at drill core sites to validate and improve the ice sheet model, and secondly, to close the oxygen isotopic budget in the hydrological cycle of a fully coupled Earth system model approach, when coupling the ice model to an atmosphere–ocean–land surface general circulation model (e.g. Werner et al., 2011; Xu et al., 2012).

In our study the backtracking scheme from de Almeida et al. (2009) with second-order accuracy is used which requires the three-dimensional velocity fields to be interpolated on intermediate steps. The sigma coordinate formulation of the ice sheet model make it necessary to evaluate and interpolate ice topography variables in space and time. This adds to the computational costs and overall complexity of the approach.

If the focus of a study with semi-Lagrangian transport is on ice core locations in the ice sheet interior a first-order backtracking may be sufficiently accurate, with the additional benefit of lower computational lost. Otherwise, if the values of the transported property near the margin are of interest, a second-order backtracking scheme such as the one of de Almeida et al. (2009) may be better suited for the task. We will address the comparison between different semi-Lagrangian schemes as well as Lagrangian and Eulerian methods focusing on values near the margin in a subsequent paper.

The indirect semi-Lagrangian approach with provenance transport and three different programs has some advantages and disadvantages.

The advantages are that transfer function between surface temperature and $\delta^{18}O$ can be changed without the need of re-running the whole simulation again. This is important for long-term simulation since SICOPOLIS and SICOTRACE are computationally expensive and, therefore, it allows to experiment with different transfer functions. The transfer function for $\delta^{18}O$ could also include local changes of surface elevation and changes in mean surface temperature (Cuffey, 2000; Langebroek et al., 2010). A downside of the three different programs is that

SICOTRACE needs the three-dimensional velocity field in the cold and temperate ice domain and information about the ice topography for each time step. For high resolution and simulations on palaeo-timescales this leads to a high amount of data which could be of the order of terabytes. Since the information of the velocity field and the whole history of the ice sheet evolution is in general of no interest, the data can be deleted after SICOTRACE has performed the transport calculation. For paleo-runs, a shell script subsequently runs SICOPOLIS and SICOTRACE to generate a depositional archive and provenance archive for the whole time period for SICOSTRAT. This leads to a further complication of file handling and an additional layer of complexity in the whole workflow.

The semi-Lagrangian transport can be used for other species, such as deuterium, but if the species involve some feedback with the ice dynamics, then the approach of three different programs is not feasible because of all the overhead with file transfer and initialisation of programs only to run for one time step.

This chosen approach is in any case an important step in the direction of fully coupled Earth System Models for investigating the climate system and comparing model output and in situ measurements. It is also the basis for studies involving the transport of passive tracers.

Code availability

ISOPOLIS is based on SICOPOLIS Version 2.9 (`http://www.sicopolis.net`) with the new modules SICOTRACE and SICOSTRAT. All components are written in Fortran 90 and ISOPOLIS consists of 35 700 lines of documented code (21 750 of pure code). The code runs on Unix-based platforms and is automatically handled by Makefile options and parameter files. To distribute, maintain, develop and share ISOPOLIS among different users we use the distributed revision control system `http://aforge.awi.de`, providing project hosting, version control, bug-tracking, and messaging. The established netCDF-output (UNIDATA, 2016) format of ISOPOLIS ensures that the computed results can subsequently be post-processed with the desired software packages (e.g. GMT scripts by Wessel and Smith, 1998). In addition the netCDF operators NCO (`http://nco.sourceforge.net/`) are required to run ISOPOLIS.

The Supplement related to this article is available online at doi:10.5194/gmd-7-1395-2014-supplement

Acknowledgements

Chapter 5

Conclusions and future perspectives

5.1 Conclusions

Article I introduced the model components of impurity melt-out and accumulation, ice albedo and SMB. The model was calibrated and evaluated with data from the K-transect in western Greenland. In addition to introducing and calibrating the model, some valuable information was derived. The daily runoff of impurities is in the order of one per mille, which corresponds to a residence time of decades. Secondly, dust melt-out is the main source of impurities, and direct atmospheric deposition of dust plays a minor role. For BC, atmospheric deposition is equally as important as melt-out (see Figure 2.15).

The model in Article I accurately captured the net shortwave radiation, even with the simple parameterisation of temperature and precipitation (see Figure 2.11). If the turbulent heat flux and longwave radiation are calculated and not empirically based, the surface energy balance, and therefore the SMB, should improve. Currently, the simplified energy balance of Robinson et al. (2010) uses empirical turbulent heat flux and longwave radiation. The model framework developed here could be used together with an atmospheric component which delivers both the turbulent heat flux and longwave radiation. Therefore, it is promising that the model of Article I delivered accurate predictions of net shortwave radiation.

Article II applied the whole framework to a simplified geometry with similar conditions to the GrIS. The results underlined the non-linearity of the whole system, which is partially caused by the effect of BC on albedo and positive feedback between melt and impurity accumulation. The effect of impurities on ice albedo

117

and, ultimately, ice sheet volume is pronounced under a warmer climate. This result emphasises the relevance of ice albedo and impurities for projections of sea level rise. The large amount of englacial impurities needs to be taken into account, especially in multi-millennia time-scale simulations. The additional ice volume loss with RCP8.5 in the year 3000 was 7% when impurity accumulation and melt-out were included. This loss was estimated to be lower due to the chosen temperature evolution (based on a global average with no warming after 2300). In addition, snow albedo was considered unaffected by impurities, and the albedo feedback to temperature and other feedbacks were not included. Overall, Article II was not meant to deliver an accurate prediction of future sea level rise but to underline the non-linearity and motivate further research in processes linked to ice albedo. Some suggestions for which can be found in the next section.

Article III introduced the transport of a passive tracer in the polythermal ice sheet model SICOPOLIS. A second-order backtracking scheme was used for the first time in an ice sheet model. Comparison to a first-order scheme showed a computed age deviation in the ablation zone but almost no difference in the ice sheet interior. Closing the global cycle of water isotopes and impurity melt-out depends on the accuracy of the age of the ice in the ablation zone. Due to the irregularity of BC, dust and δ^{18}O time series, an error of a few years could result in a substantial error of the derived property; therefore, the second-order scheme seems to be the better choice. Further investigation is needed, however, to quantify the error of the first-order scheme to justify the additional complexity and computational cost of the second-order scheme.

The model framework, as introduced in Articles I and II, can be adapted for any ice sheet or glacier and thereby improve the albedo schemes of glaciers and ice sheets as well as the cryospheric components of Earth system models and regional climate models. Article II should motivate further research into ice albedo and the use and development of dynamic ice albedo models. Articles I and II also showed the multiple benefits of reducing BC emissions. The glaciers benefit in multiple ways from such a reduction: first, by reducing the forcing effect of BC; second, by reducing the atmospheric deposition of BC on snow and ice and third, by the delayed benefit of having less englacial BC.

5.2 Future improvements of the model

This section will discuss improvements of the model components, then provide general recommendations for future research linked to ice albedo and impurities.

Each component of the model framework can be improved (Figure 1.5), starting with the ice dynamics. The shallow ice approximation can be violated at locations with steep slopes, which can cause incorrect velocities. The velocities are required to calculate the timing of impurity melt-out, which also depends on the geometry and accuracy of the tracer transport scheme. A possible solution would be to use a full Stokes ice-dynamics model such as Elmer/Ice (Gagliardini et al., 2013). However, a full Stokes model has a much higher computational cost compared to models with shallow ice approximation (e.g. Ahlkrona et al., 2016). Therefore, alternatively, the new hybrid shallow-ice-shelfy-stream method of SICOPOLIS (Bernales et al., 2016) or a hybrid model of shallow ice and full Stokes (Ahlkrona et al., 2016) could be used. The full Stokes equations could be used only when needed and the much faster shallow ice approximation elsewhere. Another advantage of a finite element model such as Elmer/Ice is that a finer mesh can be used in the ablation zone. These improvements of the ice dynamics component should result in a more accurate model.

Independent of which equations are used, shallow ice or full Stokes, the spin-up needs to match the current margin, and the age of the ice needs to match the observations as closely as possible. The recent dataset of MacGregor et al. (2015) could be very valuable in achieving that correlation.

The next aspect of the framework is the tracer transport. The ages in the ablation zone depend on the backtracking scheme. First, the magnitude of these deviations needs to be quantified and investigated further. This evaluation can be obtained by comparing different models with high resolution in space and time, as no analytical solution for age near the margin exists.

The second-order backtracking scheme of Article III has higher computational costs than the first-order scheme. One way to save computational time would be to use the second-order scheme only when necessary. The SMB of the previous time-step may be used to decide which scheme to use.

Article III's backtracking scheme is complicated to implement and maintain due to the two steps and changing geometry of the domain. Therefore, another second-order scheme such as SETTLS (Stable Extrapolation Two-Time-Level Scheme) (Hortal, 2002) might be better suited for the task as it only requires one backward step. In addition, the two SICOPOLIS domains of temperate and cold ice increase the complexity. This complexity is no longer the case with the new enthalpy methods implemented in SICOPOLIS (Greve and Blatter, 2016).

The accuracy of the transport scheme also depends on the interpolation methods; therefore, a tricubic interpolation scheme (Lekien and Marsden, 2005) and/or

"balance-based" interpolation scheme of Lhomme et al. (2005a) is expected to improve the accuracy of the age and englacial impurity concentration.

The split between the transport module SICOTRACE and SICOPOLIS is not practical in the context of the whole model framework. The tracer transport needs to update the age field at least once annually in order to allow feedback between impurity melt-out and the SMB. With the setup described in Article III, this feedback would take too much time caused by file-transfer. This delay is not the case when all the components of the model framework are integrated into SICOPOLIS. This technical improvement reduces the computational time substantially and is viewed as a requirement to study the GrIS with the model framework.

The next component to discuss is the aerosol input. There is still a lack of Holocene dust data. Only the GISP2 core includes Holocene data of the dust proxy calcium but no direct measurements of particle concentrations. Data from the NEEM ice core are still not available but should include Holocene dust records. Holocene concentrations of dust are low but still important because currently a large fraction of the ice at the margin is of Holocene origin. Also, the current rate of dust deposition needs to be better constrained, especially near the margin where local dust could be the main source. Similarly, BC data going further back in time is required and will hopefully also be delivered by the NEEM ice core.

Impurity accumulation needs further testing and comparison to field data. These data require impurity sampling close to an AWS; some suggestions for field observations are given in the next section.

Impurity accumulation in the snowpack was only included to simulate deposition of snow impurities onto the ice surface. The snowpack model needs to be improved in order to correctly account for accumulation on the snow surface. Gabbi et al. (2015) carried out an almost complementary study to Article I, focusing on the snowpack alone. They used the same albedo scheme of Gardner and Sharp (2010) and a multi-layer snowpack model which accounts for snow grain growth and snow densification. Therefore, combining Article I with their methods would encompass the whole accumulation process. This combination would improve the SMB and simulation of the surface albedo when snow is present. It would also eliminate the free parameter of wet snow albedo in Article I. The addition of a more detailed snowpack and snow albedo model, however, will also introduce additional complexity and increase the number of required inputs.

The next component is the ice albedo parameterisation. A parameterisation which directly accounts for impurities *on* the surface would eliminate the need for the effective depth described in Article I.

The final component is the SMB model itself. Articles I and II use a simplified energy balance to compute melt. Although the SMB model has previously been applied to the whole GrIS (Robinson et al., 2010, 2011), additional testing is recommended. Article I suggested an alternative transmissivity parameterisation that needs to be further tested for conditions over the whole GrIS. Also, the parameterisation of temperature and precipitation discussed in Article I needs to be optimised for the whole GrIS.

The next logical step is to combine everything and apply the model framework to the GrIS in 3D. The main tools are developed, but there are still some topics left to investigate and methods to be developed before a full study of the GrIS can be achieved.

Articles I, II and III were all conducted with stand-alone ice sheet models. The whole model framework could also be coupled with regional climate models and a model of aerosol transport (e.g. Skeie et al., 2011). This coupling would allow for a dynamic model of BC and dust deposition. Regional climate models would also reduce the need for cloud parameterisation and, most importantly, temperature and precipitation. The snowpack component would particularly benefit from daily values. Boundary conditions provided by regional climate models would also allow the effects of summer snowfall and possible cleaning of the ice surface by heavy rain events to be included.

5.3 Recommendations for future research

The ice surface itself needs further study, with a focus on the dynamics of cryoconite. This need includes studies of cryoconite hole formation and collapse and biological activity. Time-lapse cameras on AWS would improve the understanding of surface processes and cryoconite hole dynamics. All this data would allow a more accurate prediction of ice albedo in the future with a physically-based cryoconite distribution model.

The albedo scheme of Gardner and Sharp (2010) relies on the specific surface area of ice, for which few measurements exist. The specific surface area should be measured in the ablation zone all over Greenland. This measurement would require drilling shallow ice cores, some of which should be close to an AWS. In addition to the specific surface area of ice, these shallow cores should be analysed for ice crystal size, englacial impurity concentration and age. These measurements could be used to derive a more physically-based ice albedo model.

The next topic is impurities. Sampling the surface impurity close to AWS sites and reporting the results in units of mass per square metre is recommended. Then, the content and proportion should be analysed to determine how much of the impurity mass is dust, BC (reported as rBC, EC, EBC), brown carbon (from microbes and/or distant sources) and possibly other species. Ideally, the measurement methods would be standardised, allowing the contribution of each species to the total mass and variability of the impurity species percentage to be identified.

The impurity species should be understood as classes of different materials, with a variety of optical properties. For example, is the absorption of dust found at the K-transect comparable to dust found in northeast Greenland? Detailed knowledge about the distribution of impurity species could be used to derive a more physically-based ice albedo model which includes several impurity species and their optical properties.

Biological activity, which influences the albedo of ice and snow directly and indirectly, is still largely unknown. The effect of microbes on ice albedo is probably significant but still needs quantification. For example, how much light-absorbing material is produced and how is the productivity influenced by environmental parameters?

The high spatial variability of ice albedo needs to be considered. Albedo values can vary from 0.2 to 0.7 over a short distance. What is the representative ice albedo value of a grid cell as large as a few square km? Unmanned aerial vehicle campaigns could link small scale observations to larger scale ice sheet models and satellite remote sensing.

References

Abbott, P. M. and Davies, S. M.: Volcanism and the Greenland ice-cores: the tephra record, Earth-Science Reviews, 115, 173–191, doi:10.1016/j.earscirev.2012.09.001, 2012.

Adhikary, S., Nakawo, M., Seko, K., and Shakya, B.: Dust influence on the melting process of glacier ice: experimental results from Lirung Glacier, Nepal Himalayas, IAHS Publication, doi:10.1002/esp.3352, 2000.

Ahlkrona, J., Kirchner, N., and Lötstedt, P.: A numerical study of scaling relations for non-newtonian thin-film flows with applications in ice sheet modelling, The Quarterly Journal of Mechanics and Applied Mathematics, 66, 417–435, doi:10.1093/qjmam/hbt009, 2013.

Ahlkrona, J., Lötstedt, P., Kirchner, N., and Zwinger, T.: Dynamically coupling the non-linear Stokes equations with the shallow ice approximation in glaciology: Description and first applications of the ISCAL method, Journal of Computational Physics, 308, 1–19, doi:10.1016/j.jcp.2015.12.025, 2016.

Albani, S., Mahowald, N. M., Winckler, G., Anderson, R. F., Bradtmiller, L. I., Delmonte, B., François, R., Goman, M., Heavens, N. G., Hesse, P. P., Hovan, S. A., Kang, S. G., Kohfeld, K. E., Lu, H., Maggi, V., Mason, J. A., Mayewski, P. A., McGee, D., Miao, X., Otto-Bliesner, B. L., Perry, A. T., Pourmand, A., Roberts, H. M., Rosenbloom, N., Stevens, T., and Sun, J.: Twelve thousand years of dust: the Holocene global dust cycle constrained by natural archives, Climate of the Past, 11, 869–903, doi:10.5194/cp-11-869-2015, 2015.

Andreae, M. O. and Gelencsér, A.: Black carbon or brown carbon? The nature of light-absorbing carbonaceous aerosols, Atmospheric Chemistry and Physics, 6, 3131–3148, doi:10.5194/acp-6-3131-2006, 2006.

Arakawa, A.: Computational Design for Long-Term Numerical Integration of the Equations of Fluid Motion: Two-Dimensional Incompressible Flow. Part I, Journal of Computational Physics, 135, 103–114, doi:10.1006/jcph.1997.5697, 1997.

REFERENCES

ASTM International: Tables for Reference Solar Spectral Irradiances: Direct Normal and Hemispherical on 37° Tilted Surface, ASTM International, doi:10.1520/G0173-03R12, 2012.

Bales, R. C., Guo, Q., Shen, D., McConnell, J. R., Du, G., Burkhart, J. F., Spikes, V. B., Hanna, E., and Cappelen, J.: Annual accumulation for Greenland updated using ice core data developed during 2000–2006 and analysis of daily coastal meteorological data, Journal of Geophysical Research, 114, D06 116, doi:10.1029/2008JD011208, 2009.

Bamber, J. L., Griggs, J. A., Hurkmans, R. T. W. L., Dowdeswell, J. A., Gogineni, S. P., Howat, I., Mouginot, J., Paden, J., Palmer, S., Rignot, E., and Steinhage, D.: A new bed elevation dataset for Greenland, The Cryosphere, 7, 499–510, doi:10.5194/tc-7-499-2013, 2013.

Bauer, S. E., Bausch, A., Nazarenko, L., Tsigaridis, K., Xu, B., Edwards, R., Bisiaux, M., and McConnell, J.: Historical and future black carbon deposition on the three ice caps: Ice core measurements and model simulations from 1850 to 2100, Journal of Geophysical Research: Atmospheres, 118, 7948–7961, doi:10.1002/jgrd.50612, 2013.

Behrens, J.: Adaptive semi-Lagrangian finite element method for the solution of the shallow water equations: Implementation and parallelization, Berichte zur Polarforschung, 217, 167, 1996.

Bernales, J., Rogozhina, I., Greve, R., and Thomas, M.: Comparison of different hybrid schemes for the combination of Shallow Approximations in numerical simulations of the Antarctic Ice Sheet, The Cryosphere, submitted, 2016.

Bigler, M.: New aerosol measurements from the Greenland NEEM ice core, in: EGU General Assembly Conference Abstracts, Vienna, 2012.

Biscaye, P. E., Grousset, F. E., Revel, M., van der Gaast, S., Zielinski, G. A., Vaars, A., and Kukla, G.: Asian provenance of glacial dust (stage 2) in the Greenland Ice Sheet Project 2 Ice Core, Summit, Greenland, Journal of Geophysical Research: Oceans, 102, 26 765–26 781, doi:10.1029/97JC01249, 1997.

Bogdal, C., Nikolic, D., Lüthi, M. P., Schenker, U., Scheringer, M., and Hungerbühler, K.: Release of Legacy Pollutants from Melting Glaciers: Model Evidence and Conceptual Understanding, Environmental Science & Technology, 44, 4063–4069, doi:10.1021/es903007h, 2010.

Bøggild, C. E., Winther, J.-G., Sand, K., and Elvehøy, H.: Sub-surface melting in blue-ice fields in Dronning Maud Land, Antarctica: observations and modelling, Annals of Glaciology, 21, 162–168, 1995.

Bøggild, C. E., Oerter, H., and Tukiainen, T.: Increased ablation of Wisconsin ice in eastern north Greenland: observations and modelling, Annals of Glaciology, 23, 144–148, doi:10.3198/1996AoG23-144-148, 1996.

Bøggild, C. E., Brandt, R. E., Brown, K. J., and Warren, S. G.: The ablation zone in northeast Greenland: ice types, albedos and impurities, Journal of Glaciology, 56, 101–113, doi:10.3189/002214310791190776, 2010.

Bond, T. C. and Bergstrom, R. W.: Light absorption by carbonaceous particles: An investigative review, Aerosol Science and Technology, 40, 27–67, doi:10.1080/02786820500421521, 2006.

Bond, T. C., Doherty, S. J., Fahey, D. W., Forster, P. M., Berntsen, T., DeAngelo, B. J., Flanner, M. G., Ghan, S., Kaercher, B., Koch, D., Kinne, S., Kondo, Y., Quinn, P. K., Sarofim, M. C., Schultz, M. G., Schulz, M., Venkataraman, C., Zhang, H., Zhang, S., Bellouin, N., Guttikunda, S. K., Hopke, P. K., Jacobson, M. Z., Kaiser, J. W., Klimont, Z., Lohmann, U., Schwarz, J. P., Shindell, D., Storelvmo, T., Warren, S. G., and Zender, C. S.: Bounding the role of black carbon in the climate system: A scientific assessment, Journal of Geophysical Research: Atmospheres, 118, 5380–5552, doi:10.1002/jgrd.50171, 2013.

Bory, A., Biscaye, P., Piotrowski, A., and Steffensen, J. P.: Regional variability of ice core dust composition and provenance in Greenland, Geochemistry Geophysics Geosystems, 4, 1107, doi:10.1029/2003GC000627, 2003.

Bougamont, M., Bamber, J. L., and Greuell, W.: A surface mass balance model for the Greenland Ice Sheet, Journal of Geophysical Research, 110, F04 018, doi:10.1029/2005JF000348, 2005.

Box, J. E., Bromwich, D., Veenhuis, B. A., Bai, L. S., Stroeve, J. C., Rogers, J. C., Steffen, K., Haran, T., and Wang, S.-H.: Greenland Ice Sheet Surface Mass Balance Variability (1988-2004) from Calibrated Polar MM5 Output, Journal of Climate, 19, 2783–2800, doi:10.1175/JCLI3738.1, 2006.

Box, J. E., Fettweis, X., Stroeve, J. C., Tedesco, M., Hall, D. K., and Steffen, K.: Greenland ice sheet albedo feedback: thermodynamics and atmospheric drivers, The Cryosphere, 6, 821–839, doi:10.5194/tc-6-821-2012, 2012.

Brock, B. W., Willis, I. C., and Sharp, M. J.: Measurement and parameterization of aerodynamic roughness length variations at Haut Glacier d'Arolla, Switzerland, Journal of Glaciology, 52, 281–297, doi:10.3189/172756506781828746, 2006.

Brutel-Vuilmet, C., Menegoz, M., and Krinner, G.: An analysis of present and future seasonal Northern Hemisphere land snow cover simulated by CMIP5 coupled climate models, The Cryosphere, 7, 67–80, doi:10.5194/tc-7-67-2013, 2013.

Burgess, E. W., Forster, R. R., Box, J. E., Mosley-Thompson, E., Bromwich, D. H., Bales, R. C., and Smith, L. C.: A spatially calibrated model of annual accumulation rate on the Greenland Ice Sheet (1958–2007), Journal of Geophysical Research, 115, F02 004, doi:10.1029/2009JF001293, 2010.

Calanca, P., Gilgen, H., Ekholm, S., and Ohmura, A.: Gridded temperature and accumulation distributions for Greenland for use in cryospheric models, Annals of Glaciology, 31, 118–120, doi:10.3189/172756400781820345, 2000.

Carmagnola, C. M., Domine, F., Dumont, M., Wright, P., Strellis, B., Bergin, M., Dibb, J., Picard, G., Libois, Q., Arnaud, L., and Morin, S.: Snow spectral albedo at Summit, Greenland: measurements and numerical simulations based on physical and chemical properties of the snowpack, The Cryosphere, 7, 1139–1160, doi:10.5194/tc-7-1139-2013, 2013.

Castello, J. D., Rogers, S. O., Starmer, W. T., Catranis, C. M., Ma, L., Bachand, G. D., Zhao, Y., and Smith, J. E.: Detection of tomato mosaic tobamovirus RNA in ancient glacial ice, Polar Biology, 22, 207–212, doi:10.1007/s003000050411, 1999.

Chalmas, R.: Analysis of the volcanic signal in the NGRIP ice core during the ice age, Master's thesis, University of Copenhagen, Copenhagen, 2004.

Chandler, D. M., Alcock, J. D., Wadham, J. L., Mackie, S. L., and Telling, J.: Seasonal changes of ice surface characteristics and productivity in the ablation zone of the Greenland Ice Sheet, The Cryosphere, 9, 487–504, doi:10.5194/tc-9-487-2015, 2015.

Chýlek, P., Srivastava, V., Cahenzli, L., Pinnick, R. G., Dod, R. L., Novakov, T., Cook, T. L., and Hinds, B. D.: Aerosol and graphitic carbon content of snow, Journal of Geophysical Research: Atmospheres, 92, 9801–9809, doi:10.1029/JD092iD08p09801, 1987.

Chýlek, P., Johnson, B., and Wu, H.: Black Carbon Concentration in a Greenland Dye-3 Ice Core, Geophysical Research Letters, 19, 1951–1953, doi:10.1029/92GL01904, 1992.

Chýlek, P., Johnson, B., Damiano, P. A., Taylor, K. C., and Clement, P.: Biomass burning record and black carbon in the GISP2 ice core, Geophysical Research Letters, 22, 89–92, doi:doi:10.1029/94GL02841, 1995.

Clarke, A. D. and Noone, K. J.: Soot in the arctic snowpack: a cause for perturbations in radiative transfer, Atmospheric Environment, 19, 2045–2053, doi:10.1016/0004-6981(85)90113-1, 1985.

Clarke, G. and Marshall, S. J.: Isotopic balance of the Greenland Ice Sheet: modelled concentrations of water isotopes from 30,000 BP to present, Quaternary Science Reviews, 21, 419–430, doi:10.1016/S0277-3791(01)00111-1, 2002.

Clarke, G., Lhomme, N., and Marshall, S. J.: Tracer transport in the Greenland ice sheet: three-dimensional isotopic stratigraphy, Quaternary Science Reviews, 24, 155–171, doi:10.1016/j.quascirev.2004.08.021, 2005.

Cogley, J. G., Hock, R., Rasmussen, L. A., Arendt, A. A., Bauder, A., Braithwaite, R. J., Kaser, G., Möller, M., Nicholson, L., and Zemp, M.: Glossary of glacier mass balance and related terms, IHP-VII Technical Documents in Hydrology No. 86, IACS Contribution No. 2 , UNESCO-IHP, Paris, 2011.

Cook, J., Edwards, A., Takeuchi, N., and Irvine-Fynn, T.: Cryoconite: The dark biological secret of the cryosphere, Progress in Physical Geography, 40, 66–111, doi:10.1177/0309133315616574, 2015.

Cuffey, K. M.: Methodology for use of Isotopic Climate Forcings in Ice Sheet Models, Geophysical Research Letters, 27, 3065–3068, doi:10.1029/2000GL011756, 2000.

Cuffey, K. M. and Clow, G. D.: Temperature, accumulation, and ice sheet elevation in central Greenland through the last deglacial transition, Journal of Geophysical Research, 102, 26 383–26 396, doi:10.1029/96JC0398, 1997.

Cuffey, K. M. and Paterson, W. S. B.: The Physics of Glaciers, Academic Press, Burlington and Oxford, 4 edn., 2010.

Cullen, N. J., Mölg, T., Conway, J., and Steffen, K.: Assessing the role of sublimation in the dry snow zone of the Greenland ice sheet in a warming world, Journal of Geophysical Research: Atmospheres, 119, 6563–6577, doi:10.1002/2014JD021557, 2014.

Dadic, R., Mullen, P. C., Schneebeli, M., Brandt, R. E., and Warren, S. G.: Effects of bubbles, cracks, and volcanic tephra on the spectral albedo of bare ice near the Transantarctic Mountains: Implications for sea glaciers on Snowball Earth, Journal of Geophysical Research: Earth Surface, 118, 1658–1676, doi:10.1002/jgrf.20098, 2013.

Dang, C., Brandt, R. E., and Warren, S. G.: Parameterizations for narrowband and broadband albedo of pure snow and snow containing mineral dust and black carbon, Journal of Geophysical Research: Atmospheres, 120, 5446–5468, doi:10.1002/2014JD022646, 2015.

Dansgaard, W.: Stable isotopes in precipitation, Tellus, 16, 436–468, doi:10.1111/j.2153-3490.1964.tb00181.x, 1964.

Dansgaard, W., Johnsen, S. J., Clausen, H. B., Dahl-Jensen, D., Gundestrup, N. S., Hammer, C. U., Hvidberg, C. S., Steffensen, J. P., Sveinbjörnsdóttir, A. E., Jouzel, J., and Bond, G.: Evidence for general instability of past climate from a 250-kyr ice-core record, Nature, 364, 218–220, doi:10.1038/364218a0, 1993.

de Almeida, R. C., Costa, G. A. S., Da Fonseca, L. C. M., and Alves, J. L. D.: Particle trajectory calculations with a two-step three-time level semi-Lagrangian scheme well suited for curved flows, International Journal for Numerical Methods in Fluids, 61, 995–1028, doi:10.1002/fld.1993, 2009.

De Angelis, M., Steffensen, J. P., Legrand, M., Clausen, H. B., and Hammer, C. U.: Primary aerosol (sea salt and soil dust) deposited in Greenland ice during the last climatic cycle: Comparison with east Antarctic records, Journal of Geophysical Research: Atmospheres, 102, 26 681–26 698, doi:10.1029/97JC01298, 1997.

Doherty, S. J., Warren, S. G., Grenfell, T. C., Clarke, A. D., and Brandt, R. E.: Light-absorbing impurities in Arctic snow, Atmospheric Chemistry and Physics, 10, 11 647–11 680, doi:10.5194/acp-10-11647-2010, 2010.

Doherty, S. J., Grenfell, T. C., Forsström, S., Hegg, D. L., Brandt, R. E., and Warren, S. G.: Observed vertical redistribution of black carbon and other insoluble light-absorbing particles in melting snow, Journal of Geophysical Research: Atmospheres, 118, 5553–5569, doi:10.1002/jgrd.50235, 2013.

Dozier, J.: Spectral signature of alpine snow cover from the landsat thematic mapper, Remote Sensing of Environment, 28, 9–22, doi:10.1016/0034-4257(89)90101-6, 1989.

REFERENCES

Dragosics, M., Meinander, O., Jónsdóttír, T., Dürig, T., De Leeuw, G., Pálsson, F., Dagsson-Waldhauserová, P., and Thorsteinsson, T.: Insulation effects of Icelandic dust and volcanic ash on snow and ice, Arabian Journal of Geosciences, 9, 1–10, doi:10.1007/s12517-015-2224-6, 2016.

Dumont, M., Brun, E., Picard, G., Michou, M., Libois, Q., Petit, J. R., Geyer, M., Morin, S., and Josse, B.: Contribution of light-absorbing impurities in snow to Greenland's darkening since 2009, Nature Geoscience, 7, 509–512, doi:10.1038/ngeo2180, 2014.

Enderlin, E. M., Howat, I. M., Jeong, S., Noh, M. J., Angelen, J. H., and Van den Broeke, M. R.: An improved mass budget for the Greenland ice sheet, Geophysical Research Letters, 41, 866–872, doi:10.1002/2013GL059010, 2014.

Fischer, H., Siggaard-Andersen, M.-L., Ruth, U., Röthlisberger, R., and Wolff, E. W.: Glacial/interglacial changes in mineral dust and sea-salt records in polar ice cores: Sources, transport, and deposition, Reviews of Geophysics, 45, RG1002, doi:10.1029/2005RG000192, 2007.

Fisher, D.: Comparison of 105 years of oxygen isotope and insoluble impurity profiles from the Devon Island and Camp Century ice cores, Quaternary Research, 11, 299–305, doi:10.1016/0033-5894(79)90077-2, 1979.

Fitzgerald, P. W., Bamber, J. L., Ridley, J. K., and Rougier, J. C.: Exploration of parametric uncertainty in a surface mass balance model applied to the Greenland ice sheet, Journal of Geophysical Research: Earth Surface, 117, F01 021, doi:10.1029/2011JF002067, 2012.

Flanner, M. G. and Zender, C. S.: Linking snowpack microphysics and albedo evolution, Journal of Geophysical Research, 111, D12 208, doi:10.1029/2005JD006834, 2006.

Flanner, M. G., Zender, C. S., Randerson, J. T., and Rasch, P. J.: Present-day climate forcing and response from black carbon in snow, Journal of Geophysical Research, 112, D11 202, doi:10.1029/2006JD008003, 2007.

Forsström, P.-L., Sallasmaa, O., Greve, R., and Zwinger, T.: Simulation of fast-flow features of the Fennoscandian ice sheet during the Last Glacial Maximum, Annals of Glaciology, 37, 383–389, doi:10.3189/172756403781815500, 2003.

Franco, B., Fettweis, X., and Erpicum, M.: Future projections of the Greenland ice sheet energy balance driving the surface melt, The Cryosphere, 7, 1–18, doi:10.5194/tc-7-1-2013, 2013.

Fuhrer, K., Wolff, E. W., and Johnsen, S. J.: Timescales for dust variability in the Greenland Ice Core Project (GRIP) ice core in the last 100,000 years, Journal of Geophysical Research: Atmospheres, 104, 31 043–31 052, doi:10.1029/1999JD900929, 1999.

Fyke, J. G., Vizcaino, M., Lipscomb, W., and Price, S.: Future climate warming increases Greenland ice sheet surface mass balance variability, Geophysical Research Letters, 41, 470–475, doi:10.1002/2013GL058172, 2014.

Gabbi, J., Huss, M., Bauder, A., Cao, F., and Schwikowski, M.: The impact of Saharan dust and black carbon on albedo and long-term mass balance of an Alpine glacier, The Cryosphere, 9, 1385–1400, doi:10.5194/tc-9-1385-2015, 2015.

Gagliardini, O., Zwinger, T., Gillet-Chaulet, F., Durand, G., Favier, L., Fleurian, B. d., Greve, R., Malinen, M., Martín, C., Råback, P., Ruokolainen, J., Sacchettini, M., Schäfer, M., Seddik, H., and Thies, J.: Capabilities and performance of Elmer/Ice, a new-generation ice sheet model, Geoscientific Model Development, 6, 1299–1318, doi:10.5194/gmd-6-1299-2013, 2013.

Gardner, A. and Sharp, M.: A review of snow and ice albedo and the development of a new physically based broadband albedo parameterization, Journal of Geophysical Research, 115, F01 009, doi:10.1029/2009JF001444, 2010.

Gat, J. R.: Oxygen and hydrogen isotopes in the hydrologic cycle , Annual Review of Earth and Planetary Sciences, 24, 225–262, doi:10.1146/annurev.earth.24.1.225, 1996.

Ge, J. M., Su, J., Ackerman, T. P., Fu, Q., Huang, J. P., and Shi, J. S.: Dust aerosol optical properties retrieval and radiative forcing over northwestern China during the 2008 China-U.S. joint field experiment, Journal of Geophysical Research: Atmospheres, 115, D00K12, doi:10.1029/2009JD013263, 2010.

Gent, P. R., Danabasoglu, G., Donner, L. J., Holland, M. M., Hunke, E. C., Jayne, S. R., Lawrence, D. M., Neale, R. B., Rasch, P. J., Vertenstein, M., Worley, P. H., Yang, Z.-L., and Zhang, M.: The Community Climate System Model Version 4, Journal of Climate, 24, 4973–4991, doi:10.1175/2011JCLI4083.1, 2011.

Goelles, T. and Bøggild, C. E.: Albedo reduction caused by black carbon and dust accumulation: a quantitive model applied to the western margin of the Greenland ice sheet, The Cryosphere Discussions, 9, 1345–1381, doi:10.5194/tcd-9-1345-2015, 2015.

Goelles, T., Grosfeld, K., and Lohmann, G.: Semi-Lagrangian transport of oxygen isotopes in polythermal ice sheets: implementation and first results, Geoscientific Model Development, 7, 1395–1408, doi:10.5194/gmd-7-1395-2014, 2014.

Goelles, T., Bøggild, C. E., and Greve, R.: Ice sheet mass loss caused by dust and black carbon accumulation, The Cryosphere, 9, 1845–1856, doi:10.5194/tc-9-1845-2015, 2015.

Goelzer, H., Huybrechts, P., Fürst, J. J., Nick, F. M., Andersen, M. L., Edwards, T. L., Fettweis, X., Payne, A. J., and Shannon, S.: Sensitivity of Greenland ice sheet projections to model formulations, Journal of Glaciology, 59, 733–749, doi:10.3189/2013JoG12J182, 2013.

Gornitz, V., ed.: Encyclopedia of Paleoclimatology and Ancient Environments , (Encyclopedia of Earth Sciences Series), Springer, New York, 1 edn., doi:10.1007/978-1-4020-4411-3, 2009.

REFERENCES

Green, R. O., Dozier, J., Roberts, D., and Painter, T.: Spectral snow-reflectance models for grain-size and liquid-water fraction in melting snow for the solar-reflected spectrum, Annals of Glaciology, 34, 71–73, doi:10.3189/172756402781817987, 2002.

Grenfell, T. C.: Albedo, in: Encyclopedia of Snow, Ice and Glaciers, edited by Singh, V. P., Singh, P., and Haritashya, U. K., pp. 23–35, Springer, Dordrecht, doi:10.1007/978-90-481-2642-2, 2011.

Greuell, W. and Konzelmann, T.: Numerical modelling of the energy balance and the englacial temperature of the Greenland Ice Sheet. Calculations for the ETH-Camp location (West Greenland, 1155 m a.s.l.), Global and Planetary Change, 9, 91–114, doi:10.1016/0921-8181(94)90010-8, 1994.

Greve, R.: A continuum-mechanical formulation for shallow polythermal ice sheets, Philosophical Transactions of the Royal Society of London Series a-Mathematical Physical and Engineering Sciences, 355, 921–974, 1997a.

Greve, R.: Application of a polythermal three-dimensional ice sheet model to the Greenland Ice Sheet: Response to steady-state and transient climate scenarios, Journal of Climate, 10, 901–918, doi:10.1175/1520-0442(1997)010<0901:AOAPTD>2.0.CO;2, 1997b.

Greve, R.: Relation of measured basal temperatures and the spatial distribution of the geothermal heat flux for the Greenland ice sheet, Annals of Glaciology, 42, 424–432, doi:10.3189/172756405781812510, 2005.

Greve, R. and Blatter, H.: Dynamics of Ice Sheets and Glaciers (Advances in Geophysical and Environmental Mechanics and Mathematics), Springer, Dordrecht, 1st edn., 2009.

Greve, R. and Blatter, H.: Comparison of thermodynamics solvers in the polythermal ice sheet model SICOPOLIS, Polar Science, 10, 11–23, doi:10.1016/j.polar.2015.12.004, 2016.

Greve, R. and Calov, R.: Comparison of Numerical Schemes for the Solution of the Ice-Thickness Equation in a Dynamic/Thermodynamic Ice-Sheet Model, Journal of Computational Physics, 179, 649–664, doi:10.1006/jcph.2002.7081, 2002.

Grönvold, K., Óskarsson, N., Johnsen, S. J., Clausen, H. B., Hammer, C. U., Bond, G., and Bard, E.: Ash layers from Iceland in the Greenland GRIP ice core correlated with oceanic and land sediments, Earth and Planetary Science Letters, 135, 149–155, doi:10.1016/0012-821X(95)00145-3, 1995.

Hammer, C. U., Clausen, H. B., Dansgaard, W., Neftel, A., Kristinsdottir, P., and Johnson, E.: Continuous Impurity Analysis Along the Dye 3 Deep Core, in: Greenland Ice Core Geophysics, Geochemistry, and the Environment, edited by Langway Jr, C. C., Oeschger, H., and Daansgard, W., pp. 90–94, American Geophysical Union, Washington DC, 1985.

Hansen, J. and Nazarenko, L.: Soot climate forcing via snow and ice albedos, Proceedings of the National Academy of Sciences of the United States of America, 101, 423–428, 2004.

Hansson, M. E.: The Renland ice core. A Northern Hemisphere record of aerosol composition over 120,000 years, Tellus B, 46, 390–418, doi:10.1034/j.1600-0889.1994.t01-4-00005.x, 1994.

Hegg, D. A., Warren, S. G., Grenfell, T. C., Doherty, S. J., and Clarke, A. D.: Sources of light-absorbing aerosol in arctic snow and their seasonal variation, Atmospheric Chemistry and Physics, 10, 10 923–10 938, doi:10.5194/acp-10-10923-2010, 2010.

Hock, R.: Glacier melt: a review of processes and their modelling, Progress in Physical Geography, 29, 362–391, doi:10.1191/0309133305pp453ra, 2005.

Hodson, A., Anesio, A. M., Ng, F., Watson, R., Quirk, J., Irvine-Fynn, T., Dye, A., Clark, C., McCloy, P., Kohler, J., and Sattler, B.: A glacier respires: Quantifying the distribution and respiration CO 2flux of cryoconite across an entire Arctic supraglacial ecosystem, Journal of Geophysical Research, 112, G04S36, doi:10.1029/2007JG000452, 2007.

Hodson, A., Bøggild, C. E., Hanna, E., Huybrechts, P., Langford, H., Cameron, K., and Houldsworth, A.: The cryoconite ecosystem on the Greenland ice sheet, Annals of Glaciology, 51, 123–129, doi:10.3189/172756411795931985, 2010.

Hodson, A. J.: Understanding the dynamics of black carbon and associated contaminants in glacial systems, Wiley Interdisciplinary Reviews: Water, 1, 141–149, doi:10.1002/wat2.1016, 2014.

Hoffmann, G., Werner, M., and Heimann, M.: Water isotope module of the ECHAM atmospheric general circulation model: A study on timescales from days to several years, Journal of Geophysical Research: Atmospheres, 103, 16 871–16 896, doi:10.1029/98JD00423, 1998.

Hortal, M.: The development and testing of a new two-time-level semi-Lagrangian scheme (SETTLS) in the ECMWF forecast model, Quarterly Journal of the Royal Meteorological Society, 128, 1671–1687, doi:10.1002/qj.200212858314, 2002.

Irvine-Fynn, T. D. L., Bridge, J. W., and Hodson, A. J.: In situ quantification of supraglacial cryoconite morphodynamics using time-lapse imaging: an example from Svalbard, Journal of Glaciology, 57, 651–657, doi:10.3189/002214311797409695, 2011a.

Irvine-Fynn, T. D. L., Hodson, A. J., Moorman, B. J., Vatne, G., and Hubbard, A. L.: POLYTHERMAL GLACIER HYDROLOGY: A REVIEW, Reviews of Geophysics, 49, RG4002, doi:10.1029/2010RG000350, 2011b.

Jean-Baptiste, P., Jouzel, J., Stievenard, M., and Ciais, P.: Experimental determination of the diffusion rate of deuterated water vapor in ice and application to the stable isotopes smoothing of ice cores, Earth and Planetary Science Letters, 158, 81–90, doi:10.1016/S0012-821X(98)00045-4, 1998.

Johnsen, S. J., Dahl-Jensen, D., DANSGAARD, W., and Gundestrup, N. S.: Greenland palaeotemperatures derived from GRIP bore hole temperature and ice core isotope profiles, Tellus B, 47, 624–629, doi:10.3402/tellusb.v47i5.16077, 1995.

Johnsen, S. J., Clausen, H. B., Dansgaard, W., Gundestrup, N., Hammer, C. U., Andersen, U., Andersen, K. K., Hvidberg, C., Dahl-Jensen, D., Steffensen, J. P., Shoji, H.,

Sveinbjörnsdóttir, A. E., White, J., Jouzel, J., and Fisher, D.: The δ18O record along the Greenland Ice Core Project deep ice core and the problem of possible Eemian climatic instability, Journal of Geophysical Research: Oceans, 102, 26 397–26 410, doi:10.1029/97JC00167, 1997.

Jouzel, J., Russell, G. L., Suozzo, R. J., Koster, R. D., WHITE, J., and Van den Broeke, M. R.: Simulations of the HDO and H_2 ^{18}O atmospheric cycles using the NASA GISS general circulation model: The seasonal cycle for present-day conditions, Journal of Geophysical Research: Atmospheres, 92, 14 739–14 760, doi:10.1029/JD092iD12p14739, 1987.

Jouzel, J., Alley, R. B., Cuffey, K. M., Dansgaard, W., Grootes, P., Hoffmann, G., Johnsen, S. J., Koster, R. D., Peel, D., Shuman, C. A., Stievenard, M., Stuiver, M., and White, J.: Validity of the temperature reconstruction from water isotopes in ice cores, Journal of Geophysical Research: Oceans, 102, 26 471–26 487, doi:10.1029/97JC01283, 1997.

Julio-Miranda, P., Delgado-Granados, H., Huggel, C., and Kääb, A.: Impact of the eruptive activity on glacier evolution at Popocatépetl Volcano (México) during 1994–2004, Journal of Volcanology and Geothermal Research, 170, 86–98, doi:10.1016/j.jvolgeores.2007.09.011, 2008.

Kjeldsen, K. K., Korsgaard, N. J., Bjørk, A. A., Khan, S. A., Box, J. E., Funder, S., Larsen, N. K., Bamber, J. L., Colgan, W., Van den Broeke, M. R., Siggaard-Andersen, M.-L., Nuth, C., Schomacker, A., Andresen, C. S., Willerslev, E., and Kjær, K. H.: Spatial and temporal distribution of mass loss from the Greenland Ice Sheet since AD 1900, Nature, 528, 396–400, doi:10.1038/nature16183, 2015.

Klok, E. J. and Oerlemans, J.: Model study of the spatial distribution of the energy and mass balance of Morteratschgletscher, Switzerland, Journal of Glaciology, 48, 505–518, doi:10.3189/172756502781831133, 2002.

Knap, W. H. and Oerlemans, J.: The surface albedo of the Greenland ice sheet: Satellite-derived and in situ measurements in the Sondre Stromfjord area during the 1991 melt season, Journal of Glaciology, 42, 364–374, 1996.

Kohshima, S., Yoshimura, Y., and Seko, K.: Biotic Acceleration of Glacier Melting in Yala Glacier, Langtang Region, Nepal Himalaya, IAHS Publication, pp. 309–316, 1993.

Konzelmann, T. and Braithwaite, R.: Variations of ablation, albedo and energy balance at the margin of the Greenland ice sheet, Kronprins Christian Land, eastern north Greenland. , Journal of Glaciology, 41, 174–182, 1995.

Langebroek, P. M., Paul, A., and Schulz, M.: Simulating the sea level imprint on marine oxygen isotope records during the middle Miocene using an ice sheet-climate model, Paleoceanography, 25, PA4203, doi:10.1029/2008PA001704, 2010.

Langford, H., Hodson, A., Banwart, S., and Bøggild, C. E.: The microstructure and biogeochemistry of Arctic cryoconite granules, Annals of Glaciology, 51, 87–94, doi:10.3189/172756411795932083, 2010.

Lee, Y. H., Lamarque, J. F., Flanner, M. G., Jiao, C., Shindell, D. T., Berntsen, T., Bisiaux, M. M., Cao, J., Collins, W. J., Curran, M., Edwards, R., Faluvegi, G., Ghan, S., Horowitz, L. W., McConnell, J. R., Ming, J., Myhre, G., Nagashima, T., Naik, V., Rumbold, S. T., Skeie, R. B., Sudo, K., Takemura, T., Thevenon, F., Xu, B., and Yoon, J. H.: Evaluation of preindustrial to present-day black carbon and its albedo forcing from Atmospheric Chemistry and Climate Model Intercomparison Project (ACCMIP), Atmospheric Chemistry and Physics, 13, 2607–2634, doi:10.5194/acp-13-2607-2013, 2013.

Lei, Y., Zhang, Q., He, K. B., and Streets, D. G.: Primary anthropogenic aerosol emission trends for China, 1990-2005, Atmospheric Chemistry and Physics, 11, 931–954, doi:10.5194/acp-11-931-2011, 2011.

Lekien, F. and Marsden, J.: Tricubic interpolation in three dimensions, International Journal for Numerical Methods in Engineering, 63, 455–471, doi:10.1002/nme.1296, 2005.

Lhomme, N.: Modelling water isotopes in polar ice sheets, Ph.D. thesis, The University of British Columbia, 2004.

Lhomme, N., Clarke, G., and Marshall, S. J.: Tracer transport in the Greenland Ice Sheet: constraints on ice cores and glacial history, Quaternary Science Reviews, 24, 173–194, doi:10.1016/j.quascirev.2004.08.020, 2005a.

Lhomme, N., Clarke, G., and Ritz, C.: Global budget of water isotopes inferred from polar ice sheets, Geophysical Research Letters, 32, L20 502, doi:10.1029/2005GL023774, 2005b.

Liou, K. N.: An Introduction to Atmospheric Radiation, Volume 84, Second Edition (International Geophysics), Academic Press, San Diego and London, 2 edn., 2002.

Lipscomb, W. H., Fyke, J. G., Vizcaino, M., Sacks, W. J., Wolfe, J., Vertenstein, M., Craig, A., Kluzek, E., and Lawrence, D. M.: Implementation and Initial Evaluation of the Glimmer Community Ice Sheet Model in the Community Earth System Model, Journal of Climate, 26, 7352–7371, doi:10.1175/JCLI-D-12-00557.1, 2013.

Lliboutry, L. and Duval, P.: Various isotropic and anisotropic ices found in glaciers and polar ice caps and their corresponding rheologies, Annales geophysicae, 3, 207–224, 1985.

Lu, Z., Zhang, Q., and Streets, D. G.: Sulfur dioxide and primary carbonaceous aerosol emissions in China and India, 1996–2010, Atmospheric Chemistry and Physics, 11, 9839–9864, doi:10.5194/acp-11-9839-2011, 2011.

MacGregor, J. A., Fahnestock, M. A., Catania, G. A., Paden, J. D., Gogineni, S. P., Young, S. K., Rybarski, S. C., Mabrey, A. N., Wagman, B. M., and Morlighem, M.: Radiostratigraphy and age structure of the Greenland Ice Sheet, Journal of Geophysical Research: Earth Surface, 120, 212–241, doi:10.1002/2014jf003215, 2015.

Mahowald, N. M., Albani, S., Engelstaedter, S., Winckler, G., and Goman, M.: Model insight into glacial-interglacial paleodust records, Quaternary Science Reviews, 30, 832–854, doi:10.1016/j.quascirev.2010.09.007, 2011.

REFERENCES

Masson-Delmotte, V., Hou, S., Ekaykin, A., Jouzel, J., Aristarain, A., Bernardo, R. T., Bromwich, D., Cattani, O., Delmotte, M., Falourd, S., Frezzotti, M., Gallee, H., Genoni, L., Isaksson, E., Landais, A., Helsen, M. M., Hoffmann, G., Lopez, J., Morgan, V., Motoyama, H., Noone, D., Oerter, H., Petit, J. R., Royer, A., Uemura, R., Schmidt, G. A., Schlosser, E., Simoes, J. C., Steig, E. J., Stenni, B., Stievenard, M., Van den Broeke, M. R., Van de Wal, R. S. W., Van de Berg, W. J., Vimeux, F., and White, J. W. C.: A review of Antarctic surface snow isotopic composition: Observations, atmospheric circulation, and isotopic modeling, Journal of Climate, 21, 3359–3387, doi:10.1175/2007JCLI2139.1, 2008.

Maurette, M., Jéhanno, C., Robin, E., and Hammer, C. U.: Characteristics and mass distribution of extraterrestrial dust from the Greenland ice cap, Nature, 328, 699–702, doi:10.1038/328699a0, 1987.

Mayewski, P. A., Meeker, L. D., Twickler, M. S., Whitlow, S., Yang, Q., Lyons, W. B., and Prentice, M.: Major features and forcing of high-latitude northern hemisphere atmospheric circulation using a 110,000-year-long glaciochemical series, Journal of Geophysical Research: Atmospheres, 102, 26 345–26 366, doi:10.1029/96JC03365, 1997.

McConnell, J., Edwards, R., Kok, G., Flanner, M., Zender, C. S., Saltzman, E., Banta, J., Pasteris, D., Carter, M., and Kahl, J.: 20th-century industrial black carbon emissions altered arctic climate forcing, Science, 317, 1381–1384, doi:10.1126/science.1144856, 2007.

McGregor, J. L.: Economical Determination of Departure Points for Semi-Lagrangian Models, Monthly Weather Review, 121, 221–230, doi:10.1175/1520-0493(1993)121<0221:EDODPF>2.0.CO;2, 1993.

Mernild, S. H., Liston, G. E., Hiemstra, C. A., and Christensen, J. H.: Greenland Ice Sheet Surface Mass-Balance Modeling in a 131-Yr Perspective, 1950–2080, Journal of Hydrometeorology, 11, 3–25, doi:10.1175/2009JHM1140.1, 2010.

Miteva, V., Rinehold, K., Sowers, T., Sebastian, A., and Brenchley, J.: Abundance, viability and diversity of the indigenous microbial populations at different depths of the NEEM Greenland ice core, Polar Research, 34, 25 057, doi:10.3402/polar.v34.25057, 2015.

Miteva, V. I., Sheridan, P. P., and Brenchley, J. E.: Phylogenetic and Physiological Diversity of Microorganisms Isolated from a Deep Greenland Glacier Ice Core, Applied and Environmental Microbiology, 70, 202–213, doi:10.1128/AEM.70.1.202-213.2004, 2004.

Möller, R., Möller, M., Björnsson, H., Guðmundsson, S., Pálsson, F., Oddsson, B., Kukla, P. A., and Schneider, C.: MODIS-derived albedo changes of Vatnajökull (Iceland) due to tephra deposition from the 2004 Grímsvötn eruption, International Journal of Applied Earth Observation and Geoinformation, 26, 256–269, doi:10.1016/j.jag.2013.08.005, 2014.

Moustafa, S. E., Rennermalm, A. K., Smith, L. C., Miller, M. A., Mioduszewski, J. R., Koenig, L. S., Hom, M. G., and Shuman, C. A.: Multi-modal albedo distributions in the

ablation area of the southwestern Greenland Ice Sheet, The Cryosphere, 9, 905–923, doi:10.5194/tc-9-905-2015, 2015.

Mullen, P. C. and Warren, S. G.: Theory of the Optical-Properties of Lake Ice, Journal of Geophysical Research: Atmospheres, 93, 8403–8414, doi:10.1029/JD093iD07p08403, 1988.

Müller, F. and Keeler, C.: Errors in short-term ablation measurements on melting ice surfaces, Journal of Glaciology, 8, 91–105, 1969.

Nair, R. D., Scroggs, J., and Semazzi, F.: A forward-trajectory global semi-Lagrangian transport scheme, Journal of Computational Physics, 190, 275–294, doi:10.1016/S0021-9991(03)00274-2, 2003.

Nansen, F., ed.: The Norwegian North polar expedition, 1893-1896; scientific results , Longmans, Green and co., London, doi:10.5962/bhl.title.6514, 1906.

Narcisi, B., Petit, J.-R., and Chappellaz, J.: A 70 ka record of explosive eruptions from the TALDICE ice core (Talos Dome, East Antarctic plateau), Journal of Quaternary Science, 25, 844–849, doi:10.1002/jqs.1427, 2010.

NEEM community members: A Holocene dust concentration record from the new greenlandic NEEM ice core - Preliminary results, in: Workshop on High-mid latitude northern atmospheric circulation, 2009.

Nghiem, S. V., Hall, D. K., Mote, T. L., Tedesco, M., Albert, M. R., Keegan, K., Shuman, C. A., DiGirolamo, N. E., and Neumann, G.: The extreme melt across the Greenland ice sheet in 2012, Geophysical Research Letters, 39, L20 502, doi:10.1029/2012GL053611, 2012.

Nield, J. M., Chiverrell, R. C., Darby, S. E., Leyland, J., Vircavs, L. H., and Jacobs, B.: Complex spatial feedbacks of tephra redistribution, ice melt and surface roughness modulate ablation on tephra covered glaciers, Earth Surface Processes and Landforms, 38, 95–102, doi:10.1002/esp.3352, 2012.

Noël, B., Van de Berg, W. J., van Meijgaard, E., Kuipers Munneke, P., Van de Wal, R. S. W., and Van den Broeke, M. R.: Evaluation of the updated regional climate model RACMO2.3 : Summer snowfall impact on the Greenland Ice Sheet, The Cryosphere, 9, 1831–1844, doi:10.5194/tc-9-1831-2015, 2015.

Nordenskiöld, N. A. E.: Cryoconite found 1870, July 19th-25th, on the inland ice, east of Auleitsivik Fjord, Disco Bay, Greenland , Geological Magazine, 2, 157–162, 1875.

Oaida, C. M., Xue, Y., Flanner, M. G., Skiles, S. M., De Sales, F., and Painter, T. H.: Improving snow albedo processes in WRF/SSiB regional climate model to assess impact of dust and black carbon in snow on surface energy balance and hydrology over western U.S., Journal of Geophysical Research: Atmospheres, 120, 3228–3248, doi:10.1002/2014JD022444, 2015.

Oerlemans, J.: A model for the surface balance of ice masses: Part I: alpine glaciers, Zeitschrift für Gletscherkunde und Glacialgeologie, 27, 63–83, 1991.

Oerlemans, J.: Glaciers and climate change, A.A. Balkema Publishers, Lisse, Abingdon, Exton (PA), Tokyo, 2001.

Oerlemans, J., Giesen, R. H., and Van den Broeke, M. R.: Retreating alpine glaciers: increased melt rates due to accumulation of dust (Vadret da Morteratsch, Switzerland), Journal of Glaciology, 55, 729–736, doi:10.3189/002214309789470969, 2009.

Painter, T. H., Flanner, M. G., Kaser, G., Marzeion, B., VanCuren, R. A., and Abdalati, W.: End of the Little Ice Age in the Alps forced by industrial black carbon, Proceedings of the National Academy of Sciences of the United States of America, 110, 15 216–15 221, doi:10.1073/pnas.1302570110, 2013.

Parrenin, F., Remy, F., Ritz, C., Siegert, M. J., and Jouzel, J.: New modeling of the Vostok ice flow line and implication for the glaciological chronology of the Vostok ice core, Journal of Geophysical Research, 109, D20 102, doi:10.1029/2004JD004561, 2004.

Payne, A., Huybrechts, P., Abe-Ouchi, A., Calov, R., Fastook, J., Greve, R., Marshall, S. J., Marsiat, I., Ritz, C., Tarasov, L., and Thomassen, M.: Results from the EISMINT model intercomparison: the effects of thermomechanical coupling, Journal of Glaciology, 46, 227–238, doi:10.3189/172756500781832891, 2000.

Pearce, D. A., Bridge, P. D., Hughes, K. A., Sattler, B., Psenner, R., and Russell, N. J.: Microorganisms in the atmosphere over Antarctica, FEMS Microbiology Ecology, 69, 143–157, doi:10.1111/j.1574-6941.2009.00706.x, 2009.

Petit, J. R., Jouzel, J., Raynaud, D., Barkov, N., Barnola, J. M., Basile, I., Bender, M., Chappellaz, J., Davis, M., Delaygue, G., Delmotte, M., Kotlyakov, V., Legrand, M., Lipenkov, V., Lorius, C., Pepin, L., Ritz, C., Saltzman, E., and Stievenard, M.: Climate and atmospheric history of the past 420,000 years from the Vostok ice core, Antarctica, Nature, 399, 429–436, doi:10.1038/20859, 1999.

Petzold, A., Ogren, J. A., Fiebig, M., Laj, P., Li, S. M., Baltensperger, U., Holzer-Popp, T., Kinne, S., Pappalardo, G., Sugimoto, N., Wehrli, C., Wiedensohler, A., and Zhang, X. Y.: Recommendations for reporting "black carbon" measurements, Atmospheric Chemistry and Physics, 13, 8365–8379, doi:10.5194/acp-13-8365-2013, 2013.

Polashenski, C. M., Dibb, J. E., Flanner, M. G., Chen, J. Y., Courville, Z. R., Lai, A. M., Schauer, J. J., Shafer, M. M., and Bergin, M.: Neither dust nor black carbon causing apparent albedo decline in Greenland's dry snow zone: implications for MODIS C5 surface reflectance, Geophysical Research Letters, 42, 9319–9327, doi:10.1002/2015GL065912, 2015.

Press, W. H., Teukolsky, S. A., Vetterling, W. T., and Flannery, B. P.: Numerical recipes in Fortran 90: the art of parallel scientific computing, Cambridge University Press, New York, NY, USA, 2nd edn., 1996.

Price, P. B.: Microbial life in glacial ice and implications for a cold origin of life, FEMS Microbiology Ecology, 59, 217–231, doi:10.1111/j.1574-6941.2006.00234.x, 2007.

Price, P. B., Rohde, R. A., and Bay, R. C.: Fluxes of microbes, organic aerosols, dust, sea-salt Na ions, non-sea-salt Ca ions, and methanesulfonate onto Greenland and Antarctic ice, Biogeosciences, 6, 479–486, doi:10.5194/bg-6-479-2009, 2009.

Purser, R. and Leslie, L.: An Efficient Semi-Lagrangian Schme using Third-Order Semi-Implicit Time Integration and Forward Trajectories, Monthly Weather Review, 122, 745–756, doi:10.1175/1520-0493(1994)122<0745:AESLSU>2.0.CO;2, 1994.

Quesada, A., Vincent, W. F., and Lean, D. R. S.: Community and pigment structure of Arctic cyanobacterial assemblages: the occurrence and distribution of UV-absorbing compounds, FEMS Microbiology Ecology, 28, 315–323, doi:10.1111/j.1574-6941.1999.tb00586.x, 1999.

Rae, J. G. L., Aðalgeirsdóttir, G., Edwards, T. L., Fettweis, X., Gregory, J. M., Hewitt, H. T., Lowe, J. A., Lucas-Picher, b. P., Mottram, R. H., Payne, A. J., Ridley, J. K., Shannon, S. R., Van de Berg, W. J., Van de Wal, R. S. W., and Van den Broeke, M. R.: Greenland ice sheet surface mass balance: evaluating simulations and making projections with regional climate models, The Cryosphere, 6, 1275–1294, doi:10.5194/tc-6-1275-2012, 2012.

Rango, A. and Martinec, J.: Revisiting the Degree-Day Method for Snowmelt Computations, JAWRA Journal of the American Water Resources Association, 31, 657–669, doi:10.1111/j.1752-1688.1995.tb03392.x, 1995.

Rasmussen, S. O., Seierstad, I. K., Andersen, K. K., Bigler, M., Dahl-Jensen, D., and Johnsen, S. J.: Synchronization of the NGRIP, GRIP, and GISP2 ice cores across MIS 2 and palaeoclimatic implications, Quaternary Science Reviews, 27, 18–28, doi:10.1016/j.quascirev.2007.01.016, 2008.

Reeh, N.: Parameterization of Melt Rate and Surfaee Temperature on the Greenland lee Sheet, Polarforschung, 53, 113–128, 1991.

Reeh, N., Oerter, H., Letréguilly, A., Miller, H., and Hubberten, H.-W.: A new, detailed ice-age oxygen-18 record from the ice-sheet margin in central West Greenland, Palaeogeography, Palaeoclimatology, Palaeoecology (Global and Planetary Change Section), 4, 373–383, doi:10.1016/0921-8181(91)90003-F, 1991.

Reisinger, P., Wonaschütz, A., Hitzenberger, R., Petzold, A., Bauer, H., Jankowski, N., Puxbaum, H., Chi, X., and Maenhaut, W.: Intercomparison of Measurement Techniques for Black or Elemental Carbon Under Urban Background Conditions in Wintertime: Influence of Biomass Combustion, Environmental Science & Technology, 42, 884–889, doi:10.1021/es0715041, 2008.

Remias, D., Holzinger, A., Aigner, S., and Luetz, C.: Ecophysiology and ultrastructure of Ancylonema nordenskioldii (Zygnematales, Streptophyta), causing brown ice on glaciers in Svalbard (high arctic), Polar Biology, 35, 899–908, doi:10.1007/s00300-011-1135-6, 2012.

Robinson, A., Calov, R., and Ganopolski, A.: An efficient regional energy-moisture balance model for simulation of the Greenland Ice Sheet response to climate change, The Cryosphere, 4, 129–144, doi:10.5194/tc-4-129-2010, 2010.

Robinson, A., Calov, R., and Ganopolski, A.: Greenland ice sheet model parameters constrained using simulations of the Eemian Interglacial, Climate of the Past, 7, 381–396, doi:10.5194/cp-7-381-2011, 2011.

Ruth, U.: Dust concentration in the NGRIP ice core, doi:10.1594/PANGAEA.587836, Supplement to: Ruth, U., Bigler, M., Röthlisberger, R., Siggaard-Andersen, M.-L., Kipfstuhl, J., Goto-Azuma, K., Hansson, M. E., Johnsen, S. J., Lu, H., and Steffensen, J. P.: Ice core evidence for a very tight link between North Atlantic and east Asian glacial climate, Geophysical Research Letters, 34, L03 706, doi:10.1029/2006GL027876, 2007.

Ruth, U., Wagenbach, D., Steffensen, J. P., and Bigler, M.: Continuous record of microparticle concentration and size distribution in the central Greenland NGRIP ice core during the last glacial period, Journal of Geophysical Research, 108, 4098, doi:10.1029/2002JD002376, 2003.

Rybak, O. and Huybrechts, P.: A comparison of Eulerian and Lagrangian methods for dating in numerical ice-sheet models, Annals of Glaciology, 37, 150–158, doi:10.3189/172756403781815393, 2003.

Satheesh, S. and Krishna Moorthy, K.: Radiative effects of natural aerosols: A review, Atmospheric Environment, 39, 2089–2110, doi:10.1016/j.atmosenv.2004.12.029, 2005.

Shepherd, A., Ivins, E. R., A, G., Barletta, V. R., Bentley, M. J., Bettadpur, S., Briggs, K. H., Bromwich, D. H., Forsberg, R., Galin, N., Horwath, M., Jacobs, S., Joughin, I., King, M. A., Lenaerts, J. T. M., Li, J., Ligtenberg, S. R. M., Luckman, A., Luthcke, S. B., McMillan, M., Meister, R., Milne, G., Mouginot, J., Muir, A., Nicolas, J. P., Paden, J., Payne, A. J., Pritchard, H., Rignot, E., Rott, H., Sørensen, L. S., Scambos, T. A., Scheuchl, B., Schrama, E. J. O., Smith, B., Sundal, A. V., van Angelen, J. H., Van de Berg, W. J., Van den Broeke, M. R., Vaughan, D. G., Velicogna, I., Wahr, J., Whitehouse, P. L., Wingham, D. J., Yi, D., Young, D., and Zwally, H. J.: A Reconciled Estimate of Ice-Sheet Mass Balance, Science, 338, 1183–1189, doi:10.1126/science.1228102, 2012.

Skeie, R. B., Berntsen, T., Myhre, G., Pedersen, C. A., Ström, J., Gerland, S., and Ogren, J. A.: Black carbon in the atmosphere and snow, from pre-industrial times until present, Atmospheric Chemistry and Physics, 11, 6809–6836, doi:10.5194/acp-11-6809-2011, 2011.

Slater, J. F., Currie, L. A., Dibb, J. E., and Benner, Jr., B. A.: Distinguishing the relative contribution of fossil fuel and biomass combustion aerosols deposited at Summit, Greenland through isotopic and molecular characterization of insoluble carbon, Atmospheric Environment, 36, 4463–4477, doi:10.1016/S1352-2310(02)00402-8, 2002.

Staniforth, A. and Côté, J.: Semi-Lagrangian Integration Schemes for Atmospheric Models-A Review, Monthly Weather Review, 119, 2206–2223, doi:10.1175/1520-0493(1991)119<2206:SLISFA>2.0.CO;2, 1991.

Staniforth, A. and Pudykiewicz, J.: Reply to comments on and addenda to "some properties and comparative performance of the semi-lagrangian method of Robert in the solution of the advection-diffusion equation", Atmosphere-Ocean, 23, 195–200, doi:10.1080/07055900.1985.9649224, 1985.

Staniforth, A., White, A., and Wood, N.: Analysis of semi-Lagrangian trajectory computations, Quarterly Journal of the Royal Meteorological Society, 129, 2065–2085, doi:10.1256/qj.02.115, 2003.

Steffensen, J. P.: The size distribution of microparticles from selected segments of the Greenland Ice Core Project ice core representing different climatic periods, Journal of Geophysical Research, 102, 26 755–26 763, doi:10.1029/97JC01490, 1997.

Stibal, M., Lawson, E. C., Lis, G. P., Mak, K. M., Wadham, J. L., and Anesio, A. M.: Organic matter content and quality in supraglacial debris across the ablation zone of the Greenland ice sheet, Annals of Glaciology, 51, 1–8, doi:10.3189/172756411795931958, 2010.

Stibal, M., Šabacká, M., and Žárský, J.: Biological processes on glacier and ice sheet surfaces, Nature Geoscience, 5, 771–774, doi:10.1038/ngeo1611, 2012.

Stocker, T. F., Qin, Plattner, G. K., Tignor, M., Allen, S. K., Boschung, J., Nauels, A., Xia, Y., Bex, V., and Midgley, P. M., eds.: Climate Change 2013: The Physical Science Basis: Working Group I Contribution to the Fifth Assessment Report of the Intergovernmental Panel on Climate Change, Working Group I Contribution to the Fifth Assessment Report of the Intergovernmental Panel on Climate Change, Cambridge University Press, Cambridge, doi:10.1017/CBO9781107415324.004, 2013.

Stroeve, J., Box, J. E., Wang, Z., Schaaf, C., and Barrett, A.: Re-evaluation of MODIS MCD43 Greenland albedo accuracy and trends, Remote Sensing of Environment, 138, 199–214, doi:10.1016/j.rse.2013.07.023, 2013.

Sturm, C., Zhang, Q., and Noone, D.: An introduction to stable water isotopes in climate models: benefits of forward proxy modelling for paleoclimatology, Climate of the Past, 6, 115–129, doi:10.5194/cp-6-115-2010, 2010.

Swan, L. W.: The Aeolian Biome, BioScience, 42, 262–270, doi:10.2307/1311674, 1992.

Takeuchi, N.: Optical characteristics of cryoconite (surface dust) on glaciers: the relationship between light absorbency and the property of organic matter contained in the cryoconite, Annals of Glaciology, 34, 409–414, doi:10.3189/172756402781817743, 2002.

Takeuchi, N.: Cryoconite, in: Encyclopedia of Snow, Ice and Glaciers, edited by Singh, V. P., Singh, P., and Haritashya, U. K., pp. 168–171, Springer, Dordrecht, doi:10.1007/978-90-481-2642-2, 2011.

Takeuchi, N., Kohshima, S., and Seko, K.: Structure, formation, and darkening process of albedo-reducing material (cryoconite) on a Himalayan glacier: A granular algal mat growing on the glacier, Arctic Antarctic and Alpine Research, 33, 115–122, doi:10.2307/1552211, 2001.

Takeuchi, N., Nishiyama, H., and Li, Z.: Structure and formation process of cryoconite granules on Ürümqi glacier No. 1, Tien Shan, China, Annals of Glaciology, 51, 9–14, doi:10.3189/172756411795932010, 2010.

Takeuchi, N., Nagatsuka, N., Uetake, J., and Shimada, R.: Spatial variations in impurities (cryoconite) on glaciers in northwest Greenland, Bulletin of Glaciological Research, 32, 85–94, doi:10.5331/bgr.32.85, 2014.

Tarasov, L. and Peltier, W.: Greenland glacial history, borehole constraints, and Eemian extent, Journal of Geophysical Research, 108, 2143, doi:10.1029/2001JB001731, 2003.

Taylor, K. C., Mayewski, P. A., Alley, R. B., Brook, E. J., Gow, A. J., Grootes, P. M., Meese, D. A., Saltzman, E. S., Severinghaus, J. P., Twickler, M. S., White, J. W. C., Whitlow, S., and Zielinski, G. A.: The Holocene-Younger Dryas Transition Recorded at Summit, Greenland, Science, 278, 825–827, doi:10.1126/science.278.5339.825, 1997.

Tedesco, M., Fettweis, X., Van den Broeke, M. R., Van de Wal, R. S. W., Smeets, C. J. P. P., Van de Berg, W. J., Serreze, M. C., and Box, J. E.: The role of albedo and accumulation in the 2010 melting record in Greenland, Environmental Research Letters, 6, 014 005, doi:10.1088/1748-9326/6/1/014005, 2011.

Tedesco, M., Foreman, C. M., Anton, J., Steiner, N., and Schwartzman, T.: Comparative analysis of morphological, mineralogical and spectral properties of cryoconite in Jakobshavn Isbrae, Greenland, and Canada Glacier, Antarctica, Annals of Glaciology, 54, 147–157, doi:10.3189/2013AoG63A417, 2013.

Tedesco, M., Fettweis, X., Alexander, P., Green, G., and Datta, T.: MAR Greenland Outputs from Outputs 2005-01-01 to 2013-01-01 ver. 3.2, CCNY Digital Archive, 2014.

Tedesco, M., Doherty, S., Fettweis, X., Alexander, P., Jeyaratnam, J., and Stroeve, J.: The darkening of the Greenland ice sheet: trends, drivers, and projections (1981-2100), The Cryosphere, 10, 477–496, doi:10.5194/tc-10-477-2016, 2016.

Tegen, I. and Fung, I.: Modeling of mineral dust in the atmosphere: Sources, transport, and optical thickness, Journal of Geophysical Research, 99, 22 897–22 914, doi:10.1029/94JD01928, 1994.

Thomas, R. H. and PARCA Investigators: Program for Arctic Regional Climate Assessment (PARCA): Goals, key findings, and future directions, Journal of Geophysical Research, 106, 33 691–33 705, doi:10.1029/2001JD900042, 2001.

Thorarinsson, S.: The Swift Flowing Rivers — The History of Grimsvötn Eruptions and Jökulhlaups in Skeidara, Menningarsjodur Publishing, Reykjavik, 1974.

Újvári, G., Stevens, T., Svensson, A., Klötzli, U. S., Manning, C., Németh, T., Kovács, J., Sweeney, M. R., Gocke, M., Wiesenberg, G. L. B., Markovic, S. B., and Zech, M.: Two

possible source regions for central Greenland last glacial dust, Geophysical Research Letters, 42, 10,399–10,408, doi:10.1002/2015GL066153, 2015.

UNIDATA: NetCDF (network Common Data Form), URL `http://www.unidata.ucar.edu/software/netcdf/`, accessed: 2016-04-17, 2016.

van Angelen, J. H., Lenaerts, J. T. M., Lhermitte, S., Fettweis, X., Kuipers Munneke, P., Van den Broeke, M. R., van Meijgaard, E., and Smeets, C. J. P. P.: Sensitivity of Greenland Ice Sheet surface mass balance to surface albedo parameterization: a study with a regional climate model, The Cryosphere, 6, 1175–1186, doi:10.5194/tc-6-1175-2012, 2012.

Van As, D.: Warming, glacier melt and surface energy budget from weather station observations in the Melville Bay region of northwest Greenland, Journal of Glaciology, 57, 208–220, doi:10.3189/002214311796405898, 2011.

Van As, D., Hubbard, A. L., Hasholt, B., Mikkelsen, A. B., Van den Broeke, M. R., and Fausto, R. S.: Large surface meltwater discharge from the Kangerlussuaq sector of the Greenland ice sheet during the record-warm year 2010 explained by detailed energy balance observations, The Cryosphere, 6, 199–209, doi:10.5194/tc-6-199-2012, 2012.

Van de Wal, R. S. W., Greuell, W., Van den Broeke, M. R., Reijmer, C. H., and Oerlemans, J.: Surface mass-balance observations and automatic weather station data along a transect near Kangerlussuaq, West Greenland, Annals of Glaciology, 42, 311–316, doi:10.3189/172756405781812529, 2005.

Van den Berg, J., Van de Wal, R. S. W., and Oerlemans, J.: A mass balance model for the Eurasian ice sheet for the last 120,000 years, Global and Planetary Change, 61, 194–208, doi:10.1016/j.gloplacha.2007.08.015, 2008.

Van den Broeke, M. R., Smeets, P., Ettema, J., and Munneke, P. K.: Surface radiation balance in the ablation zone of the west Greenland ice sheet, Journal of Geophysical Research: Atmospheres, 113, D13 105, doi:10.1029/2007JD009283, 2008.

Van den Broeke, M. R., Bamber, J., Ettema, J., Rignot, E., Schrama, E., Van de Berg, W. J., van Meijgaard, E., Velicogna, I., and Wouters, B.: Partitioning Recent Greenland Mass Loss, Science, 326, 984–986, doi:10.1126/science.1178176, 2009.

Vaughan, D. G., Comiso, J. C., Allison, I., Kaser, G., Kwok, R., Mote, P., Murray, T., Paul, F., Ren, J., Rignot, E., Solomina, O., Steffen, K., and Zhang, T.: Observations:Cryosphere, in: Climate Change 2013: The Physical Science Basis. Contribution of Working Group I to the Fifth Assessment Report of the Intergovernmental Panel on Climate Change, edited by Stocker, T. F., Qin, Plattner, G. K., Tignor, M., Allen, S. K., Boschung, J., Nauels, A., Xia, Y., Bex, V., and Midgley, P. M., pp. 317–382, Cambridge University Press, Cambridge, United Kingdom and New York, NY, USA, 2013.

Vizcaino, M., Lipscomb, W. H., Sacks, W. J., van Angelen, J. H., Wouters, B., and Van den Broeke, M. R.: Greenland Surface Mass Balance as Simulated by the Community Earth System Model. Part I: Model Evaluation and 1850-2005 Results, Journal of Climate, 26, 7793–7812, doi:10.1175/JCLI-D-12-00615.1, 2013.

REFERENCES

Vizcaino, M., Lipscomb, W. H., Sacks, W. J., and Van den Broeke, M. R.: Greenland Surface Mass Balance as Simulated by the Community Earth System Model. Part II: Twenty-First-Century Changes, Journal of Climate, 27, 215–226, doi:10.1175/JCLI-D-12-00588.1, 2014.

Wagner, R., Ajtai, T., Kandler, K., Lieke, K., Linke, C., Müller, T., Schnaiter, M., and Vragel, M.: Complex refractive indices of Saharan dust samples at visible and near UV wavelengths: a laboratory study, Atmospheric Chemistry and Physics, 12, 2491–2512, doi:10.5194/acp-12-2491-2012, 2012.

Warren, S. G. and Brandt, R. E.: Optical constants of ice from the ultraviolet to the microwave: A revised compilation, Journal of Geophysical Research, 113, D14 220, doi:10.1029/2007JD009744, 2008.

Warren, S. G. and Wiscombe, W. J.: A model for the spectral albedo of snow. II: Snow containing atmospheric aerosols, Journal Of The Atmospheric Sciences, 37, 2734–2745, doi:10.1175/1520-0469(1980)037<2734:AMFTSA>2.0.CO;2, 1980.

Warren, S. G., Brandt, R. E., and Grenfell, T. C.: Visible and near-ultraviolet absorption spectrum of ice from transmission of solar radiation into snow, Applied Optics, 45, 5320–5334, doi:10.1364/AO.45.005320, 2006.

Werner, M., Langebroek, P. M., Carlsen, T., Herold, M., and Lohmann, G.: Stable water isotopes in the ECHAM5 general circulation model: Toward high-resolution isotope modeling on a global scale, Journal of Geophysical Research, 116, D15 109, doi:10.1029/2011JD015681, 2011.

Wessel, P. and Smith, W. H. F.: New, improved version of generic mapping tools released, Eos, Transactions American Geophysical Union, 79, 579, doi:10.1029/98EO00426, 1998.

Wientjes, I. G. M. and Oerlemans, J.: An explanation for the dark region in the western melt zone of the Greenland ice sheet, The Cryosphere, 4, 261–268, doi:10.5194/tc-4-261-2010, 2010.

Wientjes, I. G. M., Van de Wal, R. S. W., Reichart, G. J., Sluijs, A., and Oerlemans, J.: Dust from the dark region in the western ablation zone of the Greenland ice sheet, The Cryosphere, 5, 589–601, doi:10.5194/tc-5-589-2011, 2011.

Wientjes, I. G. M., Van de Wal, R. S. W., Schwikowski, M., Zapf, A., Fahrni, S., and Wacker, L.: Carbonaceous particles reveal that Late Holocene dust causes the dark region in the western ablation zone of the Greenland ice sheet, Journal of Glaciology, 58, 787–794, doi:10.3189/2012JoG11J165, 2012.

Wiscombe, W. J. and Warren, S. G.: A model for the spectral albedo of snow. I: Pure snow, Journal Of The Atmospheric Sciences, 37, 2712–2733, doi:10.1175/1520-0469(1980)037<2712:AMFTSA>2.0.CO;2, 1980.

Wolfram Research, Inc.: Mathematica, Champaign, Illinois, 2014.

Xu, X., Werner, M., Butzin, M., and Lohmann, G.: Water isotope variations in the global ocean model MPI-OM, Geoscientific Model Development, 5, 809–818, doi:10.5194/gmd-5-809-2012, 2012.

Yallop, M. L., Anesio, A. M., Perkins, R. G., Cook, J., Telling, J., Fagan, D., MacFarlane, J., Stibal, M., Barker, G., Bellas, C., Hodson, A., Tranter, M., Wadham, J., and Roberts, N. W.: Photophysiology and albedo-changing potential of the ice algal community on the surface of the Greenland ice sheet, Isme Journal, 6, 2302–2313, doi:10.1038/ismej.2012.107, 2012.

Yung, P. T., Shafaat, H. S., Connon, S. A., and Ponce, A.: Quantification of viable endospores from a Greenland ice core, FEMS Microbiology Ecology, 59, 300–306, doi:10.1111/j.1574-6941.2006.00218.x, 2007.

Zennaro, P., Kehrwald, N., McConnell, J. R., Schuepbach, S., Maselli, O. J., Marlon, J., Vallelonga, P., Leuenberger, D., Zangrando, R., Spolaor, A., Borrotti, M., Barbaro, E., Gambaro, A., and Barbante, C.: Fire in ice: two millennia of boreal forest fire history from the Greenland NEEM ice core, Climate of the Past, 10, 1905–1924, doi:10.5194/cp-10-1905-2014, 2014.

Zuo, Z. and Oerlemans, J.: Modelling albedo and specific balance of the Greenland ice sheet: Calculations for the Søndre Strømfjord transect, Journal of Glaciology, 42, 305–317, doi:10.3198/1996JoG42-141-305-317, 1996.